nature cell biology

Article

https://doi.org/10.1038/s41556-025-01753-3

CD160 dictates anti-PD-1 immunotherapy resistance by regulating CD8$^+$ T cell exhaustion in colorectal cancer

Received: 30 December 2024

Accepted: 28 July 2025

Published online: 9 September 2025

Check for updates

Tongsen Zheng[1,2,14] ✉, Chujie Ding[1,14], Shihui Lai[1,2,14], Yang Gao[1,2,14], Cheng Lyu[3], Caiqi Liu[1,2], Jiaqi Shi[1,2], Xiaobo Li[4], Mingwei Li[1,2], Hongxue Meng[5], Mingqi Li[6], Yingjian Liang[7,13], Sheng Tai[8,13], Liang Cheng[9], Yan Zhang[1,2], Li Li[6], Peng Han[6], Bin Sun[10], Te Liu[10], Feng Geng[1], Dapeng Hao[3] ✉ & Xue Zhang[11,12] ✉

The colon exhibits higher propensity for tumour development than ileum. However, the role of immune microenvironment differences in driving this disparity remains unclear. Here, by comparing paired ileum and colon samples from patients with colorectal cancer (CRC) and healthy donors, we identified ileum-enriched CD160$^+$CD8$^+$ T cells with previously unrecognized characteristics, including resistance to terminal exhaustion and strong clonal expansion. The transfer of CD160$^+$CD8$^+$ T cells significantly inhibits tumour growth in microsatellite instability-high and inflammation-induced CRC models. *Cd160* knockout accelerates tumour growth, which is mitigated by transferring CD160$^+$CD8$^+$ T cells. Notably, in microsatellite instability-high and anti-PD-1-resistant CRC models, CD160$^+$CD8$^+$ T cells improve anti-PD-1 efficacy and overcome its resistance by increasing tumour-infiltrating progenitor-exhausted T cells, nearly eradicating tumours. Mechanistically, we uncover a CD160–PI3K (p85α) interaction that promotes FcεR1γ and 4-1BB expression via the AKT–NF-κB pathway, thereby enhancing CD8$^+$ T cell cytotoxicity. Our study reveals CD160 as a crucial regulator of CD8$^+$ T cell function and proposes an innovative immunotherapy strategy of transferring CD160$^+$CD8$^+$ T cells to overcome anti-PD-1 resistance.

Colorectal cancer (CRC) is the most common gastrointestinal malignancy worldwide[1]. Intriguingly, the ileum and colon share similar histological structure, transcriptome[2] and close anatomical location, but the colon is more prone to tumour development[3]. The reasons behind this discrepancy in tumour development remain unclear. Emerging evidence suggests that a context-specific immune environment between the ileum and colon may be the key underlying reason for this phenomenon, although this difference has so far only been explored in mice[4–9]. However, systematic differences in the immune landscape between the ileum and colon in patients with CRC and healthy individuals, as well as the underlying mechanisms leading to a higher susceptibility of the colon to tumour, have not been investigated in depth.

Here, we employed single-cell (sc)RNA/B cell receptor (BCR)/T cell receptor (TCR) sequencing (seq) and bulk RNA-seq to identify CD160$^+$CD8$^+$ T cells that are highly enriched in the ileum, characterized by robust clonal expansion and resistance to terminal exhaustion. Using multiple mouse models, including xenograft, azoxymethane (AOM)/dextran sulfate sodium (DSS)-induced CRC models, *Cd160* knockout

A full list of affiliations appears at the end of the paper. ✉e-mail: zhengtongsen@hrbmu.edu.cn; dapenghao@hrbmu.edu.cn; xuezhang@hrbmu.edu.cn

and anti-PD-1 resistant models, we demonstrated that CD160 deficiency accelerates tumour progression, while transferring CD160$^+$ CD8$^+$ T cells significantly inhibits tumour growth in microsatellite instability-high (MSI-H) and inflammation-induced CRC in mice. Importantly, the transfer of CD160$^+$CD8$^+$ T cells in MSI-H CRC mice also significantly improves anti-PD-1 efficacy and overcomes resistance. Mechanistically, CD160 directly interacts with PI3K p85α to promote FcεR1γ and 4-1BB expression, thereby enhancing CD8$^+$ T cell cytotoxicity.

Results

Single-cell immune landscape reveals systematic differences among matched ileum, colon and colorectal tumours

To create an immune cell atlas, we obtained scRNA/BCR/TCR-seq data of CD45$^+$ immune cells from 68 matched samples across patients with CRC and healthy donors, including tumour-draining lymph nodes (LNs), peripheral blood mononuclear cells (PBMCs), ileum, colon and tumour tissues (Fig. 1a and Supplementary Table 1). After rigorous quality filtering, 465,920 high-quality cells were retained. Following batch correction and unsupervised clustering of multiomics data, we identified seven distinct lineages, including four lymphoid subtypes (T, B, natural killer (NK) and plasma cells (PCs)) and three myeloid subtypes (mast cells, plasmacytoid dendritic cells (pDCs) and other myeloid cells) (Fig. 1b and Extended Data Fig. 1a–d). Matched BCR and TCR profiling were highly consistent with the cell identification (Extended Data Fig. 1e). Further subclustering of T cells identified the existence of intraepithelial lymphocyte (IEL)-T cells, which were the most abundant in the ileum (Extended Data Fig. 1f–i).

Substantial differences of the cellular composition and distribution of major cell subsets were observed across tissues. PBMCs were enriched for T and NK cells, while tumour-draining LNs and ileum were enriched for B cells and tumour samples were enriched for myeloid cells, indicating the presence of a heterogeneous immune landscape across various tissues (Fig. 1c,d). *NKG7*, a marker of cytotoxicity and T cell activation, was more highly expressed in ileum and tumour than colon tissue (Fig. 1e). Consistent with IEL-T cell enrichment, the fraction of *CD160*$^+$ cells was the highest in the ileum and sharply lower in the colon and tumour (Fig. 1e). We also identified a subset of *TGFB1*^{high} long-lived plasma cells (LLPCs) that were highly enriched in tumour and colon tissues (Fig. 1f and Extended Data Fig. 2a), consistent with regulatory effects of PCs via secreting transforming growth factor (TGF)-β[10]. BCR clone-matched analysis of 3,188 PC clones across tissues demonstrated that PCs of the same clone exhibited the highest *TGFB1* expression in tumours and the lowest in ileum (Fig. 1g). We observed the highest BCR somatic hypermutation (SHM) frequencies in PCs from ileum and the lowest from tumours (Fig. 1h). Additionally, B cells from tumours were more likely to be IgG$^+$ than those from the ileum or colon (Fig. 1i), a trend independent of cellular subtype composition (Extended Data Fig. 2b–d), further indicating that B cells may take on distinct cell states across tissues. Among myeloid cells, monocytes accumulated in tumour tissue whereas mast cells were depleted in tumours (Extended Data Fig. 2e). Since mast cells have been recognized as a key regulator of antitumour immunity when activated[11], we thus constructed a gene signature to quantify the relative enrichment of mast cells, which significantly associated with prognosis in CRC (hazard ratio (HR) of 0.78 (95% confidence interval 0.66–0.93); Extended Data Fig. 2f). To compare transcriptional states across tissues, we measured the average transcriptomic similarity by conducting unsupervised hierarchical clustering for each cell lineage separately (Fig. 1j and Extended Data Fig. 2g). Overall, immune cells from PBMCs and tumour-draining LNs were separated first. Tissues from healthy donors were clustered together in all cell lineages, indicating the marked influence of tumour on the immune cell states of surrounding normal tissues. However, tumour samples showed high heterogeneity, with some displaying a higher similarity to ileum while others were more like adjacent colon tissue.

Using previously reported gene signatures (Supplementary Table 2), we found that T cells from tumours exhibited the highest terminally exhausted signature, whereas T cells from ileum and colon exhibited the highest IEL signature (Fig. 1k). By linking T cell clones to cellular states using scTCR-seq, we observed substantial enrichment of IEL-T cells within expanded clones, relative to other T cells (Fig. 1l). Additionally, IEL-T cells from ileum displayed the highest cytolytic activity (Fig. 1k). To further explore this association, we compared transcriptome differences of IEL-T cells between ileum and colon tissue, revealing systemic differences strongly correlated between healthy donors and patients with CRC (Fig. 1m and Extended Data Fig. 2h). In addition to *CD160*, the top upregulated genes in ileum included T cell activation-related genes (for example, *IFNG*, *GZMA* and *GNLY*) (Fig. 1m). Clustering of samples by the average expression of top differentially expressed genes (DEGs), we found that IEL-T cells from tumours were highly heterogeneous, with some samples closer in their gene signature to colon-like IEL-T cells and others closer to ileum-like IEL-T cells (Extended Data Fig. 2i).

Heterogeneity of T cell states across matched ileum, colon and colorectal tumours

To further investigate tumour heterogeneity in relation to ileum and colon tissue, we compared transcriptomic similarities of ileum (n = 187) and colon (n = 779) from the GTEx project and CRC samples (n = 458) from The Cancer Genome Atlas (TCGA) project. Unsupervised clustering of immune-related genes stratified CRC samples into two clusters, one together with colon (C1) and the other one with ileum (C2), and C2 showed significantly better prognosis than C1 (Extended Data Fig. 3a,b). Top DEGs between C2 and C1 were significantly enriched in the T cell activation pathway (Extended Data Fig. 3c,d), suggesting

Fig. 1 | Single-cell immune landscape in matched ileum, colon and colorectal tumours. a, A schematic diagram illustrating the workflow analysis of the single-cell study. scRNA-seq, paired scBCR-seq and scTCR-seq were applied to CD45$^+$ immune cells of ileum, colon, tumour tissues, tumour-draining LNs and PBMCs derived from patients with CRC and ileum and colon derived from healthy donors. **b**, A UMAP plot showing the major subtypes of CD45$^+$ immune cells. Cells are colour coded by their inferred cell types based on transcriptional, BCR and TCR profiles. **c**, UMAP plots, as in **b**, showing the cell density across different tissues. **d**, Percentage bar graphs showing the composition and proportions of total CD45$^+$ immune cells across different tissues. T cells are further separated into CD4$^+$ T, CD8$^+$ T, IEL-T and other unconventional T cells. **e**, Box plots showing the proportions of PCs, *NKG7*$^+$ cells and *CD160*$^+$ cells among immune cells across different tissues in patients with CRC (n = 10) and healthy donors (n = 3). **f**, Box plots showing the paired comparisons of cell proportions of LLPCs among tissues from the same patients with CRC (n = 10) and healthy donors (n = 3). NS, not significant. **g**, Box plots showing the average *TGFB1* expression of PC clones (n = 3,188) that are matched among the indicated tissues. **h**, Box plots showing the paired comparisons of the average SHM frequency of PCs among tissues from the same patients with CRC (n = 10) and healthy donors (n = 3). **i**, Box plots showing the paired comparisons of cell proportions of IgG$^+$ B cells among paired tissues from the same patients with CRC (n = 10) and healthy donors (n = 3). **j**, Unsupervised hierarchical clustering dendrogram of T cells, PCs and mast cells derived from the average transcriptome profiles across tissues in patients with CRC and healthy donors. **k**, Box plots showing terminal exhaustion score (left) and IEL score (middle) in T cells and cytolytic activity score in IELs (right) across different tissues. **l**, An alluvial plot showing the proportion of indicated T cell subsets with different clone sizes. **m**, Scatter plots illustrating the correlation of differentially expressed genes of IELs between ileum and colon in patients with CRC (y axis) against the corresponding value in healthy donors (x axis) by Pearson's correlation analysis. P values were determined by paired two-sided Mann–Whitney tests (**e**–**i** and **k**). In the box plots, the centre line is the median, box limits are the first and third quartiles and whiskers are 1.5× interquartile range.

https://doi.org/10.1038/s41556-025-01753-3

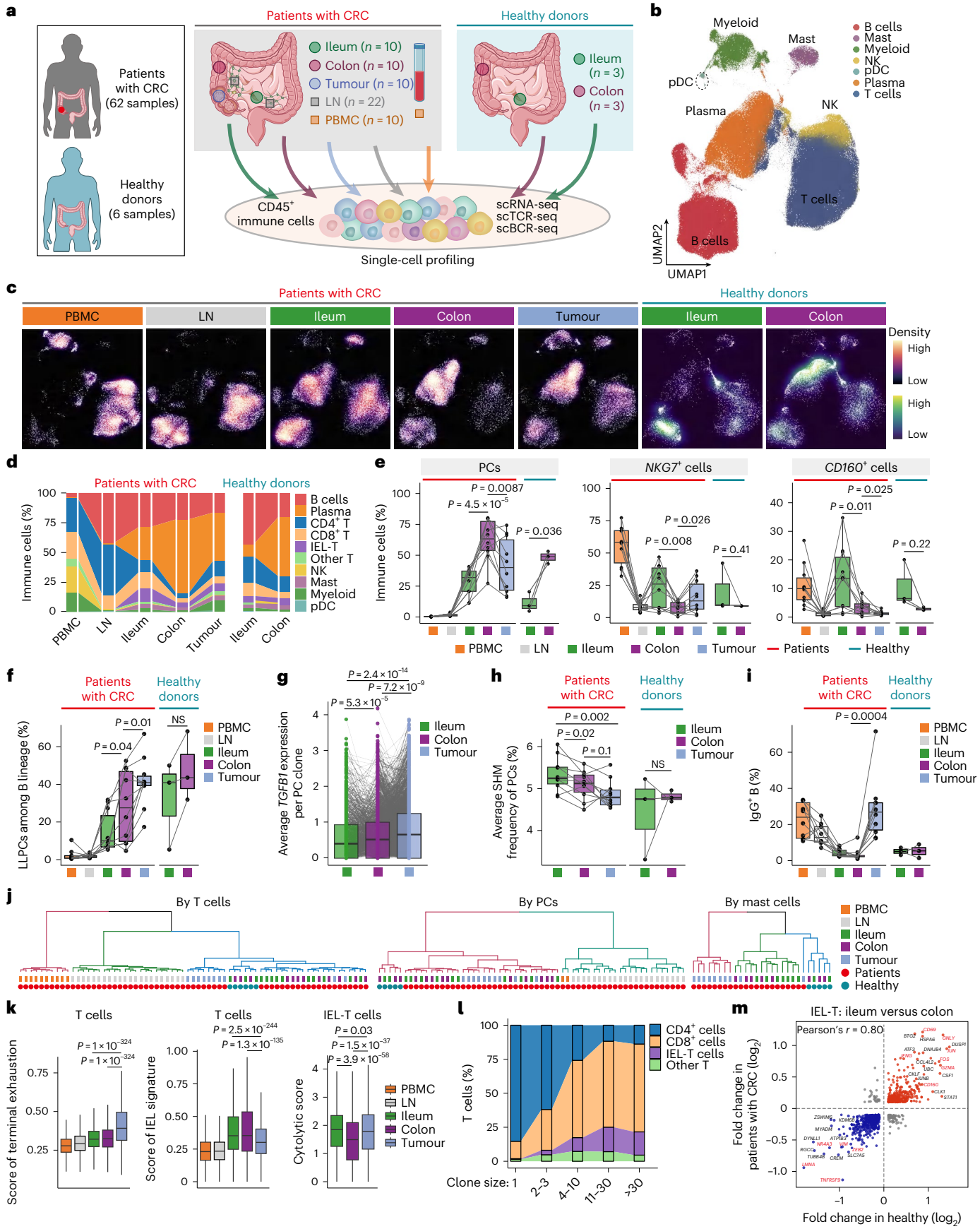

that differential T cell states between ileum and colon manifest in the heterogeneous tumour microenvironment (TME) in tumours and predict prognosis. To verify the result while controlling for interpatient heterogeneity, we obtained paired ileum and colon tissues from healthy donors and patients with CRC (Supplementary Table 1) and confirmed the enrichment in T cell activation (Extended Data Fig. 3e).

To characterize heterogeneous T cell states across tissues, we performed further clustering analyses, revealing six $CD4^+$ T cell states, eight $CD8^+$ T cell states and γδT cells (Fig. 2a and Extended Data Fig. 3f-k). IEL-T cells were identified by the expression of canonical IEL markers and the absence of the intestinal lamina propria marker *CD6* (Fig. 2a and Extended Data Fig. 3g)[12–14]. γδT cells with strong IEL signatures were identified by the additional expression of *TYROBP* and *TCRγδ* genes[15] and grouped with $CD8^+$ T cells because of high transcriptional and functional similarity (Fig. 2a and Extended Data Fig. 3f,g). We did not detect a cluster of recently reported $TCR\gamma\delta^+CD8\alpha^+$ IEL-T cells in our dataset[8]. Overall, $CD4^+$ and $CD8^+$ T cells showed upregulated T cell activation-related genes in ileum, whereas tumour samples showed upregulated genes involved in T cell dysfunction (Fig. 2b).

Among $CD4^+$ T cells (Extended Data Fig. 3h), regulatory (T_{reg}) and follicular helper (T_{FH}) T cells were more abundant in draining LNs and tumour samples, whereas naive (T_{Naive}), central memory (T_{CM}) and effector memory (T_{EM}) T cells were more abundant in ileum and colon, and understudied $CD4^+$ cytotoxic T (T_{CTL}) cells[16] were enriched in PBMCs and ileum (Extended Data Fig. 3l). Compared with colon and tumour, the ileum showed a relatively higher fraction of T_{EM} and T_{CTL} cells and a lower fraction of T_{reg} cells, although not all achieved significance, probably due to the small cohort size. Among $CD8^+$ T cells (Fig. 2a), memory T (T_{Mem}) cells were more abundant in ileum, whereas transitional effector T cells ($GZMK^+$ eff.), which were similar to previously described $GZMK^+$ effector T cells, were more abundant in tumour regions (Extended Data Fig. 3m)[17]. To identify tumour-reactive T cells, we employed a tumour-reactivity signature based on published features of neoantigen-reactive tumour-infiltrating T cells[18] (Supplementary Table 2), which revealed that T_{reg}, T_{FH} and $TCR\alpha\beta^+$ IEL-T cells were in tumour-reactive states (Extended Data Fig. 3n). Additionally, T_{reg} and T_{FH} cells from ileum of healthy donors had the lowest neoantigen-reactivity score (Extended Data Fig. 3o), indicating that tumorigenesis influences the $CD4^+$ T cell states of the surrounding ileum or colon.

We then measured the average expression of 129 genes predictive of favourable prognosis in TCGA CRC samples (Supplementary Table 3) across major T cell states within the TME, which revealed the strongest expression in $TCR\alpha\beta^+$ IEL-T cells (Fig. 2c). $TCR\alpha\beta^+$ IEL-T cells also showed the highest signature of T cell activation and dysfunction. Consistently, CRC samples from cluster C2 exhibited significantly higher IEL signatures than C1 (Extended Data Fig. 4a). We also obtained upregulated genes in responders to immune checkpoint blockade (ICB) from a CRC cohort that received first-line ICB therapy[19] and observed the strongest expression in $TCR\alpha\beta^+$ IEL-T cells (Fig. 2d).

We then focused on $TCR\alpha\beta^+$ IEL-T cells, which highly expressed T cell exhaustion markers *TIGIT*, *LAYN*, *TOX* and *LAG3* (Fig. 2e). As recent studies have uncovered heterogeneous states of exhausted T cells, including terminally exhausted T (T_{Tex}) and progenitor-exhausted T (T_{Pex}) cells, which respond to ICB[20], we measured individual cells for progenitor and terminally exhausted $CD8^+$ T cell signatures (Supplementary Table 2). By comparing across tissues, we found that $TCR\alpha\beta^+$ IEL-T cells from ileum and colon exhibited significantly higher progenitor exhaustion (Exh_Pex) signature scores, whereas those from tumours exhibited significantly higher terminal exhaustion (Exh_Tex) scores (Fig. 2f). We also compared γδT cells, for which a decreased cytotoxicity towards terminal exhaustion in colon cancer has been reported[21], and observed that γδT cells showed the highest cytotoxicity in the ileum and the lowest in tumours (Fig. 2f).

Expression of *CD160* features the state transition of $CD8^+$ T cell exhaustion

To investigate the exhausted T cell state transition, we performed pseudotime analysis using Monocle to infer the differentiation trajectory of $TCR\alpha\beta^+$ IEL-T cells[22]. The analysis showed a trajectory that started from ileum and colon and then segregated into two branches enriched by T cells from tumours. Component 1 of the trajectory correlated with the Exh_Tex signature, and component 2 correlated with the cell proliferation signal (Fig. 2g and Extended Data Fig. 4b). Along the pseudotime axis, we observed elevated signals of Exh_Tex and a reduced signal of Exh_Pex (Fig. 2g), consistent with previous reports that T_{Pex} cells give rise to T_{Tex} cells[23,24]. To further confirm that $TCR\alpha\beta^+$ IEL-T cells early and later in pseudotime correspond to a more progenitor and terminal exhaustion phenotype, respectively, we examined dynamic expression changes of canonical markers (Extended Data Fig. 4c). Consistently, expression of *EOMES* and *TOX*, which are associated with a more Exh_Tex state, was gradually increased along pseudotime. In contrast, the expression levels of *IL7R* and *REL*, which are markers of a progenitor state[23], were gradually decreased along pseudotime. We then examined the expression dynamics along the trajectory for other noncanonical genes and found highly correlated variation of *CD160* expression in all three tissues, indicating a strong association between *CD160* expression and IEL-T cell state transition (Fig. 2g).

CD160 has been recognized as a marker of IELs[25]. However, we found that *CD160* was widely expressed in $CD8^+$ T cell subpopulations

Fig. 2 | Immune characteristics of T cell subsets across ileum and colon tissues both in healthy donors and patients with CRC. a, UMAP plots showing the subtypes of $CD8^+$ T and IEL-T cells from ileum, colon and tumour tissues. Cells are colour coded by their inferred cell types/states based on transcriptional profiles (upper), IEL score (bottom left) and marker gene expression (bottom right). **b**, Heat maps showing the normalized expression of genes involved in T cell activation and T cell dysfunction for $CD4^+$ and $CD8^+$ T cells across the indicated tissue types (left). Box plots compare the average expression of the indicated genes in the heat map among matched tissues from the same patients ($n = 10$, right). **c**, Box plots showing the average expression (Avg. exp.) of prognostic genes (upper) and T cell activation (middle) and dysfunction (bottom) genes across the indicated cell subtypes in TCGA CRC samples. **d**, Box plots showing the average expression of upregulated genes in ICB responders across the indicated cell subtypes. **e**, The same UMAP as in **a** but with cells coloured by *TIGIT*, *LAYN*, *TOX* and *LAG3* expression. **f**, Box plots showing the Exh_Pex score (left) and Exh_Tex score (middle) of $TCR\alpha\beta^+$ IEL-T cells and cytolytic activity of γδT cells (right) across the indicated tissue types. **g**, Monocle trajectory reconstruction of $TCR\alpha\beta^+$ IEL-T cells. Cells are coloured by pseudotime (upper left) and tissue types (upper right). Regression lines are fitted against pseudotime for the indicated Exh_Pex and Exh_Tex score (bottom left), *PDCD1* and *CD160* expression (bottom right) of different tissue types. **h**, Bubble plot showing the expression (exp.) of *CD160* across $CD8^+$ T cell subtypes among the indicated tissues. The dot size indicates frequencies of expressing cells, coloured according to normalized expression level. **i**, Box plots showing the paired comparisons of cell proportions of $CD160^+$ among $CD8^+$ T cells across matched tissues from the same patients with CRC ($n = 10$) and healthy donors ($n = 3$). **j**, Representative immunofluorescence staining and quantification of ileum, colon and tumour from patients with CRC. Staining for CD8 (green), CD160 (red) and DAPI (blue). The red triangles highlight $CD160^+CD8^+$ T cells. Scale bars, 50 μm ($n = 5$ samples). **k**,**l**, Representative flow cytometry plots (**k**) and frequencies (**l**) of CD160 in $CD8^+$ T cells among different intestinal tissues from patients with CRC ($n = 4$ samples). **m**, Scatter plots illustrating the correlation of differentially expressed genes of $CD8^+$ T cells between $CD160^-$ versus $CD160^+$ in colon (*y* axis) against the corresponding value in ileum (*x* axis). FC, fold change. *P* values were determined by paired two-sided Mann–Whitney test (**b**, **f** and **i**). Data are shown as the mean ± s.e.m. *P* values were determined by unpaired two-tailed Student's *t*-tests (**j** and **l**). In the box plots, the centre line is the median, box limits are the first and third quartiles and whiskers are 1.5× interquartile range.

https://doi.org/10.1038/s41556-025-01753-3

and exhibited strong tissue specificity (Fig. 2h). We observed the highest fraction of *CD160*$^+$ T cells in ileum and the lowest fraction in tumours across all CD8$^+$ T cell subtypes (Fig. 2i), consistent with public datasets (Extended Data Fig. 4d). To further validate the tissue-specific expression of CD160, we used multiplex immunofluorescence and flow cytometry to quantify CD160$^+$CD8$^+$ T cells in independent CRC samples and observed the highest fraction in ileum and the lowest fraction in tumours (Fig. 2j–l). Similarly, in C57BL/6 mice, CD160$^+$CD8$^+$ T cells were significantly higher in small intestine (duodenum, jejunum and ileum) compared with colon (Extended Data Fig. 4e,f). We further

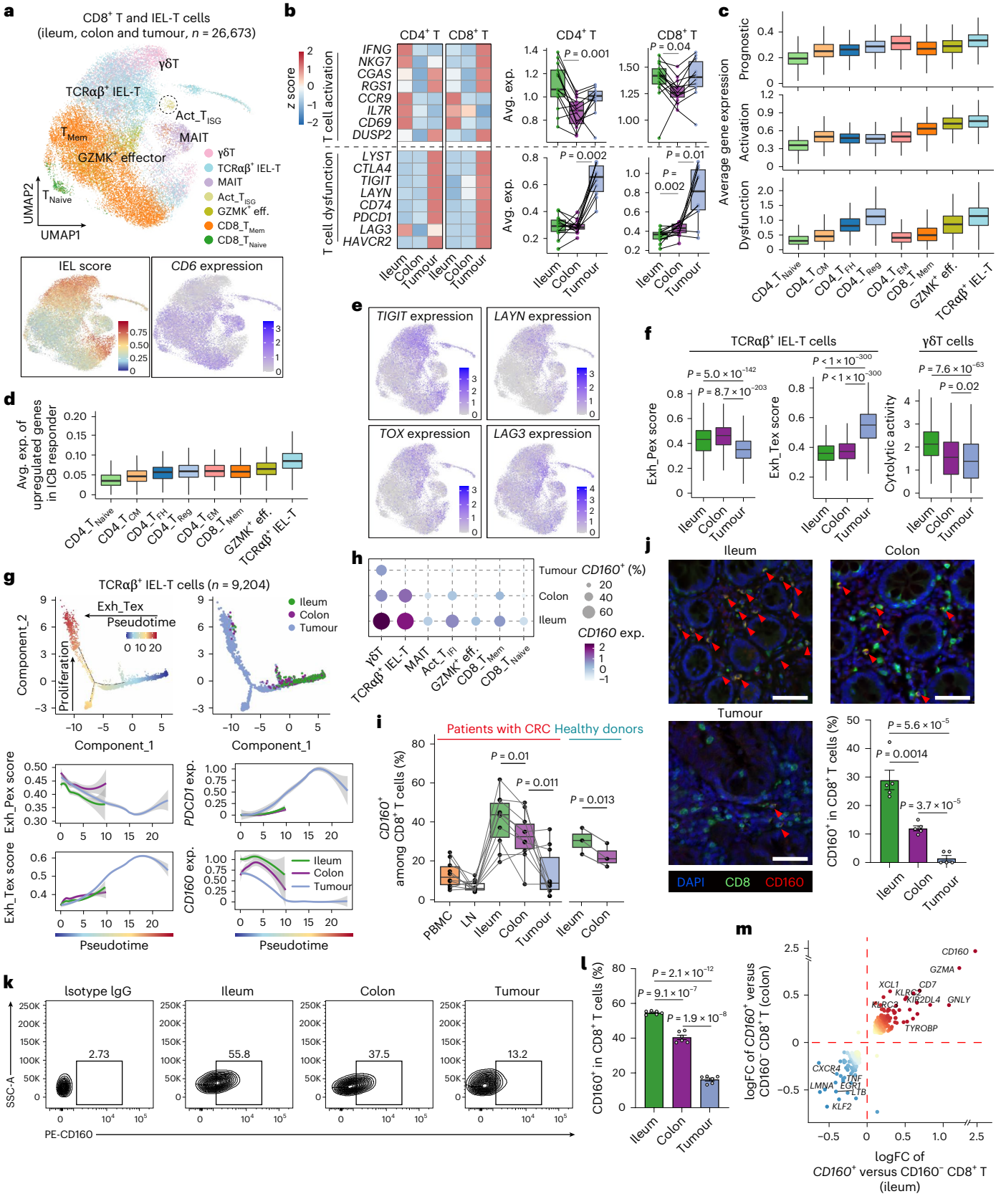

https://doi.org/10.1038/s41556-025-01753-3

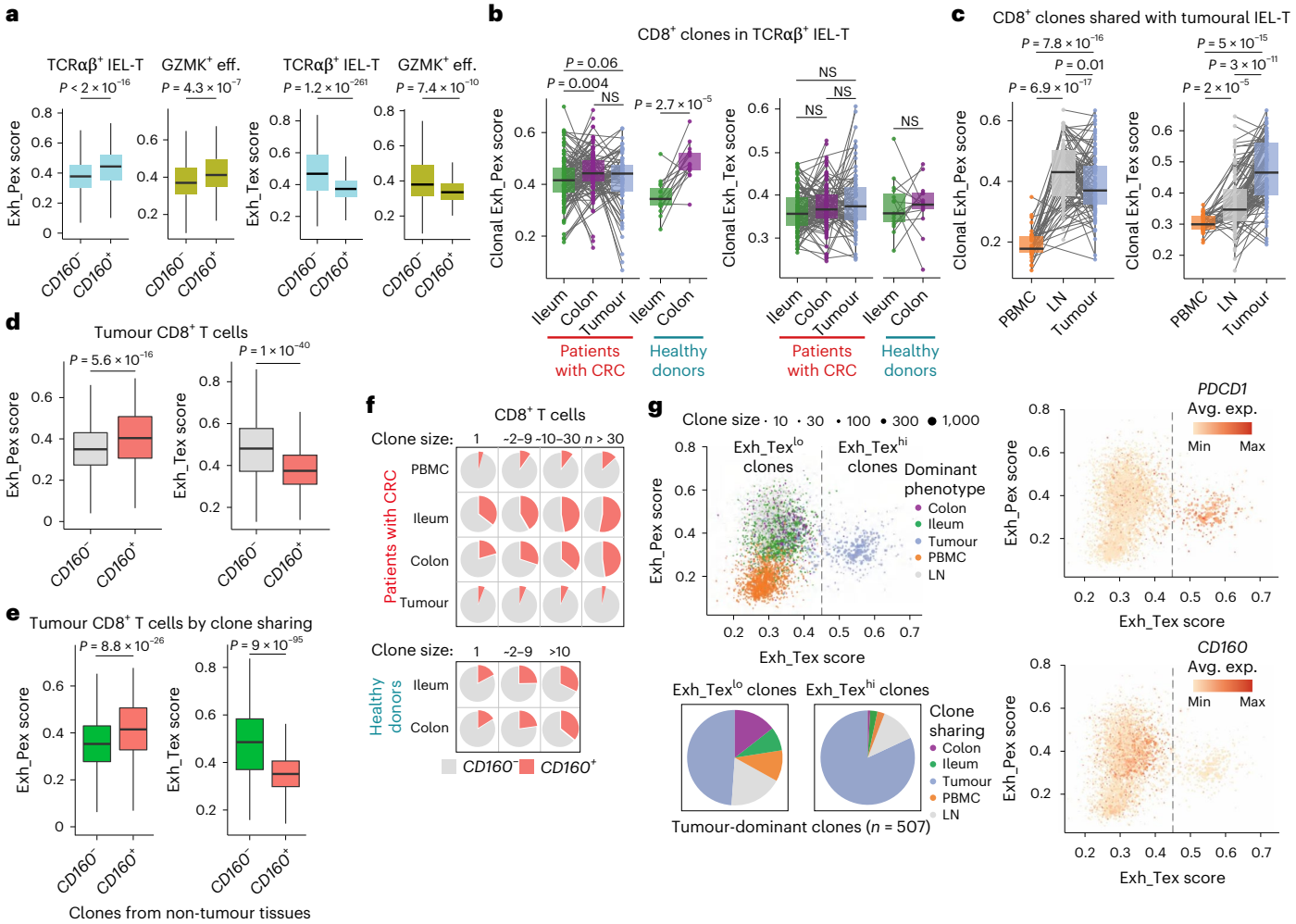

Fig. 3 | Lineage tracing of clonal state transition of CD8⁺ T cells. a, Box plots showing the Exh_Pex score and Exh_Tex score between *CD160*⁺ and *CD160*⁻ cells across the indicated CD8⁺ T subtypes. **b**, Box plots showing the average Exh_Pex score (left) and Exh_Tex score (right) per CD8⁺ clone in TCRαβ⁺ IEL-T cells that are matched among the indicated tissues in patients with CRC ($n = 129$) and healthy donors ($n = 15$). **c**, Box plots showing the average Exh_Pex score (left) and Exh_Tex score (right) per CD8⁺ clones that are clonally linked to tumoural TCRαβ⁺ IEL-T cells across matched tissues ($n = 95$). **d**, Box plots showing the Exh_Pex score (left) and Exh_Tex score (right) between tumoural *CD160*$^{+/-}$CD8⁺ T cells. **e**, Box plots showing the Exh_Pex score (left) and Exh_Tex score (right) of tumoural CD8⁺ T cells clonally linked to *CD160*^{hi} clones and *CD160*⁻ clones. **f**, Pie charts showing the percentage of *CD160*⁺ T cells among CD8⁺ T cells across indicated tissues in patients with CRC and healthy donors. Cells are grouped by clone size. LNs were not included owing to too few *CD160*⁺ cells. **g**, Exh_Pex score versus Exh_Tex score for all CD8⁺ T cell clones ($n = 4{,}758$), coloured by the dominant phenotype of cells within each clone (upper left) and the average expression of indicated genes (right). Exh_Tex^{hi} and Exh_Tex^{lo} clones are separated by a visually obvious cut off of the average exhaustion score 0.45. Pie charts show the percentage of Exh_Tex^{hi} and Exh_Tex^{lo} clones ($n = 507$ in total) per indicated regional pattern (bottom left). *P* values were determined by paired two-sided Mann–Whitney tests (**a**–**e**). In the box plots, the centre line is the median, box limits are the first and third quartiles and whiskers are 1.5× interquartile range.

corroborated this finding in AOM/DSS-induced CRC mice (Extended Data Fig. 4g,h) and found the highest expression of CD160 in ileum CD8⁺ T cells and the lowest in tumour CD8⁺ T cells (Extended Data Fig. 4i–l). These results align with our scRNA-seq data, suggesting that *CD160* expression could be dynamically regulated by local contexts across tissues. Comparison between *CD160*⁺ and *CD160*⁻ CD8⁺ T cells in ileum and colon revealed consistent upregulation of genes involved in T cell cytotoxicity (Fig. 2m), in agreement with the reported cytolytic effect of CD160⁺ T cells[8,26,27].

To further investigate whether CD160 featured the state transition of T cell exhaustion, we compared progenitor and terminal exhausted signatures for individual effector CD8⁺ T cells, including TCRαβ⁺ IEL-T and GZMK⁺ eff. cells. *CD160* expression positively correlated with Exh_Pex signature and negatively correlated with Exh_Tex signature (Fig. 3a). Collectively, these data support the association between CD160 expression and the state transition of CD8⁺ T cell exhaustion.

Tumour-exhausted CD8⁺ T cells are clonally linked to *CD160*⁻ T cell progenitors

To assess whether clonal IEL-T cell states vary across tissues, we evaluated exhaustion signatures by clone-matched analysis of TCRαβ⁺ IEL-T cells. Notably, most of TCRαβ⁺ IEL-T clones that matched across ileum, colon and tumour tissues contain *CD160*⁺ T cells. While the average signature of Exh_Pex may have slightly increased in matched clones from ileum to colon and tumours, the Exh_Tex signature did not increase significantly (Fig. 3b). We also compared PBMCs and LNs for T cells clonally matched with tumoural TCRαβ⁺ IEL-T cells, which revealed a significant increase of Exh_Tex signature in clones from PBMCs and LNs to tumour regions (Fig. 3c). Additionally, we observed the highest Exh_Pex signature in clonally linked T cells from LNs (Fig. 3c), in agreement with the recent report that T_{Tex} cells in the tumour are derived from progenitor/stem-like exhausted T cells of LNs[28]. We also divided tumoural TCRαβ⁺ IEL-T cells into groups based on the tissue origin of clonally matched T cells. Tumoural IEL-T cells

that were specific to tumours or clonally linked to T cells from PBMCs and LNs had a significantly higher Exh_Tex signature and lower Exh_Pex signature than those that shared clones with ileum or colon (Extended Data Fig. 4m). Collectively, these data imply that *CD160*$^+$CD8$^+$ T cells from ileum and colon are unlikely to be terminally exhausted in tumours relative to T cells from LNs and PBMCs.

To further explore the association between *CD160* and T cell exhaustion, we compared exhaustion scores of tumour CD8$^+$ T cells by whether they expressed *CD160* and found that *CD160*$^-$ T cells had a higher Exh_Tex signature and a lower Exh_Pex signature than *CD160*$^+$ T cells (Fig. 3d). This pattern was further confirmed in an independent scRNA-seq dataset of CRC[29] (Extended Data Fig. 4n). Next, we defined *CD160*$^+$and *CD160*$^-$ clones using all CD8$^+$ T cells from non-tumour tissues and compared exhaustion signatures for tumour CD8$^+$ T cells clonally linked to these cells. Tumour CD8$^+$ T cells clonally linked to non-tumour *CD160*$^+$ clones had a significantly higher Exh_Pex signature and a lower Exh_Tex signature than those clonally linked to non-tumour *CD160*$^-$ clones (Fig. 3e and Extended Data Fig. 4o). As cytotoxic CD8$^+$ T cell clones preferentially expand, we next examined whether *CD160* featured the clonal expansion by surveying T cells according to their clone sizes. We noted the gradually increasing percentage of *CD160*$^+$ T cells within expanded clones in normal tissues but not in tumours (Fig. 3f), indicating the distinct clonal expansion preference of *CD160*$^+$ T cells across tissues.

After characterizing all individual clones of CD8$^+$ T cells, we observed high Exh_Tex signatures in the largest clones dominated by tumoural T cells and low Exh_Pex signatures in the clones dominated by PBMCs T cells (Fig. 3g). Generally, clones with high Exh_Pex signatures were well separated by ileum/colon and LN-dominant clones. We divided all clones dominated by tumoural CD8$^+$ T cells into Exh_Tex^{hi} and Exh_Tex^{lo} groups according to the natural cut off shown by the distribution of clones and analysed lineage relationships with other tissues (Fig. 3g). We found that the majority of Exh_Tex^{lo} clones had a lineage connection with other tissues. By contrast, Exh_Tex^{hi} clones were largely restricted to tumours or clonally linked to CD8$^+$ T cells from LNs. By dividing individual tumoural CD8$^+$ T cells into Exh_Tex^{hi} and Exh_Tex^{lo} groups, we observed a substantial lineage connection between tumoural Exh_Tex^{hi} cells and CD8$^+$ T cells from PBMCs (Extended Data Fig. 4p), indicating that these cells were not included in clones dominated by tumoural CD8$^+$ T cells. On the other hand, few tumoural Exh_Tex^{hi} cells were clonally linked with CD8$^+$ T cells from ileum and colon. These results suggest that T_{Tex} cells are either tumour specific or clonally linked to *CD160*$^-$CD8$^+$ T cells from LNs (Extended Data Fig. 4p). Further transcriptomic comparison indicated that CD160$^+$CD8$^+$ T cells from different tissues of healthy donors and patients with CRC maintained transcriptional stability and were less prone to terminal exhaustion (Extended Data Fig. 5a–e), whereas CD160$^-$CD8$^+$ T cells upregulated Exh_Tex signatures (Extended Data Fig. 5c). In MC38 tumour-bearing mice, CD160$^+$CD8$^+$ T cells exhibited a significantly higher proportion of progenitor-exhausted cells (TCF1$^+$PD-1$^+$) than their CD160$^-$ counterparts across spleen, ileum, colon and tumour tissues (Extended Data Fig. 5f,g). Collectively, these findings demonstrate that CD160$^+$CD8$^+$ T cells from different tissues share a highly similar transcriptomic and progenitor-exhausted phenotype.

CD160 defines a CD8$^+$ T cell subset with strong cytotoxicity and exhaustion resistance

To evaluate CD160$^+$CD8$^+$ T cell function, we compared cytotoxic granule expression between CD160$^+$CD8$^+$ and CD160$^-$CD8$^+$ T cells. After anti-CD3/CD28 stimulation, CD160$^+$CD8$^+$ T cells exhibited a higher GzmB$^+$ fraction than in their CD160$^-$ counterparts (Fig. 4a,b), indicating higher cytotoxicity. To further investigate the exhaustion-resistant capacity of CD160$^+$CD8$^+$ T cells, we established an in vitro chronic stimulation model by continuous anti-CD3 stimulation, which induced upregulation of exhaustion markers (PD-1 and TIM3) (Fig. 4c)[30], and found CD160$^+$CD8$^+$ T cells exhibited fewer terminally exhausted (TIM3$^+$PD-1$^+$) phenotype than their CD160$^-$ counterparts (Fig. 4d,e), confirming their enhanced resistance to terminal exhaustion. Next, we isolated CD160$^+$CD8$^+$ and CD160$^-$CD8$^+$ T cells from axillary LNs of MC38-GFP tumour-bearing mice and expanded them separately (Fig. 4f). Co-culturing these cells with autologous tumour cells revealed significantly higher tumour cell death in the presence of CD160$^+$CD8$^+$ T cells, as measured by LIVE/DEAD indicator dye (Fig. 4g,h).

To assess tumour infiltration in vivo, we co-transferred CD160$^+$CD8$^+$ T cells (from GFP mice) and CD160$^-$CD8$^+$ T cells (from CD45.1 mice) into CD45.2 MC38 tumour-bearing mice (Extended Data Fig. 6a,b). At 36 h after transfer, we observed significantly higher infiltration of CD160$^+$CD8$^+$ T cells (GFP$^+$CD45.1$^-$) than CD160$^-$CD8$^+$ T cells (GFP$^-$CD45.1$^+$) within tumours (Extended Data Fig. 6c,d), suggesting enhanced tumour infiltration capacity of CD160$^+$CD8$^+$ T cells. To assess tumour-specific activation, CD160$^+$CD8$^+$ T cells sorted from CD45.1 mice were transferred into MC38-OVA tumour-bearing mice. Among tumour-infiltrating CD45.1$^+$ cells, the proportion of OVA-tetramer$^+$ cells increased time dependently, indicating that CD160$^+$CD8$^+$ T cells become activated in the TME and gradually acquire antigen specificity (Extended Data Fig. 6e, f).

Collectively, CD160 marks cytotoxic and exhaustion-resistant CD8$^+$ T cells with dual functional advantages of superior tumour infiltration and progressive acquisition of tumour antigen specificity within the TME. These findings suggest that CD160$^+$CD8$^+$ T cells play fundamental roles in tumour inhibition of CRC.

Transfer of CD160$^+$CD8$^+$ T cells inhibits colorectal tumour development by enhancing tumour-infiltrating CD8$^+$ T cell cytotoxicity

To investigate the antitumour effects of CD160$^+$CD8$^+$ T cells in vivo, we performed adoptive transfer experiments in AOM/DSS-induced CRC mice (Fig. 4i). Mice that received CD160$^+$CD8$^+$ T cells had significantly

Fig. 4 | CD160$^+$CD8$^+$ T cells exhibit strong cytotoxicity and resistance to exhaustion with adoptive transfer inhibiting CRC progression. **a**,**b**, Representative flow cytometry plots (**a**) and frequencies (**b**) of GzmB in splenic CD160$^{+/-}$CD8$^+$ T isolated from normal C57BL/6 mice. Cells were stimulated with αCD3/CD28 for 24 h ($n = 3$ biological replicates). **c**, A diagram of the in vitro exhaustion assay. **d**,**e**, Representative flow cytometry plots (**d**) and frequencies (**e**) of TIM3$^+$PD-1$^+$ in splenic CD160$^+$ versus CD160$^-$CD8$^+$ T cells from normal C57BL/6 mice ($n = 3$ biological replicates). **f**, A schematic representation of the co-culture system. Axillary draining lymph node-derived CD160$^{+/-}$CD8$^+$ T cells obtained from MC38-GFP tumour-bearing mice were cultured with autologous MC38-GFP tumour cells at a ratio of 10:1 for 48 h. GFP$^+$ MC38 tumour cells death rate was determined by flow cytometry. **g**,**h**, Representative flow cytometry plots (**g**) and frequencies (**h**) of Zombie-NIR-positive cells in GFP$^+$ MC38 cells. Zombie-NIR-positive cells in the GFP$^+$ MC38 population are considered as dead or dying cells ($n = 3$ biological replicates). **i**, The experimental scheme for adoptive T cell transfer in AOM/DSS-induced CRC mice. Splenic CD160$^{+/-}$CD8$^+$ T cells from normal syngeneic C57BL/6 mice were transferred via tail vein injection at the indicated time points. i.v., intravenous. **j**, Representative images of colon tumours in AOM/DSS-induced CRC mice, as shown in **i** ($n = 10$ mice). Black triangles indicate the site of tumour occurrence. **k**,**l**, Total tumour number (**k**) and tumour size (**l**) in colon tissues were calculated under the indicated treatments, as shown in **i** ($n = 10$ mice). **m**, The experimental scheme for adoptive T cell transfer while inoculating the MC38 cell line into C57BL/6 mice. Splenic CD160$^{+/-}$CD8$^+$ T cells from normal syngeneic C57BL/6 mice were transferred via tail vein injection at the indicated time points. **n**,**o**, Representative tumour images (**n**) and tumour volume (**o**) in MC38 tumour-bearing mice, as shown in **m** ($n = 5$ mice). **p**, Frequencies of GzmB in CD8$^+$ T cells isolated from tumour tissues in MC38 tumour-bearing mice, as shown in **m** ($n = 5$ mice). Data are shown as the mean ± s.e.m. *P* values were determined by unpaired two-tailed Student's *t*-tests (**b**, **e**, **h**, **k**, **l**, **o** and **p**).

https://doi.org/10.1038/s41556-025-01753-3

reduced tumour numbers and sizes compared with those that received PBS (Fig. 4j–l). In contrast, mice that received CD160$^-$CD8$^+$ T cells showed no effect.

Next, two transfer strategies evaluated the effects of CD160$^+$ CD8$^+$ T cells at different tumour stages. First, CD160$^+$CD8$^+$ T cells were injected simultaneously with MC38 cell inoculation in C57BL/6 mice to mimic their impact in early tumour development (Fig. 4m) and which developed significantly smaller tumours than those injected with CD160$^-$CD8$^+$ T cells or PBS (Fig. 4n,o). Additionally, after the transfer of CD160$^+$CD8$^+$ T cells, increased tumour-infiltrating

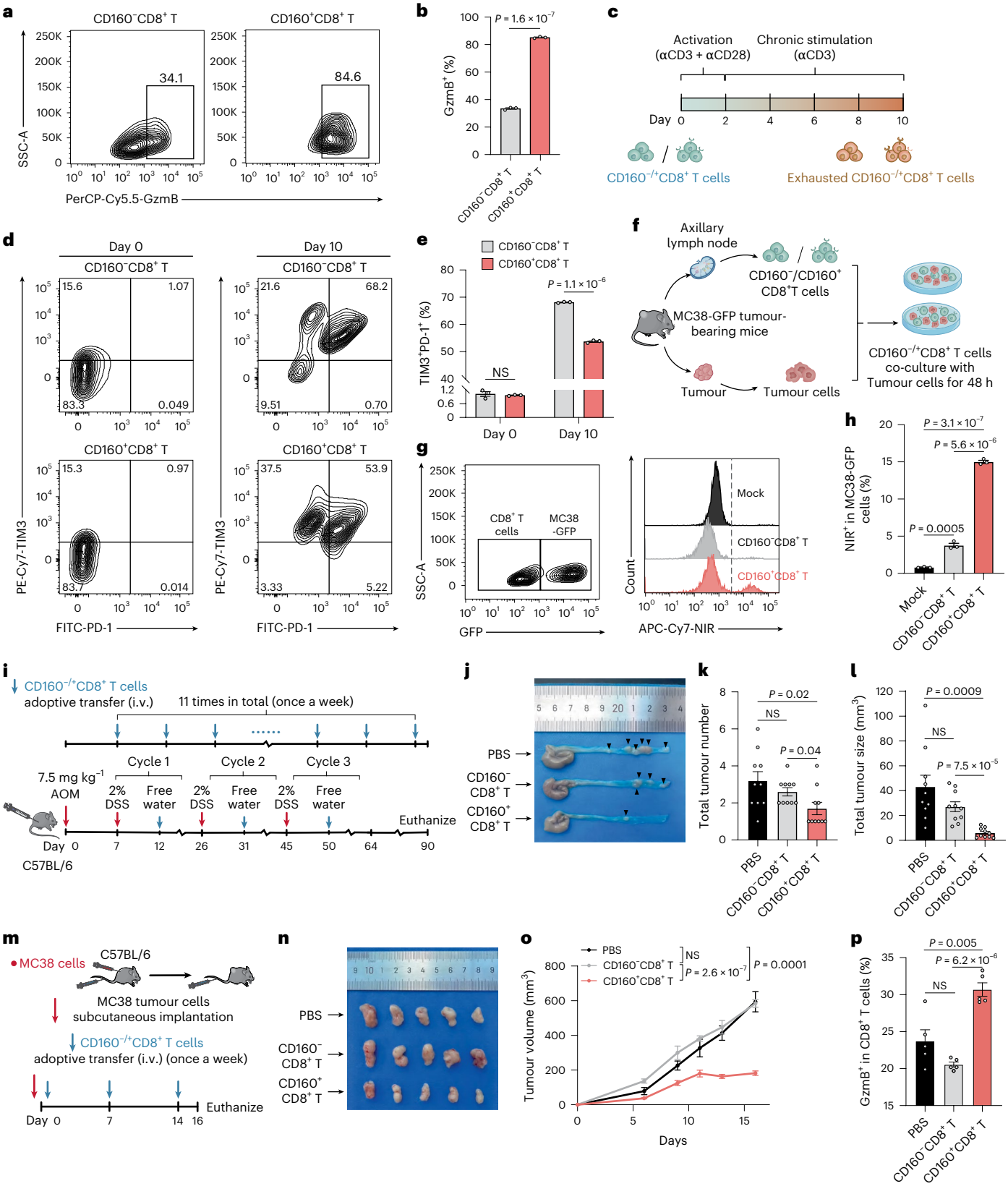

https://doi.org/10.1038/s41556-025-01753-3

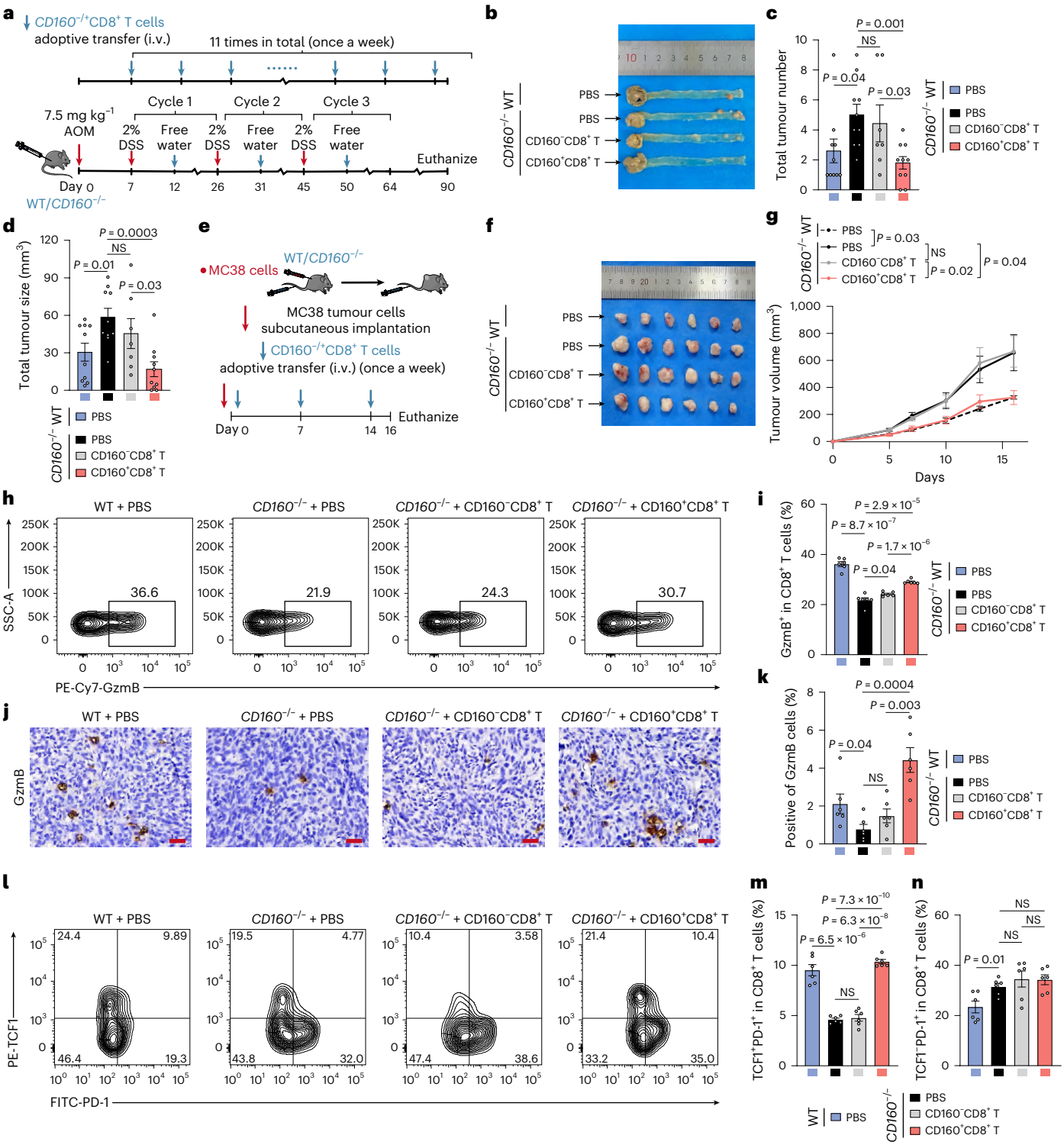

Fig. 5 | CD160 deficiency accelerates tumour progression and promotes terminal exhaustion of tumour-infiltrating CD8⁺ T cells. a, The experimental scheme for adoptive T cell transfer in *Cd160*$^{-/-}$ CRC mice induced by AOM/DSS. Splenic CD160$^{+/-}$CD8⁺ T cells from normal syngeneic C57BL/6 mice were transferred into *Cd160*$^{-/-}$ recipient mice at the indicated time points. **b**, Representative images of colon tumours from an AOM/DSS-induced CRC model in WT and *Cd160*$^{-/-}$ mice, as shown in **a** ($n = 7$–10 mice). **c**,**d**, The total tumour number (**c**) and tumour size (**d**) in colon tissues were calculated under the indicated treatments, as shown in **a** ($n = 7$–10 mice). **e**, The experimental scheme for adoptive T cell transfer while inoculating the MC38 cell line into *Cd160*$^{-/-}$ mice. Splenic CD160$^{+/-}$CD8⁺ T cells from normal syngeneic C57BL/6 mice were transferred into *CD160*$^{-/-}$ recipient mice via tail vein injection at the indicated time points. **f**,**g**, Representative tumour images (**f**) and tumour volume (**g**) in WT and *Cd160*$^{-/-}$ mice, as shown in **e** ($n = 6$ mice). **h**,**i**, Representative flow cytometry plots (**h**) and frequencies (**i**) of GzmB in CD8⁺ T cells isolated from tumour tissues in WT and *Cd160*$^{-/-}$ mice, as shown in **e** ($n = 6$ mice). **j**,**k**, Representative IHC staining (**j**) and quantification (**k**) of GzmB in tumour tissues in WT and *Cd160*$^{-/-}$ mice, as shown in **e**. Scale bars, 30 μm ($n = 6$ mice). **l**–**n**, Representative flow cytometry plots (**l**) and frequencies of TCF1⁺PD-1⁺ (**m**) and TCF1⁻PD-1⁺ (**n**) in CD8⁺ T cells isolated from tumour tissues in WT and *Cd160*$^{-/-}$ mice, as shown in **e** ($n = 6$ mice). Data are shown as the mean ± s.e.m. *P* values were determined by unpaired two-tailed Student's *t*-tests (**c**, **d**, **g**, **i**, **k**, **m** and **n**).

$CD160^+CD8^+$ and $GzmB^+CD8^+$ T cells were observed, indicating successful TME infiltration and enhanced $CD8^+$ T cell cytotoxicity (Fig. 4p and Extended Data Fig. 6g–i). Second, $CD160^+CD8^+$ T cells were injected after 7 days of MC38 inoculation, once tumours were established, to evaluate their effect on later tumour development (Extended Data Fig. 6j). Similarly, $CD160^+CD8^+$ T cells suppressed tumour growth with maintained TME infiltration and GzmB expression (Extended Data Fig. 6k–p). Notably, in both experiments (Fig. 4n and Extended Data Fig. 6k), $CD160^-CD8^+$ T cells showed no evidence of an antitumour effect.

In the poor immunogenic CT26 model[31], $CD160^+CD8^+$ T cells failed to inhibit tumour growth (Extended Data Fig. 7a–j), despite infiltrating into tumours (Extended Data Fig. 7d,i), demonstrating that the antitumour effects of $CD160^+CD8^+$ T cells depend on tumour immunogenicity.

CD160 deficiency promotes terminal exhaustion of $CD8^+$ T cells and impairs $CD8^+$ T cell-mediated tumour control

To understand the impact of CD160 deficiency on tumour control, we generated *Cd160* knockout ($Cd160^{-/-}$) mice and evaluated tumour progression using AOM/DSS and subcutaneous MC38 models (Fig. 5a,e and Extended Data Fig. 7k–n). In both tumour models, $Cd160^{-/-}$ mice developed more numerous and larger tumours than wild-type (WT) mice. Notably, transfer of syngeneic $CD160^+CD8^+$ T cells markedly inhibited tumour growth in $Cd160^{-/-}$ mice, while $CD160^-CD8^+$ T cells exhibited no therapeutic effect (Fig. 5b–d,f,g). Additionally, $Cd160^{-/-}$ mice showed reduced tumour-infiltrating $GzmB^+CD8^+$ T cells, which was rescued by transfer of $CD160^+CD8^+$ T cells (Fig. 5h,i and Extended Data Fig. 7o,p). These results were further confirmed by immunohistochemistry (IHC) of tumour sections (Fig. 5j,k).

We further analysed tumour-infiltrating $CD8^+$ T cell exhaustion phenotypes (progenitor, $TCF1^+PD\text{-}1^+$; terminal, $TCF1^-PD\text{-}1^+$)[32,33]. $Cd160^{-/-}$ mice exhibited fewer progenitor and more terminally exhausted $CD8^+$ T cells (Fig. 5l–n). Transferring $CD160^+CD8^+$ T cells into $Cd160^{-/-}$ mice largely restored $TCF1^+PD\text{-}1^+$ proportions without affecting the fraction of $TCF1^-PD\text{-}1^+$ cells, whereas transfer of same number of $CD160^-CD8^+$ T cells had no effect (Fig. 5l–n). These observations collectively suggest that CD160 deficiency impairs $CD8^+$ T cell cytotoxicity, accelerates CRC progression and depletes anti-PD-1-responsive progenitor-exhausted T cells, supporting the therapeutic potential of $CD160^+CD8^+$ T cells for improving anti-PD-1 immunotherapy.

Transfer of $CD160^+CD8^+$ T cells confers anti-PD-1 immunotherapy sensitivity and overcomes anti-PD-1 resistance in MSI-H CRC

We next assessed whether the transfer of $CD160^+CD8^+$ T cells potentiates anti-PD-1 efficacy in MC38 tumours (Fig. 6a). Surprisingly, $CD160^+CD8^+$ T cells combined with anti-PD-1 induced near-complete tumour regression, outperforming either monotherapy, whereas $CD160^-CD8^+$ T cells failed to enhance anti-PD-1 efficacy (Fig. 6b,c). After infiltrating tumours, $CD160^+CD8^+$ T cells increased the proportion of $GzmB^+CD8^+$ T cells, especially in the combination group (Fig. 6d and Extended Data Fig. 8a–c).

Blocking terminally exhausted $CD8^+$ T cell accumulation during anti-PD-1 therapy by tipping the balance towards progenitor-exhausted T cells is vital to improve response[32]. We found that $CD160^+CD8^+$ T cells alone or combined with anti-PD-1 significantly raised the percentage of $TCF1^+PD\text{-}1^+$ in tumour-infiltrating $CD8^+$ T cells without affecting the $TCF1^-PD\text{-}1^+$ level (Fig. 6e and Extended Data Fig. 8d,e). Multiplex IHC further confirmed increased progenitor-exhausted $CD8^+$ T cells in mice treated with $CD160^+CD8^+$ T cells alone or combined with anti-PD-1 (Fig. 6f,g). In AOM/DSS-induced CRC mice, anti-PD-1 alone showed no significant effect, but combined with $CD160^+CD8^+$ T cells markedly reduced tumour burden (Extended Data Fig. 8f–i). Moreover, $CD160^+CD8^+$ T cells alone failed to prolong survival, but when combined with anti-PD-1 modestly improved survival (Extended Data Fig. 8j).

Despite the promising efficacy of anti-PD-1 immunotherapy in MSI-H patients with CRC, approximately 50% of such patients exhibit anti-PD-1 resistance[34]. To further confirm the relationship between *CD160* and anti-PD-1 response, we collected 13 MSI-H patients with CRC who received anti-PD-1 treatment (Supplementary Table 4). Response was defined by tumour regression grade (TRG): sensitive (TRG <2, $n = 8$) or resistant (TRG ≥2, $n = 5$) (Fig. 6h). Computed tomography confirmed sustained primary tumour remission after anti-PD-1 therapy in the sensitive group and large residual tumours in the resistant group (Fig. 6i). Indeed, we observed significantly higher CD160 expression among tumour-infiltrating $CD8^+$ T cells in the sensitive group (Fig. 6j,k). Consistently, in an independent CRC cohort that received first-line ICB therapy[19], high expression of CD160 predicted improved survival (Fig. 6l), independent of $CD8^+$ T cell infiltration (Extended Data Fig. 8k,l). Complete responders had higher *CD160* expression, despite being not statistically significant due to the small cohort size.

To further explore whether $CD160^+CD8^+$ T cells overcome anti-PD-1 resistance in MSI-H CRC, we established an anti-PD-1-resistant MC38 tumour model via multiple iterations of anti-PD-1 treatment until

Fig. 6 | Tumour-infiltrating $CD160^+CD8^+$ T cells confer sensitivity to immunotherapy and overcome resistance to anti-PD-1 in MSI-H CRC. a, The experimental scheme for adoptive T cell transfer combined with anti-PD-1 therapy in MC38 tumour-bearing mice. Splenic $CD160^{+/-}CD8^+$ T cells from normal syngeneic C57BL/6 mice were transferred via tail vein injection, while MC38 tumour-bearing mice were administrated anti-PD-1 at the indicated time points. **b**,**c**, Representative tumour images (**b**) and tumour volume (**c**) in MC38 tumour-bearing mice, as shown in **a** ($n = 6$ mice). **d**,**e**, Frequencies of GzmB (**d**) and $TCF1^+PD\text{-}1^+$ (**e**) in $CD8^+$ T cells isolated from tumour tissues in MC38 tumour-bearing mice, as shown in **a** ($n = 6$ mice). **f**,**g**, Representative multiplex IHC staining (**f**) and quantification of $TCF1^+TIM3^-PD\text{-}1^+CD8^+$ (**g**) in tumour tissues from MC38 tumour-bearing mice. Staining for DAPI (blue), CD8 (green), TCF1 (yellow), TIM3 (orange) and PD-1 (red). The red triangles highlight $TCF1^+TIM3^-PD\text{-}1^+CD8^+$ cells. Scale bars, 50 μm ($n = 6$ mice). **h**, A pie chart showing the proportion of TRG in MSI-H patients with CRC received anti-PD-1 therapy ($n = 13$ samples). **i**, Representative computed tomography scans of MSI-H patients with CRC with sensitive response and resistant response before and after anti-PD-1 therapy. Images of the primary tumour are delineated by solid red lines. **j**,**k**, Representative immunofluorescence staining (**j**) and quantification (**k**) in the sensitive response group and resistant response group of MSI-H patients with CRC after anti-PD-1 therapy. Staining for CD8 (green), CD160 (red) and DAPI (blue). Red triangles highlight $CD160^+CD8^+$ T cells. Scale bars, 50 μm ($n = 13$ samples). **l**, Association between CD160 and response to immunotherapy. Box plots show the *CD160* expression across different response groups of patients with CRC that received first-line immunotherapy (CR, $n = 6$; PR, $n = 17$; SD $n = 11$). CR, complete response; PR, partial response; SD, stable disease. *P* values were determined by paired two-sided Mann–Whitney tests. Kaplan–Meier curves display the progression-free survival (PFS) between patients with CRC grouped by the high or low expression of *CD160*. *P* values were determined by the log-rank test. The plus signs indicate censored data points. **m**, The experimental scheme for establishing the anti-PD-1 resistant MC38 tumour model and combining adoptive T cell transfer with anti-PD-1 therapy in this model. Splenic $CD160^{+/-}CD8^+$ T cells from normal syngeneic C57BL/6 mice were transferred via tail vein injection, while MC38 tumour-bearing mice were administrated anti-PD-1 at the indicated time points. **n**,**o**, Representative tumour images (**n**) and tumour volume (**o**) in the anti-PD-1-resistant model mice, as shown in **m** ($n = 6$ mice). **p**,**q**, The frequencies of $GzmB^+$ (**p**) and $TCF1^+PD\text{-}1^+$ (**q**) in $CD8^+$ T cells isolated from tumour tissues in anti-PD-1 resistant model mice, as shown in **m** ($n = 6$ mice). Data are shown as the mean ± s.e.m. *P* values were determined by unpaired two-tailed Student's *t*-tests (**c**–**e**, **g**, **k**, **o**, **p** and **q**). In the box plots, the centre line is the median, box limits are the first and third quartiles and whiskers are 1.5× interquartile range. i.p., intraperitoneal; i.v., intravenous; s.c., subcutaneous.

https://doi.org/10.1038/s41556-025-01753-3

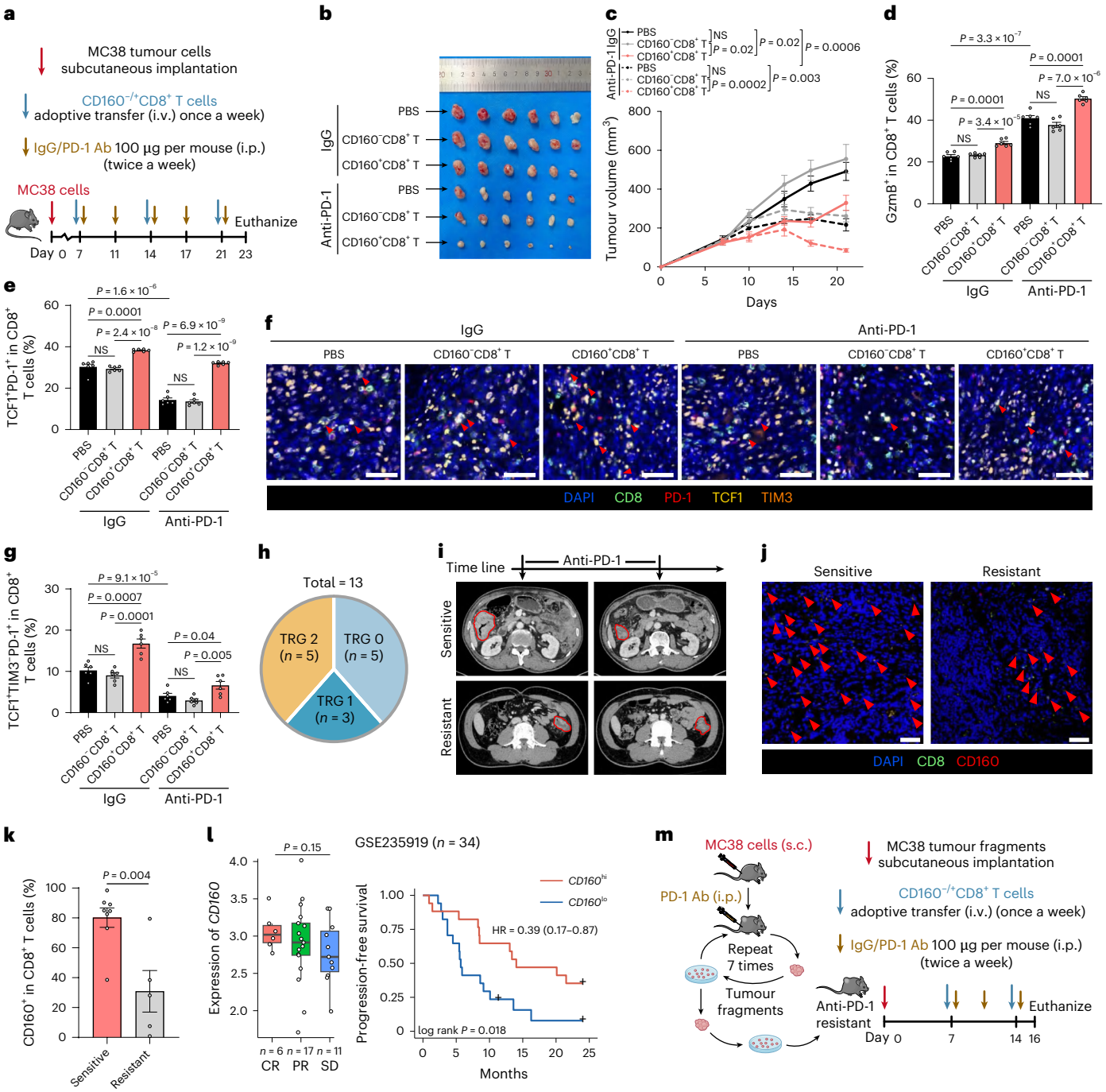

https://doi.org/10.1038/s41556-025-01753-3

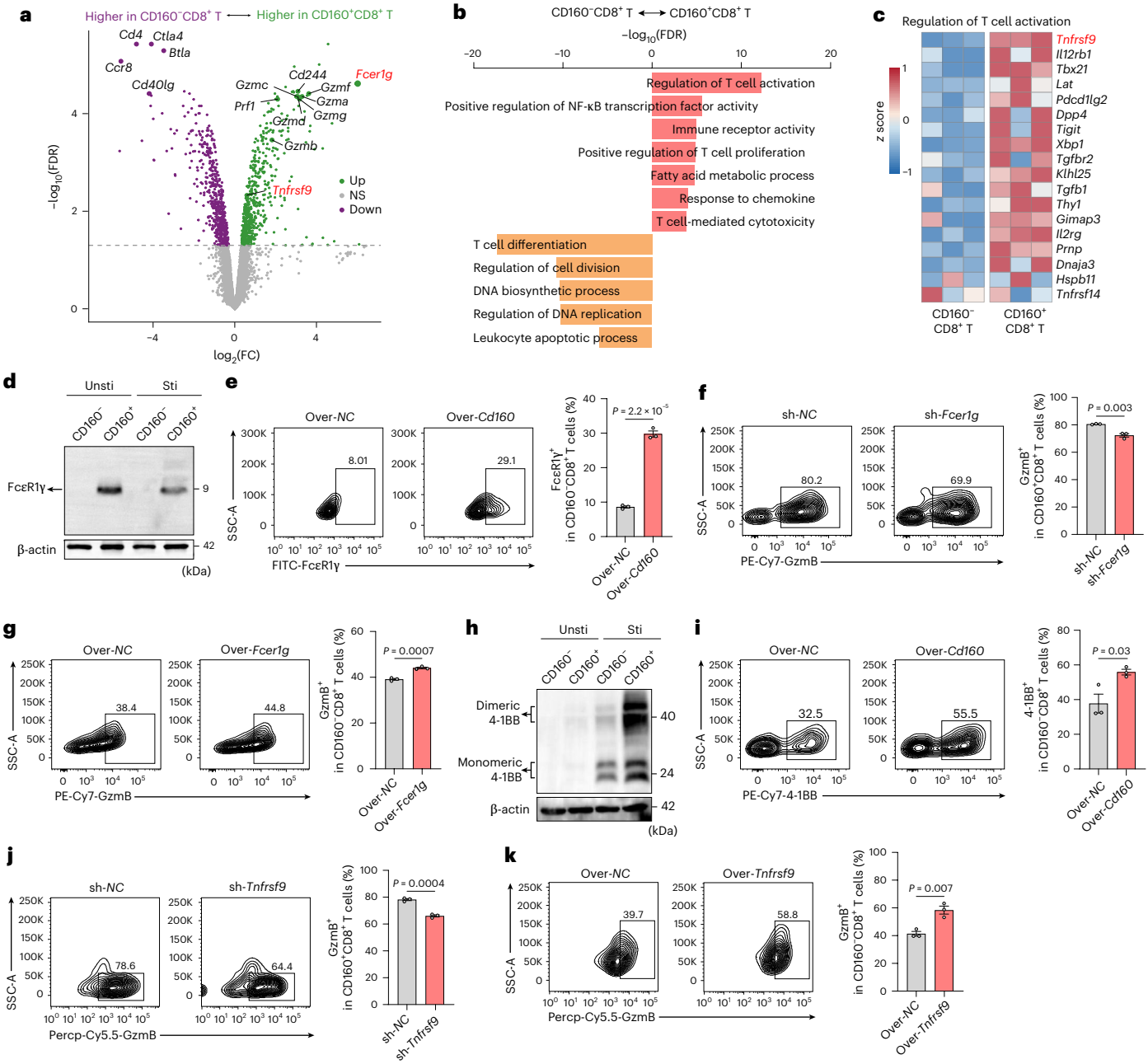

Fig. 7 | CD160 enhances CD8⁺ T cell cytotoxicity by upregulating FcεR1γ and 4-1BB expression. a, A volcano plot showing the DEGs in CD160$^{-/+}$CD8$^+$ T cells isolated from the spleen of normal C57BL/6 mice ($n = 3$ mice). The horizontal dashed line represents the statistical significance threshold (adjusted P value = 0.05). **b**, GO enrichment analysis of DEGs between CD160$^{-/+}$CD8$^+$ T cells. **c**, Heat maps showing the normalized expression of genes involved in the regulation of T cell activation for CD160$^{-/+}$CD8$^+$ T cells. Red font in **a** and **c** highlights the differentially expressed genes (DEGs) between CD160$^-$ and CD160$^+$ groups that are closely associated with T cell function, which were the focus of our study. **d**, Representative images of FcεR1γ protein expression in CD160$^{-/+}$CD8$^+$ T cells with (sti) or without (unsti) anti-CD3/CD28 stimulation for 24 h. **e**, Representative flow cytometry plots and frequencies of FcεR1γ$^+$ cells in CD160$^-$CD8$^+$ T cells overexpressing *Cd160* detected by flow cytometry ($n = 3$ biological replicates). **f**, Representative flow cytometry plots and frequencies of GzmB$^+$ cells in CD160$^+$CD8$^+$ T cells after knocking down *Fcer1g* ($n = 3$ biological replicates). **g**, Representative flow cytometry plots and frequencies of GzmB$^+$ cells in CD160$^-$CD8$^+$ T cells overexpressing *Fcer1g* ($n = 3$ biological replicates). **h**, Representative images of 4-1BB protein expression in CD160$^{-/+}$CD8$^+$ T cells. **i**, Representative flow cytometry plots and frequencies of 4-1BB$^+$ cells in CD160$^-$CD8$^+$ T cells overexpressing *Cd160* ($n = 3$ biological replicates). **j**, Representative flow cytometry plots and frequencies of GzmB$^+$ cells in CD160$^+$CD8$^+$ T cells after knocking down *Tnfrsf9* ($n = 3$ biological replicates). **k**, Representative flow cytometry plots and frequencies of GzmB$^+$ cells in CD160$^-$CD8$^+$ T cells overexpressing *Tnfrsf9* ($n = 3$ biological replicates). Data are shown as the mean ± s.e.m. P values were determined by unpaired two-tailed Student's t-tests (**e**–**g** and **i**–**k**).

tumour inhibition effect was no longer observable (Fig. 6m–o). Transfer of CD160$^+$CD8$^+$ T cells restored anti-PD-1 sensitivity, leading to near-complete tumour regression (Fig. 6n,o). These coincided with increased tumour-infiltrating GzmB$^+$CD8$^+$ T cells and progenitor-exhausted T cells (Fig. 6p,q and Extended Data Fig. 8m,n). However, CD160$^-$CD8$^+$ T cells had no such effects. Thus, these results suggest that CD160$^+$CD8$^+$ T cells confer immunotherapy sensitivity and overcome anti-PD-1 resistance in MSI-H CRC.

CD160–PI3K interaction enhances CD8$^+$ T cell cytotoxicity by promoting FcεR1γ and 4-1BB expression

To explore the function of CD160 in CD8$^+$ T cells, we compared transcriptomes between CD160$^+$CD8$^+$ and CD160$^-$CD8$^+$ T cells sorted from mouse spleens. CD160$^+$CD8$^+$ T cells showed robust upregulation of Fcer1g (Fig. 7a), known for transducing activation signals from immune receptors[35]. Gene Ontology (GO) enrichment demonstrated upregulated pathways in T cell activation, NF-κB regulation and T cell-mediated cytotoxicity (Fig. 7b). Among T cell activation pathway-related genes, *Tnfrsf9*, a downstream effector of CD160 involved in CD8$^+$ T cell survival and memory formation[36], was highly upregulated in CD160$^+$CD8$^+$ T cells (Fig. 7c).

At the mRNA/protein level, Fcer1g (encoding FcεR1γ) was significantly higher in CD160$^+$CD8$^+$ T cells (Fig. 7d and Extended Data Fig. 9a). *Cd160* overexpression in CD160$^-$CD8$^+$ T cells induced FcεR1γ expression, while *Fcer1g* knockdown decreased GzmB expression in CD160$^+$CD8$^+$ T cells, reducing their cytotoxicity. Conversely, *Fcer1g* overexpression enhanced CD160$^-$CD8$^+$ T cell cytotoxicity (Fig. 7e–g and Extended Data Fig. 9b–d). Similarly, *Tnfrsf9* (encoding 4-1BB) was elevated in CD160$^+$CD8$^+$ T cells, with *Cd160* overexpression induced 4-1BB expression (Fig. 7h,i and Extended Data Fig. 9e). Silencing *Tnfrsf9* reduced the GzmB level in CD160$^+$CD8$^+$ T cells, while *Tnfrsf9* overexpression augmented CD160$^-$CD8$^+$ T cell cytotoxicity (Fig. 7j,k and Extended Data Fig. 9f,g). Meanwhile, tumour-infiltrating CD160$^+$CD8$^+$ T cells from patients with CRC and MC38 tumour-bearing mice maintained significantly higher FcεR1γ and 4-1BB expression than CD160$^-$CD8$^+$ T cells (Extended Data Fig. 9h–m). Thus, these results indicate that FcεR1γ and 4-1BB are key downstream effectors for CD160 to enhance CD160$^+$CD8$^+$ T cell cytotoxicity.

We next interrogated how CD160 regulates Fcer1g and Tnfrsf9 expression in CD8$^+$ T cells. NF-κB is the transcription factor for *Fcer1g* and *Tnfrsf9* (ref. 37) and GO analysis indicated enrichment of NF-κB signalling in CD160$^+$CD8$^+$ T cells. Compared with CD160$^-$CD8$^+$ T cells, CD160$^+$CD8$^+$ T cells upregulated the classical NF-κB pathway (p65) but not the nonclassical pathway (p52) (Extended Data Fig. 9n). Immunofluorescence and nuclear/cytoplasmic blots showed significant nuclear translocation of NF-κB p65 in CD160$^+$CD8$^+$ T cells, whereas they failed to enter the nucleus in CD160$^-$CD8$^+$ T cells (Fig. 8a–c). Blocking NF-κB nuclear translocation with JSH-23 reduced *Fcer1g* and *Tnfrsf9* expression, indicating that CD160 promotes their transcription via NF-κB (Fig. 8d).

The PI3K-AKT pathway, critical for T cell activation, proliferation, cytotoxicity and NF-κB nuclear translocation[38,39], was upregulated in CD160$^+$CD8$^+$ T cells by Gene Set Enrichment Analysis (GSEA) (Fig. 8e), with an increased p-AKT level (Fig. 8f). Class I PI3K is a heterodimer composed of a catalytic subunit (p110) and a regulatory subunit (p85)[40]. To determine whether CD160 activates the PI3K–AKT pathway by direct interaction with PI3K subunits, we performed endogenous co-immunoprecipitation (co-IP) in CD160$^+$CD8$^+$ T cells. Notably, CD160 robustly bound to p85α and weakly to p110δ under similar exposure conditions, with no detectable interaction with p110α, p110β or p110γ (Fig. 8g). This interaction specificity was confirmed in HEK293T cells co-transfected with HA-tagged CD160 and Flag-tagged PI3K p85α or p110δ, where HA-CD160 preferentially bound to p85α (Extended Data Fig. 9o). A proximity ligation assay (PLA) further revealed direct CD160–p85α interaction in CD160$^+$CD8$^+$ T cells, but not in CD160$^-$ counterparts (Fig. 8h and Extended Data Fig. 9p). Molecular dynamics simulations and docking analyses showed that the CD160–p85α complex displays a higher binding stability than complexes with other PI3K subunits (Fig. 8i and Extended Data Fig. 9q). Functionally, p85α knockdown in CD160$^+$CD8$^+$ T cells abolished CD160-mediated GzmB expression and AKT phosphorylation, whereas p110δ knockdown had no effect (Fig. 8j,k and Extended Data Fig. 9r). Collectively, these findings demonstrate that CD160 enhances CD8$^+$ T cell cytotoxicity by directly interacting with p85α to activate the AKT–NF-κB pathway, thereby promoting FcεR1γ and 4-1BB expression.

Discussion

The colon, though smaller in surface area, is more prone to tumour development than the ileum. The underlying role of the immune microenvironment in the colon and ileum is being increasingly recognized[41]. By integrating scRNA/BCR/TCR-seq and bulk RNA-seq datasets from patients with CRC and healthy donors, we mapped immune landscapes across different intestinal tissues and revealed a progressive decline of CD160$^+$CD8$^+$ T cells from ileum/colon to tumours. These cells exhibit previously unrecognized characteristics, including high cytotoxicity, strong clonal expansion and resistance to terminal exhaustion. Functional studies confirmed their role in inhibiting CRC growth and sensitizing MSI-H CRC to anti-PD-1 therapy. Mechanistically, CD160 directly interacts with PI3K p85α to promote FcεR1γ and 4-1BB expression, ultimately enhancing CD8$^+$ T cell cytotoxicity (Fig. 8l).

Recent single-cell transcriptomic studies have described differences between colon and ileum, but these were limited to mouse models or patients without cancer[9,42]. Our study integrated CRC samples with colon and ileum samples, and identified extensive remodelling of PCs and T cell state transitions between colon and ileum that were embodied in heterogeneous TME across tumours. The most obvious T cell state transition occurs within IEL-T cells, including γδT cells and TCRαβ$^+$ IEL-T cells. γδT cells are critical for early CRC control and constitute a major lymphocyte population infiltrating tumour[6]. However, long-term exposure to the TME drives their transition into a pro-tumorigenic state, characterized by the loss of cytotoxic markers[6,43]. These align with our observations that γδT cells exhibit higher cytolytic activity in ileum than in colon and the lowest in tumours. TCRαβ$^+$ IEL-T cells play a key role in maintaining the intestinal epithelial cell barrier[43], but their role in antitumour immunity remains unclear. Our study indicates that they show significantly higher terminal exhaustion in colon and tumour tissues than in ileum tissue. We suspect this T cell dysfunction may associate with a higher fraction of TGF-β$^+$ LLPCs in these regions as TGF-β promotes T cell exhaustion[44] and regulates IEL epithelial adhesion[45], consistent with a strong interaction between LLPCs and exhausted IEL-T cells in our single-cell dataset.

Fig. 8 | CD160 interacts with PI3K p85α to promote NF-κB nuclear translocation. a,**b**, Representative images (**a**, top), line charts of the fluorescence signal positioning (**a**, bottom) and quantification (**b**) of immunofluorescence staining displaying the subcellular distribution of NF-κB p65 in CD160$^{-/+}$CD8$^+$ T cells with or without anti-CD3/CD28 stimulation for 24 h. Staining for DAPI (blue) and NF-κB p65 (green). Scale bars, 5 μm (n = 15 biological replicates). **c**, Representative images of NF-κB p65 nuclear and cytoplasmic protein expression in CD160$^{-/+}$CD8$^+$ T cells with or without anti-CD3/CD28 stimulation for 24 h. **d**, Relative mRNA expression of *Fcer1g* and *Tnfrsf9* in CD160$^+$CD8$^+$ T cells treated with dimethylsulfoxide (DMSO) or the NF-κB inhibitor, JSH-23 for 24 h with or without anti-CD3/CD28 stimulation (n = 3 biological replicates). **e**, GSEA of the PI3K–AKT signalling pathway in CD160$^{-/+}$CD8$^+$ T cells. NES, normalized enrichment score. **f**, Representative images of p-AKT, AKT protein expression in CD160$^{-/+}$CD8$^+$ T cells with or without anti-CD3/CD28 stimulation for 30 min. **g**, Co-IP assays showing the binding of PI3K subunits and CD160 analysed in CD160$^+$CD8$^+$ T cells. **h**, PLA signals between p85α and CD160 in CD160$^+$CD8$^+$ T cells. Scale bars, 10 μm. **i**, The predicted p85α–CD160 binding mode and its stability as evidenced by a plateaued root mean squared deviation (r.m.s.d.) curve of the interface residues along a 500 ns molecular dynamics simulation. **j**, Representative flow cytometry plots and frequencies of GzmB in CD160$^+$CD8$^+$ T cells following p85α and p110δ knockdown (n = 3 biological replicates). **k**, Representative images of p-AKT, AKT protein expression in CD160$^+$CD8$^+$ T cells following p85α and p110δ knockdown. **l**, A summary diagram of the main approaches and findings from this study. KO, knockout. Data are shown as the mean ± s.e.m. P values were determined by unpaired two-tailed Student's t-tests (**b**, **d** and **j**).

https://doi.org/10.1038/s41556-025-01753-3

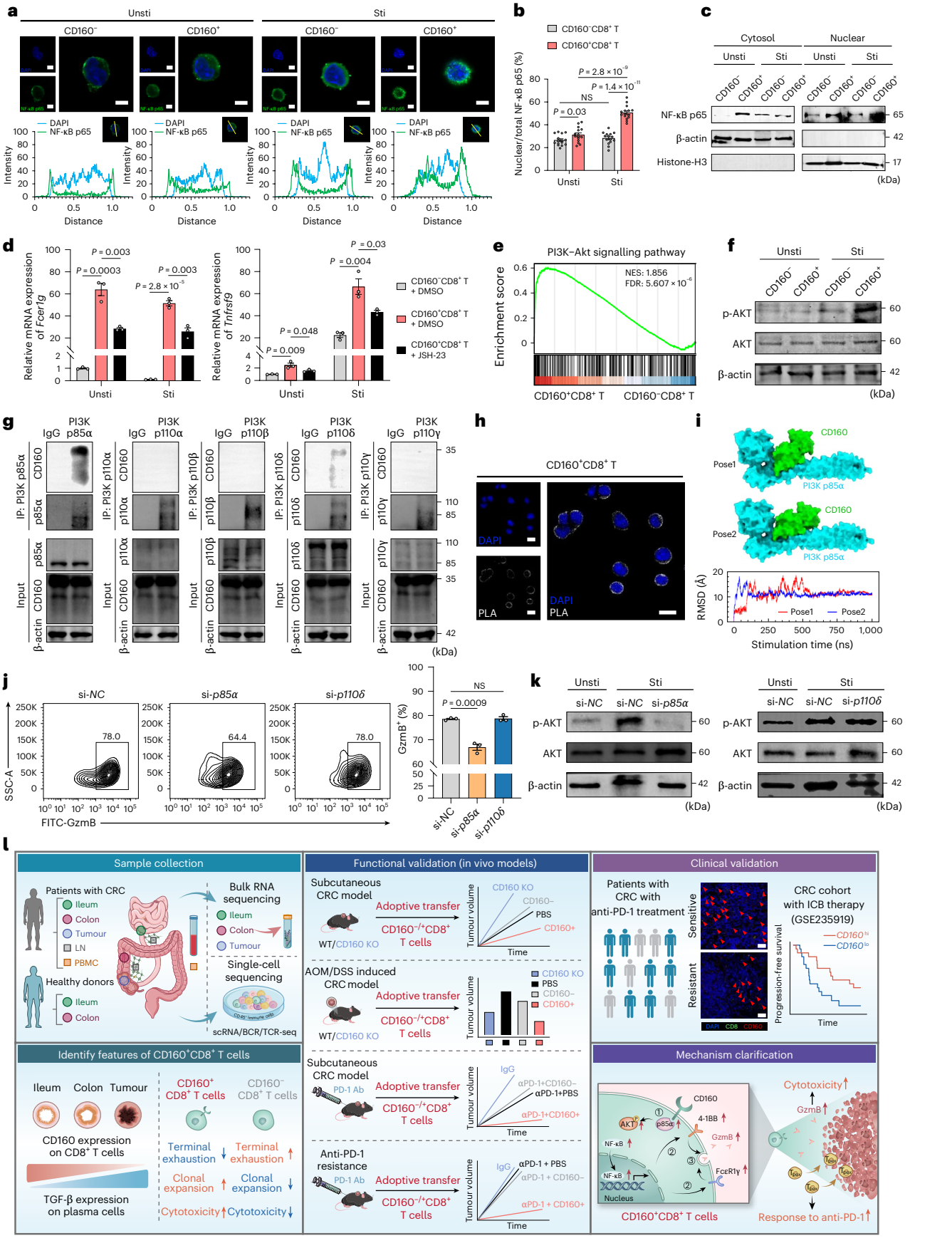

T cell state transitions across tissues are accompanied by extensive transcriptome reprogramming and, most significantly, the varied expression of *CD160*. CD160 is a lymphocyte surface protein that is expressed in spleen, PBMCs and small intestine tissues[46] and exhibits context-dependent immunosuppressive or immunostimulatory effects[47–50]. We confirmed that CD160 was widely expressed in $CD8^+$ T cells but not $CD4^+$ T cells, with $CD160^+CD8^+$ T cells highly enriched in ileum. Single-cell sequencing, in vitro and in vivo studies demonstrated that CD160 marked $CD8^+$ T cells that are highly cytotoxic and resistant to terminal exhaustion. Paired scRNA/TCR-seq data across tissues enabled lineage tracing, revealing that terminally exhausted $CD8^+$ T cells primarily linked to $CD160^-$ T cells. The majority of intratumour exhausted $CD8^+$ T cells were clonally linked to $CD8^+$ T cells from LNs, which were marked by low *CD160* expression and high *TCF7* and *SELL* expression, supporting recent reports that stem-like progenitor cells from LNs fuel the T cell response in cancer[50,51]. On the other hand, intratumoural $CD8^+$ T cells clonally linked to $CD160^+CD8^+$ T cells from ileum or colon were more likely to maintain a progenitor exhaustion state. Hence, our data substantiate a concept that $CD160^+CD8^+$ T cells sustain antitumour immunity and resist terminal exhaustion.

Our study holds important clinical implications. In vivo functional studies showed that T cells from $Cd160^{-/-}$ mice exhibited impaired antitumour activity, promoting CRC development. Notably, intravenously injected $CD160^+CD8^+$ T cells permeated into the TME, induced strong antitumour immunity and increased tumour-infiltrating $TCF1^+PD\text{-}1^+CD8^+$ T cells to confer anti-PD-1 sensitivity. However, an improved anti-PD-1 response may involve complex mechanisms, including potential effects on macrophages, neutrophils and DC cells, requiring further investigation[52–55]. Importantly, our analysis of independent ICB-treated MSI-H CRC cohorts confirmed that $CD160^+CD8^+$ T cells correlate with better immunotherapy response. Although previous studies have linked CD160 expression in gastric cancer[56], CRC[57], lung cancer[58] and chronic lymphocytic leukemia[59] to prognosis and immunotherapy response, which is consistent with our findings, the role of CD160 in immunotherapy and its underlying mechanisms remain unclear. Our study shows that the transfer of $CD160^+CD8^+$ T cells not only enhances MSI-H CRC sensitivity to anti-PD-1 treatment but also effectively overcomes their resistance. Notably, despite reduced $CD160^+CD8^+$ T cell fractions in tumours, many tumours still show a non-negligible presence of $CD160^+CD8^+$ T cells, suggesting the potential of benefit from immunotherapy.

Mechanistically, we identified an important function of $CD160^+CD8^+$ T cells, which promotes cytotoxicity via a direct reciprocal manner between CD160 and PI3K p85α. A previous study only found co-localization of CD160 and PI3K in NK cells by immunofluorescence[60], lacking reliable evidence for their relationship or specific PI3K subunits. We employed PLA, co-IP and molecular docking to definitively demonstrate the strong interaction between CD160 and PI3K p85α in $CD8^+$ T cells, which is an important discovery in elucidating the mechanism.

In summary, this work provides a unique single-cell resource with multiregional and clonal resolution of patients with CRC. We revealed tissue-specific characteristic of $CD160^+CD8^+$ T cells, which are highly enriched in ileum, and demonstrate their promising therapeutic potential in MSI-H CRC, where they can enhance anti-PD-1 efficacy and overcome its resistance, suggesting their important clinical translational value in pan-cancer treatment.

Online content

Any methods, additional references, Nature Portfolio reporting summaries, source data, extended data, supplementary information, acknowledgements, peer review information; details of author contributions and competing interests; and statements of data and code availability are available at https://doi.org/10.1038/s41556-025-01753-3.

References

1. Siegel, R. L., Miller, K. D., Wagle, N. S. & Jemal, A. Cancer statistics, 2023. *CA Cancer J. Clin.* **73**, 17–48 (2023).
2. Mayassi, T. et al. Spatially restricted immune and microbiota-driven adaptation of the gut. *Nature* **636**, 447–456 (2024).
3. Lowenfels, A. B. Why are small-bowel tumours so rare? *Lancet* **1**, 24–26 (1973).
4. Mowat, A. M. & Agace, W. W. Regional specialization within the intestinal immune system. *Nat. Rev. Immunol.* **14**, 667–685 (2014).
5. Anandakumar, H. et al. Segmental patterning of microbiota and immune cells in the murine intestinal tract. *Gut Microbes* **16**, 2398126 (2024).
6. Reis, B. S. et al. TCR-Vγδ usage distinguishes protumor from antitumor intestinal γδ T cell subsets. *Science* **377**, 276–284 (2022).
7. Morikawa, R. et al. Intraepithelial lymphocytes suppress intestinal tumor growth by cell-to-cell contact via CD103/E-cadherin signal. *Cell Mol. Gastroenterol. Hepatol.* **11**, 1483–1503 (2021).
8. Yakou, M. H. et al. TCF-1 limits intraepithelial lymphocyte antitumor immunity in colorectal carcinoma. *Sci. Immunol.* **8**, eadf2163 (2023).
9. Lin, Y. H. et al. Small intestine and colon tissue-resident memory $CD8^+$ T cells exhibit molecular heterogeneity and differential dependence on Eomes. *Immunity* **56**, 207–223.e8 (2023).
10. Pioli, P. D. Plasma cells, the next generation: beyond antibody secretion. *Front. Immunol.* **10**, 2768 (2019).
11. Lichterman, J. N. & Reddy, S. M. Mast cells: a new frontier for cancer immunotherapy. *Cells* **10**, 1270 (2021).
12. Zhang, L. et al. Lineage tracking reveals dynamic relationships of T cells in colorectal cancer. *Nature* **564**, 268–272 (2018).
13. Allison, M. C., Poulter, L. W., Dhillon, A. P. & Pounder, R. E. Immunohistological studies of surface antigen on colonic lymphoid cells in normal and inflamed mucosa. Comparison of follicular and lamina propria lymphocytes. *Gastroenterology* **99**, 421–430 (1990).
14. Trejdosiewicz, L. K. Intestinal intraepithelial lymphocytes and lymphoepithelial interactions in the human gastrointestinal mucosa. *Immunol. Lett.* **32**, 13–19 (1992).
15. Corridoni, D. et al. Single-cell atlas of colonic $CD8^+$ T cells in ulcerative colitis. *Nat. Med.* **26**, 1480–1490 (2020).
16. Chu, Y. et al. Pan-cancer T cell atlas links a cellular stress response state to immunotherapy resistance. *Nat. Med.* **29**, 1550–1562 (2023).
17. Zheng, L. et al. Pan-cancer single-cell landscape of tumor-infiltrating T cells. *Science* **374**, abe6474 (2021).
18. Lowery, F. J. et al. Molecular signatures of antitumor neoantigen-reactive T cells from metastatic human cancers. *Science* **375**, 877–884 (2022).
19. Thibaudin, M. et al. First-line durvalumab and tremelimumab with chemotherapy in RAS-mutated metastatic colorectal cancer: a phase 1b/2 trial. *Nat. Med.* **29**, 2087–2098 (2023).
20. Liu, Z. et al. Progenitor-like exhausted $SPRY1^+CD8^+$ T cells potentiate responsiveness to neoadjuvant PD-1 blockade in esophageal squamous cell carcinoma. *Cancer Cell* **41**, 1852–1870.e9 (2023).
21. Chen, D. et al. γδ T cell exhaustion: opportunities for intervention. *J. Leukoc. Biol.* **112**, 1669–1676 (2022).
22. Trapnell, C. et al. The dynamics and regulators of cell fate decisions are revealed by pseudotemporal ordering of single cells. *Nat. Biotechnol.* **32**, 381–386 (2014).
23. Sade-Feldman, M. et al. Defining T cell states associated with response to checkpoint immunotherapy in melanoma. *Cell* **175**, 998–1013.e20 (2018).
24. Paley, M. A. et al. Progenitor and terminal subsets of CD8+ T cells cooperate to contain chronic viral infection. *Science* **338**, 1220–1225 (2012).

25. Seo, G. Y. et al. Epithelial HVEM maintains intraepithelial T cell survival and contributes to host protection. *Sci. Immunol.* **7**, eabm6931 (2022).
26. Rey, J. et al. The co-expression of 2B4 (CD244) and CD160 delineates a subpopulation of human CD8$^+$ T cells with a potent CD160-mediated cytolytic effector function. *Eur. J. Immunol.* **36**, 2359–2366 (2006).
27. Del Rio, M. L. et al. Modulation of cytotoxic responses by targeting CD160 prolongs skin graft survival across major histocompatibility class I barrier. *Transl. Res.* **181**, 83–95.e3 (2017).
28. Pai, J. A. et al. Lineage tracing reveals clonal progenitors and long-term persistence of tumor-specific T cells during immune checkpoint blockade. *Cancer Cell* **41**, 776–790.e7 (2023).
29. Li, J. et al. Remodeling of the immune and stromal cell compartment by PD-1 blockade in mismatch repair-deficient colorectal cancer. *Cancer Cell* **41**, 1152–1169.e7 (2023).
30. Belk, J. A. et al. Genome-wide CRISPR screens of T cell exhaustion identify chromatin remodeling factors that limit T cell persistence. *Cancer Cell* **40**, 768–786.e7 (2022).
31. Klement, J. D. et al. Tumor PD-L1 engages myeloid PD-1 to suppress type I interferon to impair cytotoxic T lymphocyte recruitment. *Cancer Cell* **41**, 620–636.e9 (2023).
32. Miller, B. C. et al. Subsets of exhausted CD8$^+$ T cells differentially mediate tumor control and respond to checkpoint blockade. *Nat. Immunol.* **20**, 326–336 (2019).
33. Utzschneider, D. T. et al. T cell factor 1-expressing memory-like CD8$^+$ T cells sustain the immune response to chronic viral infections. *Immunity* **45**, 415–427 (2016).
34. André, T. et al. Pembrolizumab in microsatellite-instability-high advanced colorectal cancer. *N. Engl. J. Med.* **383**, 2207–2218 (2020).
35. Huang, C. et al. Antibody Fc-receptor FcεR1γ stabilizes cell surface receptors in group 3 innate lymphoid cells and promotes anti-infection immunity. *Nat. Commun.* **15**, 5981 (2024).
36. Zhang, L. et al. CD160 signaling is essential for CD8+ T cell memory formation via upregulation of 4-1BB. *J. Immunol.* **211**, 1367–1375 (2023).
37. Pichler, K. et al. Strong induction of 4-1BB, a growth and survival promoting costimulatory receptor, in HTLV-1-infected cultured and patients' T cells by the viral Tax oncoprotein. *Blood* **111**, 4741–4751 (2008).
38. Guo, Q. et al. NF-κB in biology and targeted therapy: new insights and translational implications. *Signal Transduct. Target Ther.* **9**, 53 (2024).
39. Shen, S. et al. The exoprotein Gbp of *Fusobacterium nucleatum* promotes THP-1 cell lipid deposition by binding to CypA and activating PI3K-AKT/MAPK/NF-κB pathways. *J. Adv. Res.* **57**, 93–105 (2024).
40. Castel, P., Toska, E., Engelman, J. A. & Scaltriti, M. The present and future of PI3K inhibitors for cancer therapy. *Nat. Cancer* **2**, 587–597 (2021).
41. Schrock, A. B. et al. Genomic profiling of small-bowel adenocarcinoma. *JAMA Oncol.* **3**, 1546–1553 (2017).
42. Kong, L. et al. The landscape of immune dysregulation in Crohn's disease revealed through single-cell transcriptomic profiling in the ileum and colon. *Immunity* **56**, 444–458.e5 (2023).
43. Hoytema van Konijnenburg, D. P. et al. Intestinal epithelial and intraepithelial T cell crosstalk mediates a dynamic response to infection. *Cell* **171**, 783–794.e13 (2017).
44. Chen, W. TGF-β regulation of T cells. *Annu. Rev. Immunol.* **41**, 483–512 (2023).
45. El-Asady, R. et al. TGF-β-dependent CD103 expression by CD8$^+$ T cells promotes selective destruction of the host intestinal epithelium during graft-versus-host disease. *J. Exp. Med.* **201**, 1647–1657 (2005).
46. Anumanthan, A. et al. Cloning of BY55, a novel Ig superfamily member expressed on NK cells, CTL, and intestinal intraepithelial lymphocytes. *J. Immunol.* **161**, 2780–2790 (1998).
47. Cai, G. et al. CD160 inhibits activation of human CD4$^+$ T cells through interaction with herpesvirus entry mediator. *Nat. Immunol.* **9**, 176–185 (2008).
48. Zhang, L. et al. CD160 plays a protective role during chronic infection by enhancing both functionalities and proliferative capacity of CD8$^+$ T cells. *Front. Immunol.* **11**, 2188 (2020).
49. Tu, T. C. et al. CD160 is essential for NK-mediated IFN-γ production. *J. Exp. Med.* **212**, 415–429 (2015).
50. Sun, H. et al. Reduced CD160 expression contributes to impaired NK-cell function and poor clinical outcomes in patients with HCC. *Cancer Res.* **78**, 6581–6593 (2018).
51. Yost, K. E. et al. Clonal replacement of tumor-specific T cells following PD-1 blockade. *Nat. Med.* **25**, 1251–1259 (2019).
52. Rao, G. et al. Anti–PD-1 induces M1 polarization in the glioma microenvironment and exerts therapeutic efficacy in the absence of CD8 cytotoxic T cells. *Clin. Cancer Res.* **26**, 4699–4712 (2020).
53. Luo, Q. et al. Apatinib remodels the immunosuppressive tumor ecosystem of gastric cancer enhancing anti-PD-1 immunotherapy. *Cell Rep.* **42**, 112437 (2023).
54. Gordon, S. R. et al. PD-1 expression by tumour-associated macrophages inhibits phagocytosis and tumour immunity. *Nature* **545**, 495–499 (2017).
55. Hirschhorn, D. et al. T cell immunotherapies engage neutrophils to eliminate tumor antigen escape variants. *Cell* **186**, 1432–1447. e17 (2023).
56. Wang, J. et al. Intratumoral CXCL13$^+$ CD160$^+$ CD8$^+$ T cells promote the formation of tertiary lymphoid structures to enhance the efficacy of immunotherapy in advanced gastric cancer. *J. Immunother. Cancer* **12**, e009603 (2024).
57. Li, J. et al. Biomarkers of pathologic complete response to neoadjuvant immunotherapy in mismatch repair-deficient colorectal cancer. *Clin. Cancer Res.* **30**, 368–378 (2024).
58. Liao, J. et al. Plasma extracellular vesicle transcriptomics identifies CD160 for predicting immunochemotherapy efficacy in lung cancer. *Cancer Sci.* **114**, 2774–2786 (2023).
59. Bozorgmehr, N. et al. Expanded antigen-experienced CD160$^+$CD8$^+$ effector T cells exhibit impaired effector functions in chronic lymphocytic leukemia. *J. Immunother. Cancer* **9**, e002189 (2021).
60. Rabot, M. et al. CD160-activating NK cell effector functions depend on the phosphatidylinositol 3-kinase recruitment. *Int. Immunol.* **19**, 401–409 (2007).

Publisher's note Springer Nature remains neutral with regard to jurisdictional claims in published maps and institutional affiliations.

Springer Nature or its licensor (e.g. a society or other partner) holds exclusive rights to this article under a publishing agreement with the author(s) or other rightsholder(s); author self-archiving of the accepted manuscript version of this article is solely governed by the terms of such publishing agreement and applicable law.

© The Author(s), under exclusive licence to Springer Nature Limited 2025

[1]Key Laboratory of Molecular Oncology of Heilongjiang Province, Harbin, China. [2]Department of Gastrointestinal Medical Oncology, Harbin Medical University Cancer Hospital, Harbin, China. [3]School of Basic Medical Sciences, Harbin Medical University, Harbin, China. [4]Department of Pathology, Harbin Medical University, Harbin, China. [5]Department of Pathology, Harbin Medical University Cancer Hospital, Harbin, China. [6]Department of Colorectal Surgery, Harbin Medical University Cancer Hospital, Harbin, China. [7]Departments of General Surgery, First Affiliated Hospital of Harbin Medical University, Harbin, China. [8]Department of Hepatic Surgery, Second Affiliated Hospital of Harbin Medical University, Harbin, China. [9]College of Bioinformatics Science and Technology, NHC Key Laboratory of Molecular Probe and Targeted Diagnosis and Therapy, Harbin Medical University, Harbin, China. [10]Research Center for Pharmacoinformatics (The State-Province Key Laboratories of Biomedicine-Pharmaceutics of China), College of Pharmacy, Harbin Medical University, Harbin, China. [11]NHC Key Laboratory of Molecular Probes and Targeted Diagnosis and Therapy, Harbin Medical University, Harbin, China. [12]McKusick-Zhang Center for Genetic Medicine, Institute of Basic Medical Sciences, Chinese Academy of Medical Sciences and Peking Union Medical College, Beijing, China. [13]Present address: Department of Hepatobiliary and Pancreatic Surgery, Harbin Medical University Cancer Hospital, Harbin, China. [14]These authors contributed equally: Tongsen Zheng, Chujie Ding, Shihui Lai, Yang Gao. ✉e-mail: zhengtongsen@hrbmu.edu.cn; dapenghao@hrbmu.edu.cn; xuezhang@hrbmu.edu.cn

Methods

Ethical statement

This study was approved by the Institutional Reviewer Board (IRB) of Harbin Medical University (IRB reference HMUIRB2023001). Experiments involving human participants were done according to the recommendations of the research and ethics committee. This study follows the principles according to the Declaration of Helsinki, with fully informed consent obtained from all participants before sample collection. All mice experiments were approved by the Institutional Animal Care and Use Committee of Harbin Medical University.

Human specimens

All sample collection procedures complied with the regular routine in clinical practice. Nineteen patients with primary colon cancer who underwent right hemicolectomy and pathologically diagnosed with colon adenocarcinoma at Harbin Medical University Cancer Hospital were enrolled for sequencing in this study. None of the 19 patients had received neoadjuvant chemotherapy before tumour resection. Paired, fresh tumour, adjacent normal colon, ileum tissues and lymph nodes were surgically removed from patients. Typical lesions from the core site of the pathological entity were collected as the tumour sample, while disease-free mucosa at least 5 cm away from the lesion edge was acquired as adjacent normal control. Peripheral blood samples were collected before the surgery through venipuncture or implanted vascular access ports. Healthy donor intestines were procured from eight brain-dead organ donors from The First Affiliated Hospital of Harbin Medical University, The Second Affiliated Hospital of Harbin Medical University and The First Affiliated Hospital of USTC.

In all cases (patients and healthy donors), fresh samples collected directly during standard surgical procedures were transported in sterile saline and preserved by MACS Tissue Storage Solution (Miltenyi Biotec) at 4 °C for scRNA/BCR/TCR-seq or preserved by RNALater (Thermo Fisher) in liquid nitrogen for bulk RNA-seq. In detail, 62 samples from 10 patients underwent scRNA/BCR/TCR-seq, and 26 samples from another 9 patients were sequenced by bulk RNA-seq. Another 6 samples from 3 healthy donors underwent scRNA/BCR/TCR-seq, and 10 samples from 5 healthy donors were sequenced by bulk RNA-seq. Clinical information and metadata for the above samples are provided in Supplementary Table 1.

For the MSI-H CRC samples, 13 patients genetically diagnosed with MSI-H and histologically confirmed CRC from Sun Yat-sen University Cancer Center, who were treated with PD-1 blockade therapy as neoadjuvant treatment were retrospectively enrolled. Patients who received postoperative PD-1 blockade or without determination of tumour response were excluded. Pathological tumour responses were determined using the TRG grading scale as described previously[61]. Tumour tissues and paraffin-embedded formalin-fixed slides were obtained from the 13 patients with CRC who underwent surgery after PD-1 blockade therapy. Clinical information for the above samples are provided in Supplementary Table 4.

Mice

Male C57BL/6 and Balb/c mice (6–8 weeks old) were purchased from Liaoning Changsheng Biotechnology Co. Ltd, while B6-H11-CAG-EGFP, CD45.1 congenic mice and *Cd160* knockout (*Cd160*$^{-/-}$) mice on a C57BL/6 background were purchased from GemPharmatech Co. Ltd. For animal experiments with knockout mice, WT littermate controls on the same C57BL/6 background at the age of 6–10 weeks were used. Mice were housed in a controlled, specific pathogen-free environment and received humane care in accordance with the animal welfare guidelines. All animal experiments were approved by the Animal Care Committee of Harbin Medical University. All mice were maintained under the conditions of pathogen-free, 12 h light/12 h dark cycle, temperatures of 18–23 °C and 40–60% humidity.

Cell lines and cell culture

Murine MC38 (MSI-H)[62,63], MC38-OVA, MC38-GFP and HEK293T cells were cultured in DMEM (Gibco) with 10% fetal bovine serum (FBS, Gibco) and 1% penicillin/streptomycin (Beyotime). Murine CT26 (microsatellite stable, MSS)[64] cells were cultured in RPMI-1640 medium (Gibco) containing 1% penicillin/streptomycin and 10% FBS. All cells were performed to subculture in a 37 °C cell incubator with 5% CO_2.

Single-cell library construction and sequencing

Fresh intestine tissues and lymph node tissues were immediately minced into 1–2 mm^3 and enzymatically digested with gentleMACS (Miltenyi) using a constant temperature shaker at 37 °C following the manufacturer's instruction (Tumor Dissociation Kit). Briefly, cells from tissues or PBMCs were subsequently filtered, counted and stained with antibodies against 7-AAD and CD45, followed by FACS sorting to obtain viable CD45$^+$ single cells on a BD Melody instrument. CD45$^+$ single cells were loaded into the chip with the position of 18,000 cells using the 10X Chromium Single Cell V(D)J Reagent kits v2. Then, 10,000 cells were collected in droplets to produce nanolitre-scale gel bead in emulsion according to the manufacturer's procedure (Chromium Next GEM Single Cell 5′ Reagent kits v2). ScRNA, TCR V(D)J and BCR V(D)J libraries sequencing were performed on an Illumina NovaSeq 6000 sequencer with 150 bp paired-end reads.

Single-cell raw data processing

Raw scRNA-seq data were preprocessed using CellRanger Single Cell Software Suite (v6.1.2, 10X Genomics) by mapping to human reference genome build 38. Filtered gene-barcode matrices that contained only barcodes with UMI counts that passed the threshold for cell detection were used for further analysis. Cells expressing fewer than 200 genes or more than 5,000 genes were considered low-quality or potential doublets and were removed. Likely apoptotic cells where >10% transcripts were derived from the mitochondrial genome were also excluded. ScTCR-seq/scBCR-seq data were first preprocessed by CellRanger v6.1.2 for V(D)J sequence assembly and TCR/BCR reconstruction using the human reference genome build 38. TCR annotation was performed using 10X CellRanger V(D)J pipeline as described. Only high-confidence and productive TRA/TRB annotations were used for further analysis. Cells sharing the same CDR3αβ nucleotide sequences were defined as belonging to the same TCR clone. For scBCR data, The Change-O repertoire clonal assignment toolkit was further applied to define clones. To calculate the SHM level of each BCR, BCR germline sequences were reconstructed using CreateGermlines.py and the number of somatic mutations for each sequence was calculated using observedMutations using Shazam software. Paired scTCR-seq/scBCR-seq data were integrated with scRNA-seq based on their matched unique cell barcodes.

Single-cell data normalization and clustering

Library size normalization was performed using the NormalizeData function in Seurat (v4.1.3) on the filtered gene-barcode matrices. The FindVariableFeatures of Seurat was applied to the normalized data to identify variable genes for unsupervised clustering. TCR/BCR variable genes were masked when performing clustering analysis. Principal component analysis was performed on the top 2,500 variable genes for dimension reduction and the Harmony algorithm was used for batch effect correction in the reduced dimension space of principal component analysis with default parameters. The function FindNeighbors of Seurat was used to construct the shared nearest neighbour graph, based on which function FindClusters of Seurat was used for unsupervised clustering. Different resolution parameters were examined to determine the optimal number of clusters. For visualization, dimensionality reduction and 2D visualization of the single cell clusters was performed using Uniform Manifold Approximation and Projection (UMAP) with the Seurat function RunUMAP. Multiple layers of information including the cluster distribution, cluster specific genes, canonical

immune cell markers and transcription factors were integrated and carefully reviewed to define cell subtypes.

Single-cell trajectory inference

To reconstruct the differentiation trajectory of TCRαβ$^+$ IEL cells, we applied Monocle 2 by inferring the pseudotemporal ordering of cells according to their transcriptome similarity. Monocle 2 was run with default parameters on the top 2,500 variable genes. To show the dynamics of tumour reactivity as pseudotime progresses, loess smoothed line of signature scores and *CD160* expression were plotted along the pseudotime axis. In addition, to provide a better visualization, Monocle 3 was applied to infer the differentiation states of PCs. To complement the trajectory analysis and better understand the cellular differentiation hierarchy of PCs, an independent approach CytoTRACE was then applied with default parameters to infer the cellular differentiation states using scRNA-seq data.

Bulk RNA-seq data analysis

To prepare data for downstream analysis, FastQC (v0.12.1) was used to assess the quality of raw sequencing data, and fastp software (v0.23.4) was applied to remove low-quality reads and any residual adaptor sequences. The high-quality reads were aligned to human genome reference GRCh38 (hg38) using the STAR algorithm (v2.7.10b). RSeQC (v5.0.3) was applied to assess the quality of alignment results using various alignment metrics, including coverage, mapping quality and distribution of mapped reads. Then, FeatureCount (v2.0.6) was utilized to extract the feature count matrix from alignments. We used edgeR (v3.40.2) for normalization and multidimensional scaling. We used the mSigDB database to investigate the overrepresentation of GO functions. The gene set enrichment score was estimated by single-sample GSEA (ssGSEA) using the GSVA R package (v1.44.5) before *z*-score normalization.

We downloaded the normalized RNA-seq data generated by TCGA on primary CRCs from NCI Cancer Genomic Data Commons (NCI-GDC: https://gdc.cancer.gov). The RNA-seq data were processed and normalized by the NCI-GDC bioinformatics team using their transcriptome analysis pipeline. The clinical annotation of the TCGA CRC cohort was downloaded from a recent PanCanAtlas study[65]. We downloaded two additional large-scale CRC datasets (GSE21510 and GSE39582) from the Gene Expression Omnibus (GEO) database. The raw data from microarray experiments were normalized using the Robust Multi-array Average algorithm. Within each microarray datasets, the most sensitive probe was used when multiple probes corresponding to the same gene. The immunotherapy dataset of CRC was obtained from GEO database (GSE235919) and the expression value measured by TPM was used.

Gene signature scoring

To characterize cells according to previously reported gene signatures of cytolytic activity, CD8$^+$ T cell exhaustion, *TCF7*$^+$ progenitor exhausted T cells, viral specificity and neoantigen specificity (Supplementary Table 2) gene scores were calculated per cell using the AUCell package (v1.18.1). After building a gene expression ranking for each cell, the gene set enrichment was calculated for each cell using the area under the recovery curve.

Clone-matched analysis

Clone-matched analysis of CD8$^+$ T cell clones was performed when at least one cell present in two matched tissues was found. Clonal scores and expressions were calculated per tissue by averaging the values of cells within each clone per each tissue. To characterize T cell state transitions of CD8$^+$ clones in TCRαβ$^+$ IELs, we only kept clones with at least one TCRαβ$^+$ IEL present in at least two tissues of ileum, colon and tumour. These included 36 matched clones across the all the tissues, 70 matched clones between ileum and colon, 14 matched clones across ileum and tumour and 24 matched clones across colon and tumour. To characterize T cell state transitions of CD8$^+$ clones that shared with tumoural IELs, we only kept CD8$^+$ clones of TCRαβ$^+$ IELs from tumour regions that shared with at least one cell with LNs or PBMCs. These included 24 matched clones across all the tissues, 60 matched clones between LNs and tumours and 11 matched clones between PBMCs and tumours. An unpaired Wilcoxon rank test was applied in clone-matched analysis due to the unequal number of matched clones within each tissue. To remove the potential false positive signature from cell debris, *CD160*$^+$ clones were defined by a minimum value 0.3 of the average expression of *CD160*.

Protein extraction and western blotting

Protein lysates were prepared immediately following cell collection to preserve protein integrity and minimize degradation. The detailed protocol is as follows: after collecting the cells, they were washed with PBS and lysed on ice for 30 min using RIPA (Beyotime) or NP40 (Beyotime) lysis buffer supplemented with protease and phosphatase inhibitors. The lysates were then centrifuged at 1,2000*g* for 15 min at 4 °C to remove cellular debris, yielding freshly prepared protein lysates. Protein concentrations were quantified using the BCA assay and normalized across samples. The lysates were diluted with XT Sample Buffer (Bio-Rad) and boiled for 10 min. All WB analyses were performed following SDS–PAGE using standard methods, and then transferred onto polyvinylidene difluoride membranes (Millipore). The membranes were incubated with the indicated primary antibodies overnight at 4 °C, followed by incubation with appropriate secondary antibodies for protein detection. Images were obtained using ChemiDoc MP Imaging System (Bio-Rad). Details of all antibodies used for western blot are provided in Supplementary Table 5.

Total RNA extraction and RT–qPCR

Total RNA was extracted from T cells using TRIzol reagent (Thermo Fisher). A total of 0.5 μg RNA was reverse transcribed into complementary DNA (cDNA) by the cDNA synthesis kit (Takara) according to the manufacturers' instructions. Subsequently, cDNA was performed to amplify on the CFX96 Real-Time System (Bio-Rad) using the SYBR RT–qPCR Master Mix (Roche). Finally, the mRNA expression was quantified using the $2^{-\Delta\Delta Ct}$ method. The relevant PCR primers used in this study are summarized in Supplementary Table 6.

Tissue digestion and flow cytometry analysis

Fresh tissues were dissected into 1 mm^3 fragments using scissors and then enzymatically digested with RPMI-1640 medium mixture supplemented with 1 mg ml^{-1} collagenase IV (Solarbio), and 0.1 mg ml^{-1} DNase (Solarbio) for 1 h using a constant temperature shaker (Spring Instrument Co. Ltd) at 37 °C. The dissociated cells from relative tissues were filtered through a 70 μm cell strainer (Biosharp) and collected by centrifugation at 600*g* for 20 min. Red blood cells were lysed with red blood cell lysis buffer (Miltenyi) on ice for 5 min. Single-cell suspensions were immediately stained with Zombine NIR (APC/CY7) followed by antibody staining. Cells were detected using a flow cytometer (BD FACSMelody), and corresponding experimental data were further analysed with FlowJo software V10. The representative figures of FACS gating strategy are included in Extended Data Fig. 10. Details of all antibodies used for flow cytometry are provided in Supplementary Table 5.

CD160$^+$CD8$^+$ and CD160$^-$CD8$^+$ T cells sorting and culture

As for sorting of primary CD160$^{+/-}$CD8$^+$ T cells, single-cell suspensions were prepared from mouse spleens, axillary draining lymph nodes or human PBMCs. CD160$^+$CD8$^+$ T cells and CD160$^-$CD8$^+$ T cells were then sorted from single-cell suspensions through a flow cytometer (BD FACSMelody) with anti-CD8α (PerCP-Cy5.5) and anti-CD160 (PE). The sorted CD160$^{+/-}$CD8$^+$ T cells were cultured for 3 days in RPMI-1640 complete medium (containing 1% penicillin/streptomycin and 10% FBS) with plate-bound anti-CD3 (10 μg ml^{-1}), soluble anti-CD28

(2 μg ml^{-1}) and recombinant murine IL-2 (20 ng ml^{-1}). Thereafter, cells were expanded for 7–14 days in fresh RPMI-1640 complete medium containing recombinant murine IL-2 (20 ng ml^{-1}), with medium replacement every 3 days. Before use, cells were restimulated with plate-bound anti-CD3 (10 μg ml^{-1}) and soluble anti-CD28 (2 μg ml^{-1}) to ensure they reached the required functional state.

T cell exhaustion assays in vitro

CD160$^-$CD8$^+$ and CD160$^+$CD8$^+$ T cells were sorted from spleens of normal C57BL/6 mice and initially activated with anti-CD3/CD28 antibodies for 2 days. Chronic stimulation was induced using plate-coated anti-CD3 (10 μg ml^{-1}) in RPMI-1640 medium containing 20 ng ml^{-1} murine IL-2 (PeproTech), 1% penicillin/streptomycin and 10% FBS. Cells were passaged onto a fresh coated plates every 2 days. On day 10, cells were collected for flow cytometry analysis of PD-1 and TIM3 expression.

T cell killing assays in vitro

CD160$^-$ and CD160$^+$CD8$^+$ T cells were sorted and expanded from the axillary draining lymph nodes of MC38-GFP tumour-bearing mice and MC38-GFP cells were sorted and expanded from the subcutaneous tumour tissues of the same MC38-GFP tumour-bearing mice by FACS. Then, 1×10^5 MC38-GFP cells were plated into a well of 6-well plate (Corning) for 24 h and then co-cultured with autologous CD160$^-$ or CD160$^+$CD8$^+$ T cells at a ratio of 1:10 for 48 h. GFP$^+$ MC38 tumour cells were stained with Zombie-NIR antibody and tumour cell death rate was determined by flow cytometry for the evaluation of T cell killing capacity.

Cell transduction and transfection

CD160$^-$CD8$^+$ and CD160$^+$CD8$^+$ T cells isolated and expanded from spleens of normal C57BL/6 mice were transduced with adenovirus supernatants encoding EGFP-tagged *Cd160*, *Tnfrsf9*, *Fcer1g* or controls, as well as lentiviral supernatants expressing shRNA targeting *Tnfrsf9*, *Fcer1g* or controls (Hanbio Biotechnology) using Polybrene (2 μg ml^{-1}) transfection reagent. HEK293T cells were seeded at 70% confluence and transfected with Flag-tagged PI3K p85α and p110δ plasmids alone or co-transfected with HA-tagged CD160 plasmid using jetPRIME transfection reagent (Polyplus) according to the manufacturer's instructions. CD160$^+$CD8$^+$ T cells were transfected with siRNA targeting PI3K p85α or p110δ (Sangon Biotech) using ProteanFect Max transfection reagent (Nanoportal Biotech) according to the manufacturer's instructions. In all constructs, the coding sequence for each protein (*Cd160*, *Tnfrsf9*, *Fcer1g*, *Pik3r1* and *Pik3cd*) and its respective tag (EGFP, FLAG and HA) are driven by separate promoters to prevent mutual interference. After transduced or transfection for 48 h, cells were collected for further experimental validation. The sequences of shRNA or siRNA used in the study are listed in Supplementary Table 7.

PLA

The interaction of CD160 and PI3K p85α was verified by PLA using a NaveniFlex Cell MR kit (Navinci) following the manufacturer's instructions. CD160$^+$CD8$^+$ T cells sorted and expanded from human PBMCs were fixed with 4% paraformaldehyde, permeabilized with 0.1% Triton X-100, followed by incubation with blocking buffer. Cells were incubated with primary antibodies CD160 and PI3K p85α, followed by secondary antibodies conjugated with PLA probes. After ligation and amplification, cells were stained with 4,6-diamidino-2-phenylindole (DAPI) (Beyotime) and imaged by confocal microscope.

Establishment and administration of anti-PD-1-resistant tumour models

Six-week-old male C57BL/6 mice were subcutaneously inoculated with MC38 cells. At 7 days after inoculation, mice received intraperitoneal injections of anti-PD-1 twice a week. After five injections, the largest tumour was selected and cut into approximately 1 mm^3 fragments, and transplanted subcutaneously into new 6-week-old male C57BL/6 mice. This process was repeated for seven generations until there was no significant change in tumour volume after anti-PD-1 treatment compared with IgG control, which confirmed the successful establishment of anti-PD-1 resistant tumour models.

In these experiments, CD160$^+$CD8$^+$ and CD160$^-$CD8$^+$ T cells were isolated and expanded from spleens of normal syngeneic C57BL/6 mice, cultured as described above and then adoptively transferred via tail vein injection after 7 days of transplantation of the P7 generation tumour fragments. Cells were administered weekly for a total of three treatments (1×10^6 cells per mouse). At the same time, anti-PD-1 antibody (100 μg per mouse) was intraperitoneally injected twice a week until the end of the experiment.

Statistics and reproducibility

Statistical analyses were performed as described in the figure legends. All basic statistical analysis were performed in R statistical environment (v4.2.1) and GraphPad Prism 9. All statistical tests performed in this study were two-sided. To control the false discovery rate (FDR) and correct *P* values for multiple testing, we applied the Benjamini–Hochberg method. To assess the prognostic value of the enrichment of mast cells, we first computed by obtaining the *z*-scores of the enrichment signature and then obtained a smooth estimate of the relationship between normalized signature and hazard ratio (smoothCoxph function in package phenoTest, v1.44.0). Samples were divided into three approximately equal groups by a signature score ±0.5, and Kaplan–Meier survival curves were compared between groups with high and low signature scores. For tumour experiments, mice were randomly assigned to different treatment groups. No data were excluded from the analyses. The investigators were not blinded to allocation during experiments and outcome assessment. Data distribution was assumed to be normal but this was not formally tested. Additionally, representative images of immunofluorescence and western blotting are from one experiment with at least three independent biological replicates.

Reporting summary

Further information on research design is available in the Nature Portfolio Reporting Summary linked to this article.

Data availability

All data needed to evaluate the conclusions in this study are present in the Article or its Supplementary Information. The raw sequence data reported in this Article have been deposited in the Genome Sequence Archive[66] in the National Genomics Data Center[67] via accession number HRA006401 for human scRNA/BCR/TCR-seq data, HRA006350 for human bulk RNA-seq data and CRA019585 for mouse bulk RNA-seq data. Processed scRNA/BCR/TCR-seq data and processed human bulk RNA-seq data are available are available via the Mendeley Data Repository at https://doi.org/10.17632/6czch25jyb.1 (ref. 68) and https://doi.org/10.17632/hb9jjk2gbz.1 (ref. 69). Processed mouse bulk RNA-seq data are available via the Mendeley Data repository at https://doi.org/10.17632/7tgb8gnb8f.1 (ref. 70). The processed public datasets were collected from different databases, including GEO (https://www.ncbi.nlm.nih.gov/geo/, GSE235919, GSE39582, GSE21510 and GSE205506), the GDC data portal (https://portal.gdc.cancer.gov/, TCGA-COAD and TCGA-READ) and the GTEx portal (https://www.gtexportal.org/). All other data supporting the findings of this study are available from the corresponding authors upon reasonable request. Source data are provided with this paper.

Code availability

Codes used for analysis and cell annotation are available via GitHub at https://github.com/HaoLabHMU/Colon-Adenocarcinoma.

References

61. Sui, Q. et al. Inflammation promotes resistance to immune checkpoint inhibitors in high microsatellite instability colorectal cancer. *Nat. Commun.* **13**, 7316 (2022).
62. Efremova, M. et al. Targeting immune checkpoints potentiates immunoediting and changes the dynamics of tumor evolution. *Nat. Commun.* **9**, 32 (2018).
63. Fong, W. et al. *Lactobacillus gallinarum*-derived metabolites boost anti-PD1 efficacy in colorectal cancer by inhibiting regulatory T cells through modulating IDO1/Kyn/AHR axis. *Gut* **72**, 2272–2285 (2023).
64. Castle, J. C. et al. Immunomic, genomic and transcriptomic characterization of CT26 colorectal carcinoma. *BMC Genomics* **15**, 190 (2014).
65. Liu, J. et al. An integrated TCGA pan-cancer clinical data resource to drive high-quality survival outcome analytics. *Cell* **173**, 400–416.e11 (2018).
66. Chen, T. et al. The genome sequence archive family: toward explosive data growth and diverse data types. *Genomics Proteomics Bioinformatics* **19**, 578–583 (2021).
67. CNCB-NGDC Members and Partners. Database resources of the National Genomics Data Center, China National Center for Bioinformation in 2024. *Nucleic Acids Res.* **52**, D18–D32 (2024).
68. Lyu, C. Single cell RNASeq data in colorectal cancer. *Mendeley Data, V1* https://doi.org/10.17632/6czch25jyb.1 (2025).
69. Lyu, C. Bulk RNASeq data in colorectal cancer. *Mendeley Data, V1* https://doi.org/10.17632/hb9jjk2gbz.1 (2025).
70. Lyu, C. Bulk RNASeq data from mouse spleens. *Mendeley Data, V1* https://doi.org/10.17632/7tgb8gnb8f.1 (2025).

Acknowledgements

This study was supported by The Tou-Yan Innovation Team Program of the Heilongjiang Province (grant 2019-15 to X.Z.). We thank H. Liang and Y. Luo of The University of Texas MD Anderson Cancer Center for their comments and suggestions on the paper. We thank P. Ding of Sun Yat-sen University Cancer Center for their assistance of partial biological samples in the study.

Author contributions

Conceptualization by T.Z., D.H. and X.Z. Methodology by D.H., C. Lyu., C.D. and X.L. Validation by C.D., S.L. and Y.G. Formal analysis by D.H., C. Lyu., B.S. and T.L. Data curation by L.C. Drafting and editing by T.Z., D.H., C.D., S.L. Y.G. and F.G. Investigation by C. Liu., J.S., Mingwei Li and Y.Z. Visualization by D.H., C. Lyu., S.L. and Y.G. Funding acquisition by X.Z. and T.Z. Resources from H.M., Mingqi Li, Y.L., S.T., L.L. and P.H. Supervision by T.Z., D.H. and X.Z. All authors revised and reviewed the paper and approved the final version.

Competing interests

The authors declare no competing interests.

Additional information

Extended data is available for this paper at https://doi.org/10.1038/s41556-025-01753-3.

Supplementary information The online version contains supplementary material available at https://doi.org/10.1038/s41556-025-01753-3.

Correspondence and requests for materials should be addressed to Tongsen Zheng, Dapeng Hao or Xue Zhang.

Peer review information *Nature Cell Biology* thanks Ping-Chih Ho, Dirk Jäger and the other, anonymous, reviewer(s) for their contribution to the peer review of this work. Peer reviewer reports are available.

Reprints and permissions information is available at www.nature.com/reprints.

https://doi.org/10.1038/s41556-025-01753-3

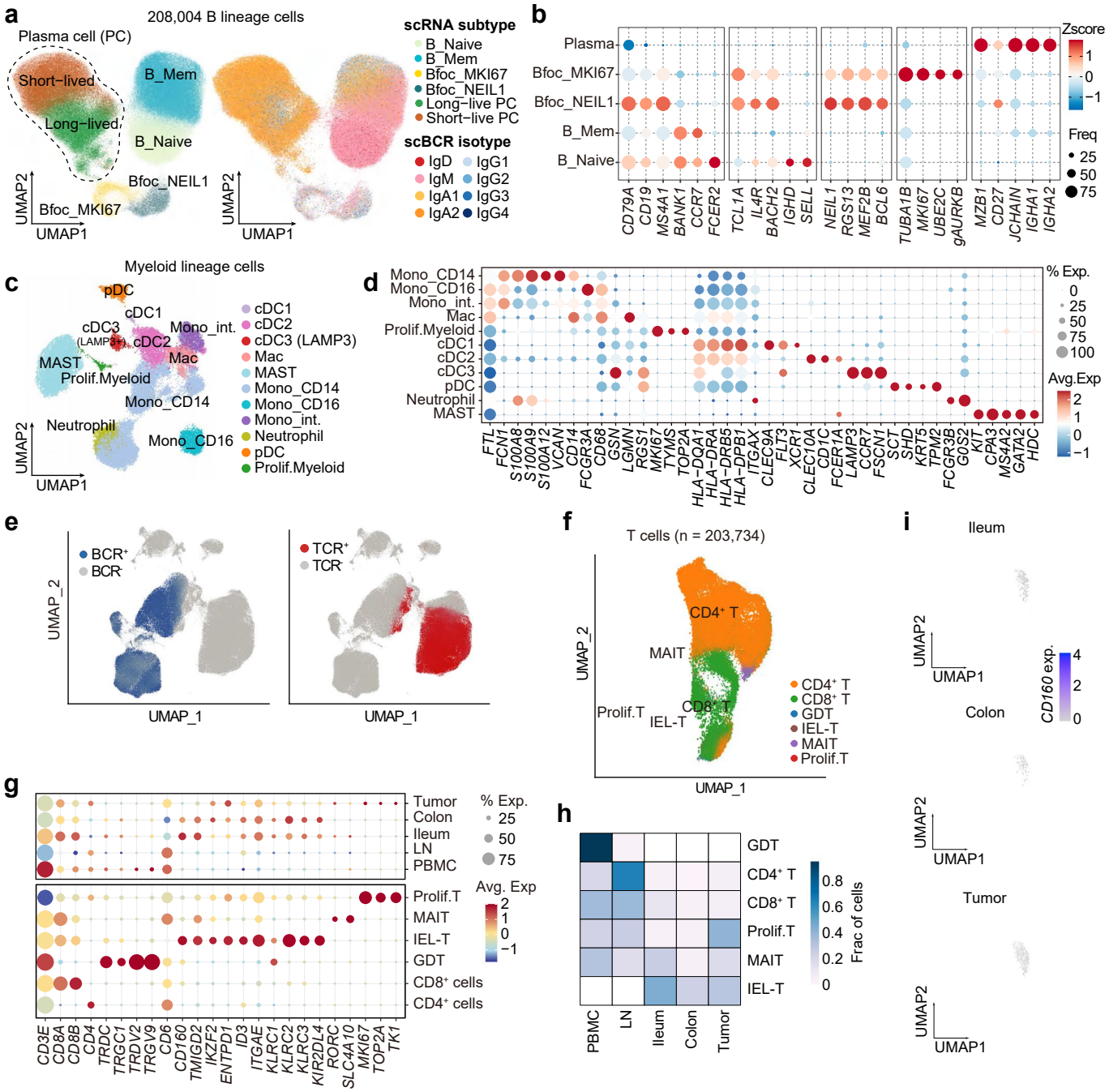

Extended Data Fig. 1 | Analysis of immune cells of CRC patients and healthy donors. a, UMAP plots showing 208,004 B lineage cells. Cells are color labeled with their inferred cell types/states based on transcriptional profiles (left) and antibody isotypes using scBCR-seq data (right). **b**, Bubble plots showing the expression of selected marker genes for B cells subtypes as defined in (**a**). Dot size indicates frequencies of expressing cells, colored according to average expression levels. **c**, UMAP plots showing subtypes of myeloid lineage cells. **d**, Bubble plot showing the expression of select marker genes for myeloid cells subtypes as defined in (**c**). Dot size indicates frequencies of expressing cells, colored according to average expression levels. **e**, The same UMAP as in Fig. 1b but with cells color coded by their BCR (left) and TCR (right) expression. **f**, UMAP plot showing all the T cells colored by 6 subtypes. **g**, Bubble plots showing average expression levels and proportions of select marker genes for different tissues (upper) and T cells subtypes as defined in (**f**) (bottom). Dot size indicates frequencies of expressing cells, colored according to normalized average expression levels. **h**, Heatmap displaying the fraction of T cells subtypes across multiple tissues. **i**, UMAP plots displaying the expression of *CD160* for T cells from ileum (upper), colon (middle) and tumor (bottom).

https://doi.org/10.1038/s41556-025-01753-3

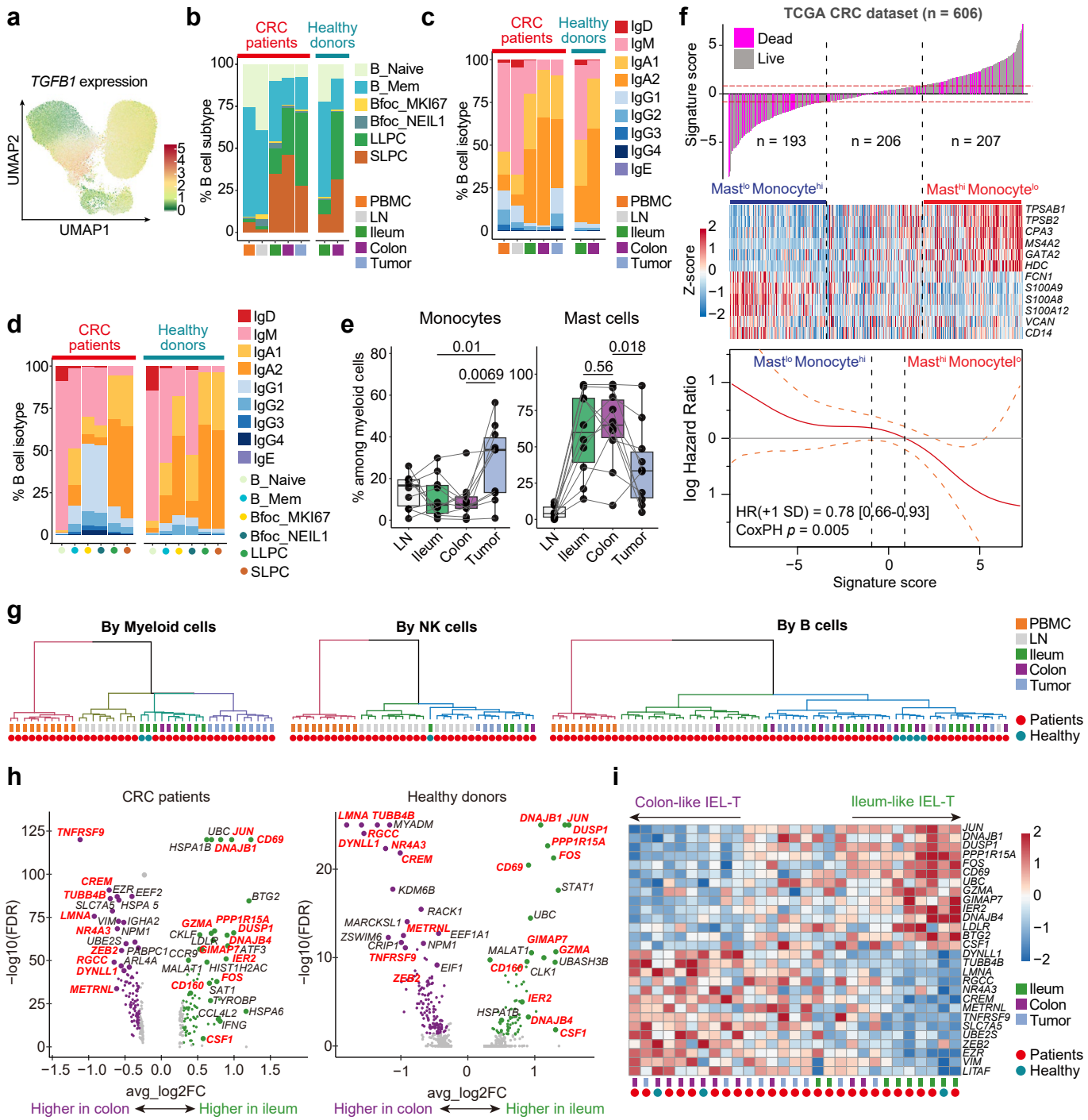

Extended Data Fig. 2 | Differences of the cellular composition, distribution and transcriptional states across different tissues. a, The same UMAP as in Extended Data Fig. 1a, but with cells colored by *TGFB1* expression. **b**–**d**, Bar graph displaying the composition of B cell subtypes (**b**) and antibody isotypes (**c**) across different tissues, and the landscape of antibody isotypes compositions across B cell subtypes (**d**) in CRC patients and healthy donors. **e**, Box plots showing the paired comparisons of cell proportions of monocyte and mast cells among matched tissues from the same CRC patients ($n = 10$). *P* values are determined by paired two-sided Mann-Whitney test. **f**, Patients from the TCGA CRC cohort that are ranked by signature score constructed using specific marker genes of mast cells and monocytes. Signature score is defined as the T-test score comparing normalized expression of mast cell markers versus monocyte markers. Samples are divided into 3 approximately equal groups according to the score (upper). The heatmap illustrating the expression of marker genes across tumor samples (middle). Estimates are made for the dependence of all-time risk of death on the signature score (bottom). *P* value is determined by the cox proportional hazards (CoxPH) model, and the dotted curves represent the 95% confidence interval (CI) of the log hazard ratio. Hi, high; lo, low. **g**, Unsupervised hierarchical clustering dendrogram of myeloid cells, NK cells and B cells derived from the average transcriptome profiles across tissues in CRC patients and healthy donors. **h**, Volcano plots illustrating the differentially expressed genes in IELs between colon and ileum of CRC patients (left) and healthy donors (right). Genes with significant differential expression and consistent tendency in CRC patients and healthy donors are indicated in green or purple dots and bold labels. **i**, Heatmap displaying expression of top DEGs of ileum vs. colon across ileum, colon and tumor in CRC patients and healthy donors. Box plots: center line, median; box limits, first and third quartile; whiskers, 1.5× interquartile range.

https://doi.org/10.1038/s41556-025-01753-3

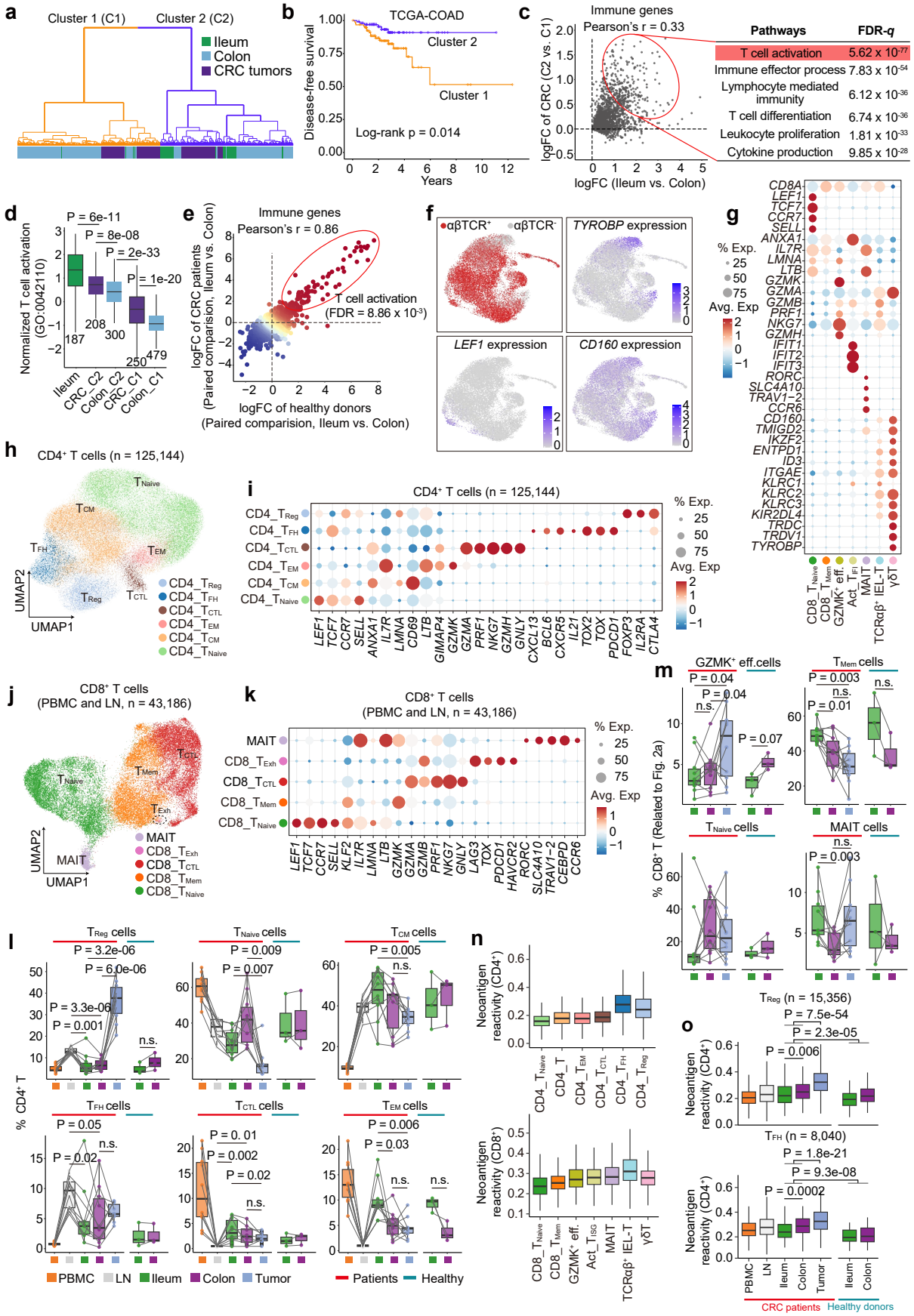

Extended Data Fig. 3 | See next page for caption.

https://doi.org/10.1038/s41556-025-01753-3

Extended Data Fig. 3 | Bulk RNA-seq analysis of transcriptional differences across different intestinal tissues and single-cell immune profiling of CD4$^+$ and CD8$^+$ T cells. a, Dendrogram showing unsupervised hierarchical clustering of tissue samples from CRC patients and healthy donors that were run on the expression of immune-related genes. **b**, Kaplan Meier curves displaying differences of DFS between the two clusters in TCGA-COAD cohort. **c**, Scatter plots showing immune genes expression fold change (log2) between C1 and C2 (y-axis) against the corresponding values of ileum and colon (x-axis). Dots in red circle represent top immune genes with significant expression change on both axes. Pathways enrichment of the selected immune genes and the most enriched pathways are labeled on the top. **d**, Box plots showing normalized T cell activation pathway enrichment score in different clusters across CRC tumors and normal tissues, ordered by decreasing signature score. The number of samples in each group is listed below the boxes. **e**, Scatter plot showing the correlation of differentially expressed immune related genes between ileum and colon in CRC patients (y-axis) against the corresponding values in healthy donors (x-axis). **f**, The same UMAP as in Fig. 2a but with cells colored by TCR productivity and gene expression of *TYROBP*, *LEF1*, *CD160*. **g**, Bubble plot showing the expression of indicated genes for CD8$^+$ T cells and IEL-T subtypes as defined in Fig. 2a. Dot size indicates frequencies of expressing cells, colored according to average expression levels. **h**, UMAP plot showing subtypes of CD4$^+$ T cells. **i**, Bubble plot showing the expression of select marker genes for CD4$^+$ T cells subtype as defined in (**h**). Dot size indicates frequencies of expressing cells, colored according to average expression levels. **j**, UMAP plot showing subtypes of CD8$^+$ T cells from PBMC and LN. **k**, Bubble plot showing the expression of select marker genes for CD8$^+$ T cells subtype from PBMC and LN. Dot size indicates frequencies of expressing cells, colored according to average expression levels. **l**, Box plots showing the paired comparisons of cell proportions of T_{Reg} cells, T_{Naive} cells, T_{CM} cells, T_{FH} cells, T_{CTL} cells and T_{EM} cells in CD4$^+$ T cells among matched tissues from the same CRC patients ($n = 10$) and healthy donors ($n = 3$). **m**, Box plots showing the paired comparisons of cell proportions of GZMK$^+$ eff. cells, T_{Mem} cells, T_{Naive} cells and MAIT cells in CD8$^+$ T cells among matched tissues from the same CRC patients ($n = 10$) and healthy donors ($n = 3$). **n**, Box plots showing neoantigen reactivity for CD4$^+$ (left) and CD8$^+$ (right) cells across the indicated cell subtypes. **o**, Box plots showing CD4$^+$ neoantigen reactivity of T_{Reg} and T_{FH} cells across the indicated tissue types in CRC patients and healthy donors. *P* values are determined by paired two-sided Mann-Whitney test (**d**, **l**, **m** and **o**). Box plots: center line, median; box limits, first and third quartile; whiskers, 1.5× interquartile range.

https://doi.org/10.1038/s41556-025-01753-3

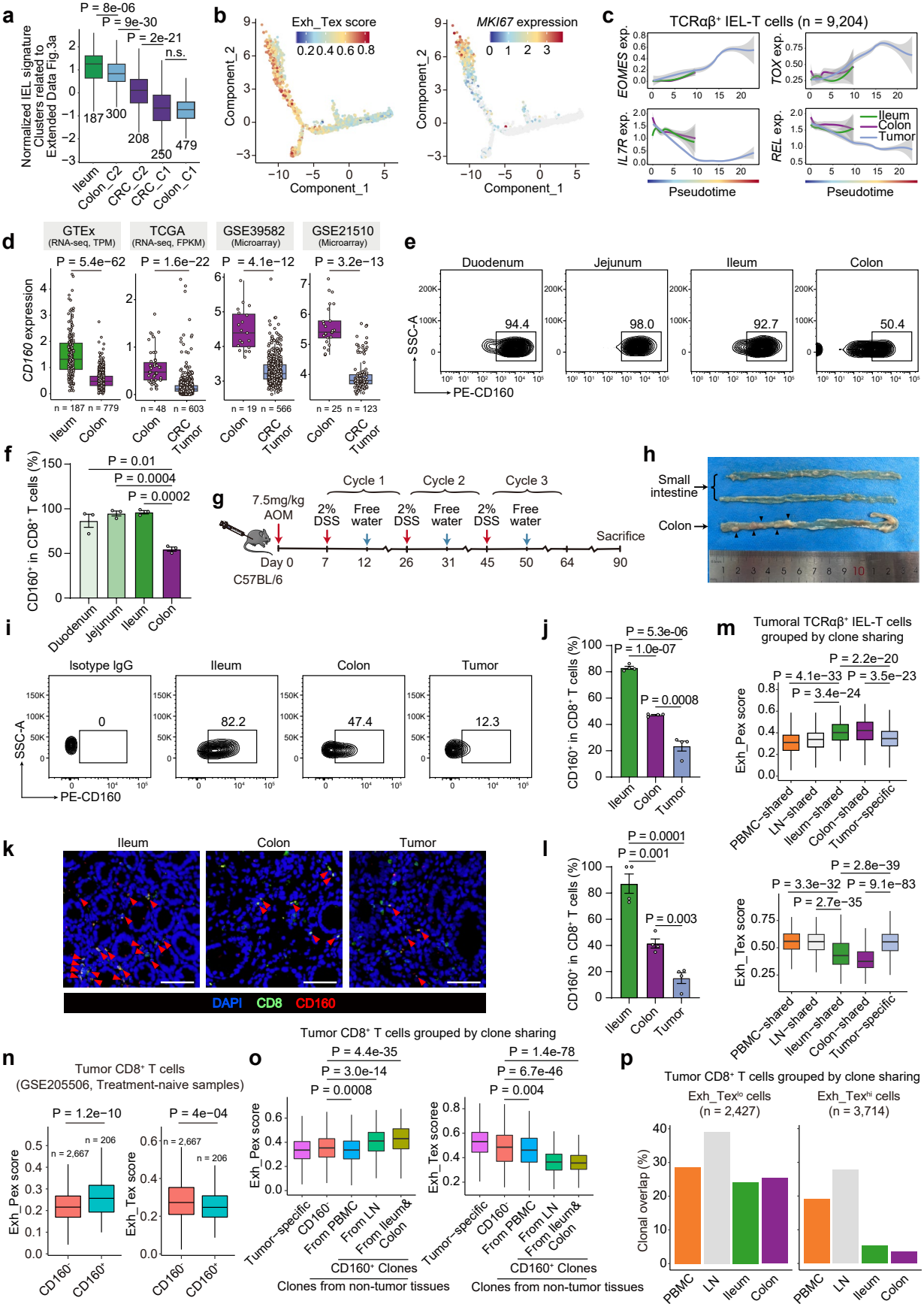

Extended Data Fig. 4 | See next page for caption.

https://doi.org/10.1038/s41556-025-01753-3

Extended Data Fig. 4 | Relationship between transition of T cell exhaustion state and CD160, and distribution of CD160$^+$CD8$^+$ T cells in different intestinal tissues. a, Box plots showing normalized IEL signature in different clusters, ordered by decreasing values. The number of samples in each group is listed below the boxes. **b**, Monocle trajectory plots of TCRαβ$^+$ IEL-T cells. Cells are colored by the Exh_Tex score (left) and *MKI67* expression (right). **c**, Monocle trajectory reconstruction of TCRαβ$^+$ IEL-T cells. Regression lines are fitted against pseudotime for *EOMES, IL7R, TOX, REL* expression of different tissue types. **d**, Box plots demonstrating the expression of *CD160* in ileum, colon and tumor tissues from GTEx, TCGA-CRC, GSE39582, and GSE21510 datasets. **e, f**, Representative flow cytometry plots (**e**) and frequencies (**f**) of CD160 in CD8$^+$ T cells among different intestinal tissues from C57BL/6 mice (n = 3 mice). **g**, Experimental scheme of AOM/DSS-induced CRC mouse model. **h**, Representative small intestine and colon images of AOM/DSS-induced CRC mouse (n = 6 mice). **i, j**, Representative flow cytometry plots (**i**) and frequencies (**j**) of CD160 in CD8$^+$ T cells among ileum, colon and tumor from AOM/DSS-induced CRC mice (n = 4 mice). **k, l**, Representative immunofluorescence staining (**k**) and quantification (**l**) of ileum, colon and tumor from AOM/DSS induced CRC mouse. Staining for CD8 (green), CD160 (red) and DAPI (blue). Red triangles highlight CD160$^+$CD8$^+$ T cells. Scale bars: 50 μm (n = 4 mice). **m**, Box plots showing the Exh_Pex score (left) and Exh_Tex score (right) of tumoral TCRαβ$^+$ IELs per indicated regional pattern. **n**, Box plots showing the Exh_Pex score (left) and Exh_Tex score (right) across *CD160*$^+$ and *CD160*$^-$ cells in tumoral CD8$^+$ T cells from GSE205506 dataset. **o**, Box plots showing the Exh_Pex score (left) and Exh_Tex score (right) of tumoral CD8$^+$ T cells per indicated regional pattern. **p**, Bar plots showing the fraction of tumoral CD8$^+$ T cells that are clonally linked with cells from other indicated tissues. Cells are divided by the cutoff 0.45 of Exh_Tex score, and only cells from clones containing at least 2 tumoral CD8$^+$ T cells are included. *P* values are determined by paired two-sided Mann-Whitney test (**a**, **d**, **m**, **n** and **o**). Data are shown as the mean ± s.e.m, *P* values were determined by unpaired two-tailed Student's t-test (**f**, **j**, and **l**). Box plots: center line, median; box limits, first and third quartile; whiskers, 1.5× interquartile range.

https://doi.org/10.1038/s41556-025-01753-3

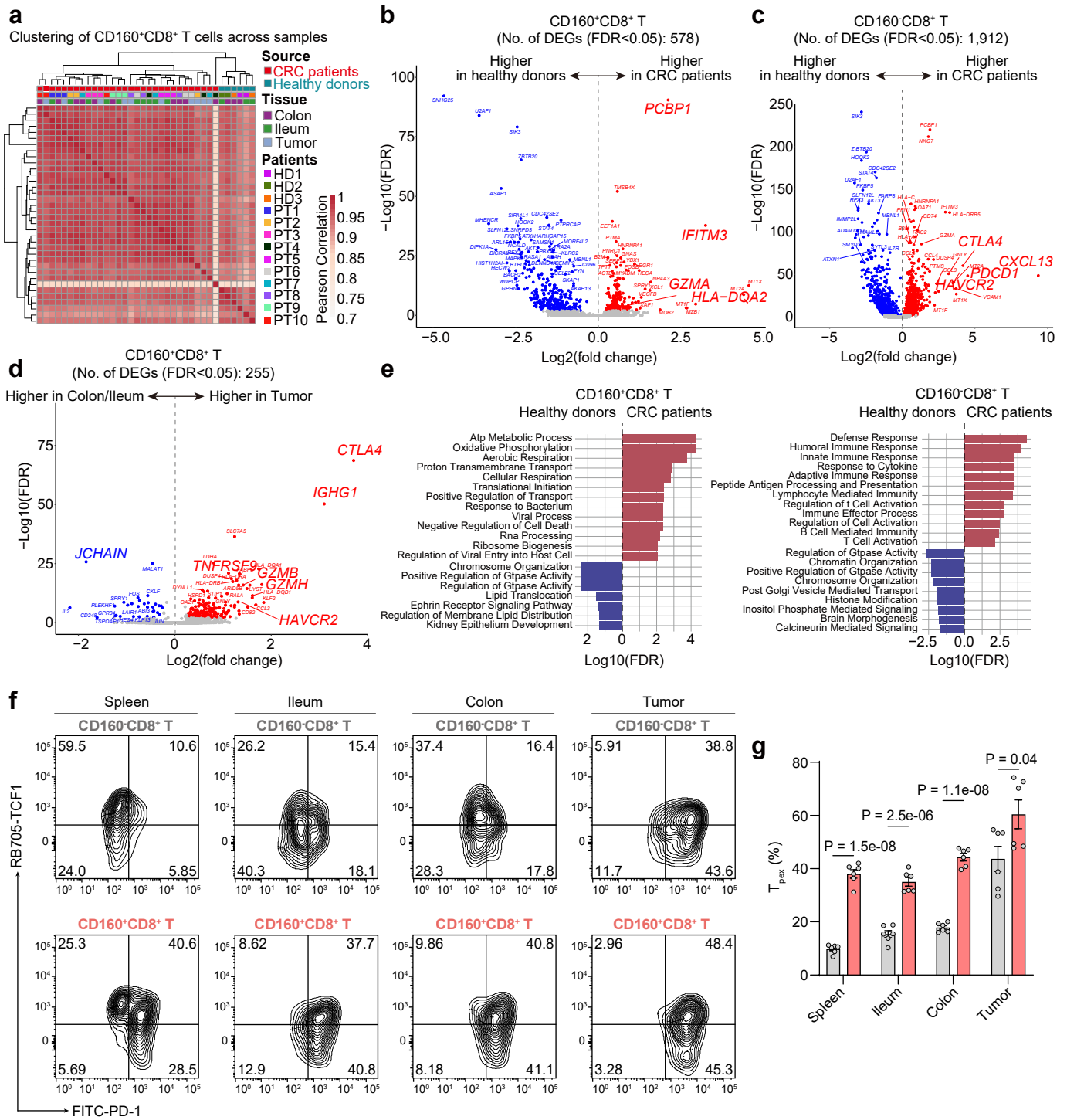

Extended Data Fig. 5 | Conserved transcriptomes and progenitor exhausted phenotype of CD160$^+$CD8$^+$ T cells across tissues. a, Clustering and correlation of CD160$^+$CD8$^+$ T cells across samples indicate higher variation across individuals than across tissues. Clustering is based on Euclidean distances between the average transcriptome of samples. **b-d**, Volcano plots illustrating DEGs in CD160$^+$CD8$^+$ T cells (**b**) and CD160$^-$CD8$^+$ T cells (**c**) between healthy donors and CRC patients, and CD160$^+$CD8$^+$ T cells (**d**) between tumor and normal tissues from CRC patients. Contamination signals are highlighted due to subtle transcriptomic differences in (**d**), as shown by the top DEGs such as *JCHAIN* and *IGHG1*. **e**, GSEA of GO biological processes in CD160$^+$ and CD160$^-$ CD8$^+$ T cells between healthy donors and CRC patients that indicates the enrichment of metabolism- and immune-related pathways, respectively. **f, g**, Representative flow cytometry plots (**f**) and frequencies (**g**) of TCF1$^+$PD-1$^+$ in CD160$^+$CD8$^+$ and CD160$^-$CD8$^+$ T cells from indicated tissues of MC38 tumor-bearing mice ($n = 6$ mice). Data are shown as the mean ± s.e.m, P values were determined by unpaired two-tailed Student's t-test (**g**).

https://doi.org/10.1038/s41556-025-01753-3

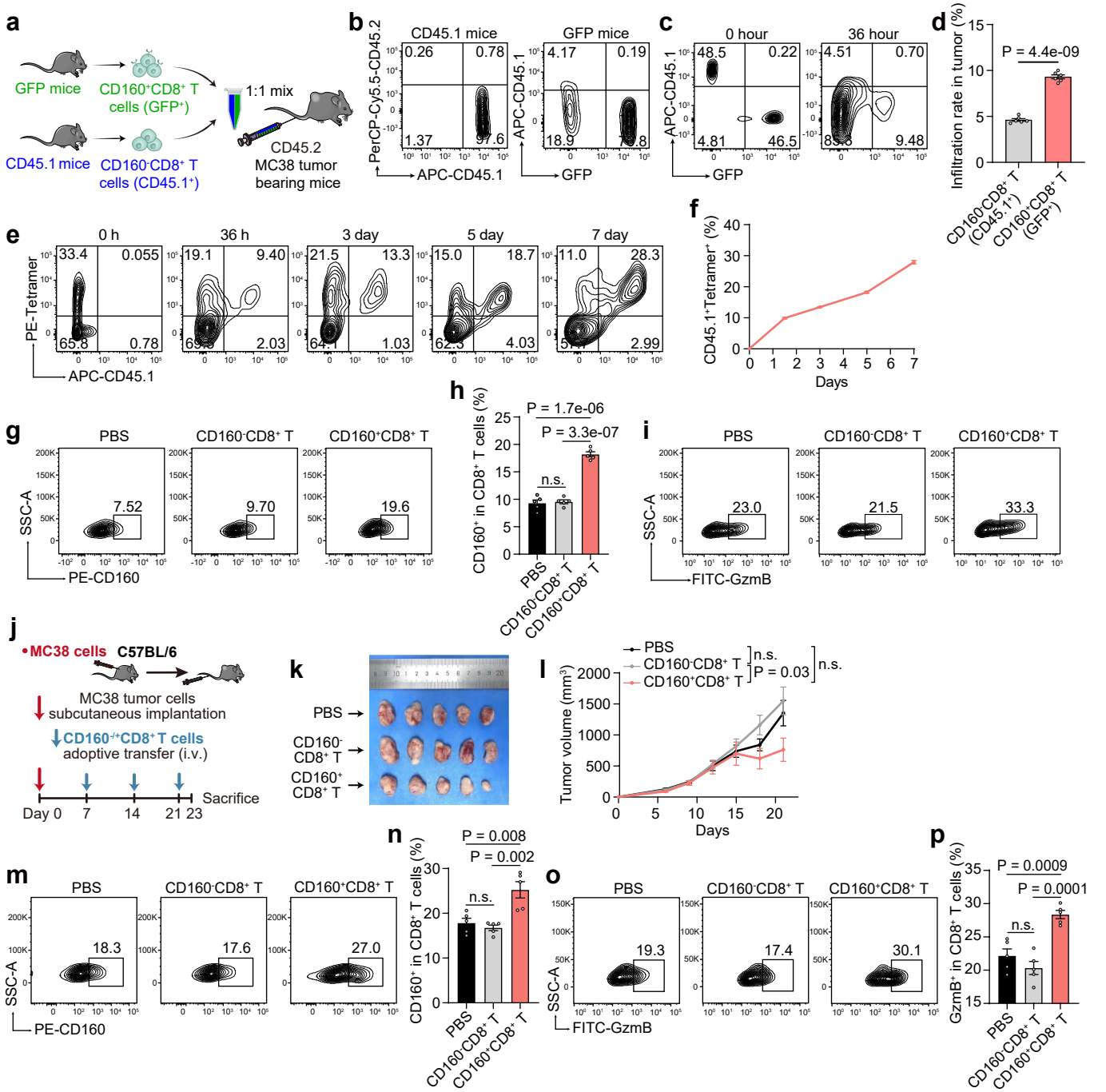

Extended Data Fig. 6 | Adoptive transfer of CD160$^+$CD8$^+$ T cells inhibit the growth of MC38 subcutaneous tumor. a, Schematic representation of co-transfer of CD160$^+$CD8$^+$ T cells (GFP$^+$) and CD160$^-$CD8$^+$ T cells (CD45.1$^+$) into MC38 tumor-bearing mice. **b**, Representative flow cytometry identification plots of splenocytes from CD45.1 and GFP mice. **c, d**, Representative flow cytometry plots (**c**) and frequencies (**d**) of GFP$^+$CD45.1$^-$ and GFP$^-$CD45.1$^+$ in tumors 36 hours after transfer ($n = 6$ mice). **e, f**, Representative flow cytometry plots (**e**) and frequencies (**f**) of CD45.1$^+$Tetramer$^+$ cells in tumors at indicated timepoints after adoptive transfer CD160$^+$CD8$^+$ T cells from CD45.1 mouse spleens into established MC38-OVA tumors ($n = 5$ mice). **g, h**, Representative flow cytometry plots (**g**) and frequencies (**h**) of CD160 in CD8$^+$ T cells isolated from tumor tissues, as shown in Fig. 4m ($n = 5$ mice). **i**, Representative flow cytometry plots of GzmB in CD8$^+$ T cells isolated from tumor tissues, as shown in Fig. 4m. **j**, Experimental scheme for adoptive T cell transfer in established MC38 tumors. Splenic CD160$^+$CD8$^+$ and CD160$^-$CD8$^+$ T cells from normal syngeneic C57BL/6 mice were transferred via tail vein injection at the indicated time points. **k, l**, Representative tumor images (**k**) and tumor volume (**l**) in MC38 tumor mouse model, as shown in (**j**) ($n = 5$ mice). **m, n**, Representative flow cytometry plots (**m**) and frequencies (**n**) of CD160 in CD8$^+$ T cells isolated from tumor tissues, as shown in (**j**) ($n = 5$ mice). **o, p**, Representative flow cytometry plots (**o**) and frequencies (**p**) of GzmB in CD8$^+$ T cells isolated from tumor tissues in MC38 tumor-bearing mice, as shown in (**j**) ($n = 5$ mice). Data are shown as the mean ± s.e.m, *P* values were determined by unpaired two-tailed Student's t-test (**d**, **h**, **l**, **n** and **p**).

https://doi.org/10.1038/s41556-025-01753-3

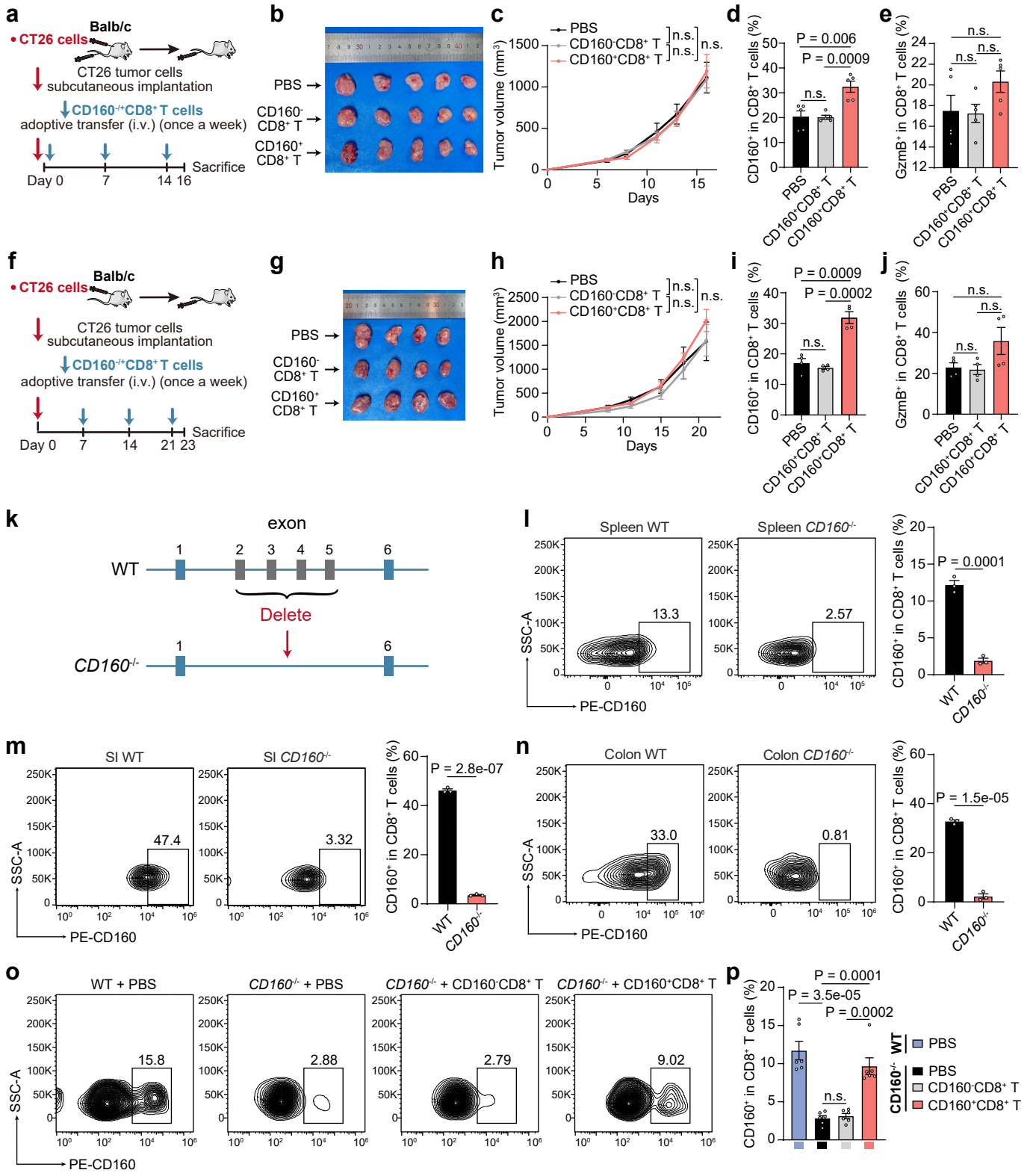

Extended Data Fig. 7 | See next page for caption.

https://doi.org/10.1038/s41556-025-01753-3

Extended Data Fig. 7 | Effects of CD160 expression levels on CD8$^+$ T cell anti-tumor function in MSS CRC model and validation of CD160 knockout efficiency of *Cd160*$^{-/-}$ mice. a, Experimental scheme for adoptive T cell transfer while inoculating the CT26 cell line into Balb/c mice. Splenic CD160$^+$CD8$^+$ and CD160$^-$CD8$^+$ T cells from normal syngeneic Balb/c mice were transferred via tail vein injection at the indicated time points. **b, c**, Representative tumor images (**b**) and tumor volume (**c**) in CT26 tumor-bearing mice, as shown in (**a**) ($n = 5$ mice). **d, F**requencies of CD160 in CD8$^+$ T cells isolated from tumor tissues in CT26 tumor-bearing mice, as shown in (**a**) ($n = 5$ mice). **e**, Frequencies of GzmB in CD8$^+$ T cells isolated from tumor tissues in CT26 tumor-bearing mice, as shown in (**a**) ($n = 5$ mice). **f**, Experimental scheme for adoptive T cell transfer in established CT26 tumors. Splenic CD160$^+$CD8$^+$ and CD160$^-$CD8$^+$ T cells from normal syngeneic Balb/c mice were transferred via tail vein injection at the indicated time points. **g, h**, Representative tumor images (**g**) and tumor volume (**h**) in CT26 tumor-bearing mice, as shown in (**f**) ($n = 4$ mice). **i**, Frequencies of CD160 in CD8$^+$ T cells isolated from tumor tissues in CT26 tumor-bearing mice, as shown in (**f**) ($n = 4$ mice). **j**, Frequencies of GzmB in CD8$^+$ T cells isolated from tumor tissues in CT26 tumor-bearing mice, as shown in (**f**) ($n = 4$ mice). **k**, Scheme of generation of *Cd160*$^{-/-}$ mice. **l**–**n**, Representative flow cytometry plots and frequencies of CD160 in CD8$^+$ T cells isolated from spleen (**l**), small intestine (**m**) and colon (**n**) in WT and *Cd160*$^{-/-}$ mice. **o, p**, Representative flow cytometry plots (**o**) and frequencies (**p**) of CD160 in CD8$^+$ T cells isolated from tumor tissues in WT and *Cd160*$^{-/-}$ mice bearing MC38 tumor, as shown in Fig. 5e ($n = 6$ mice). Data are shown as the mean ± s.e.m, *P* values were determined by unpaired two-tailed Student's t-test (**c**, **d**, **e**, **h**, **i**, **j**, **l, m, n** and **p**).

https://doi.org/10.1038/s41556-025-01753-3

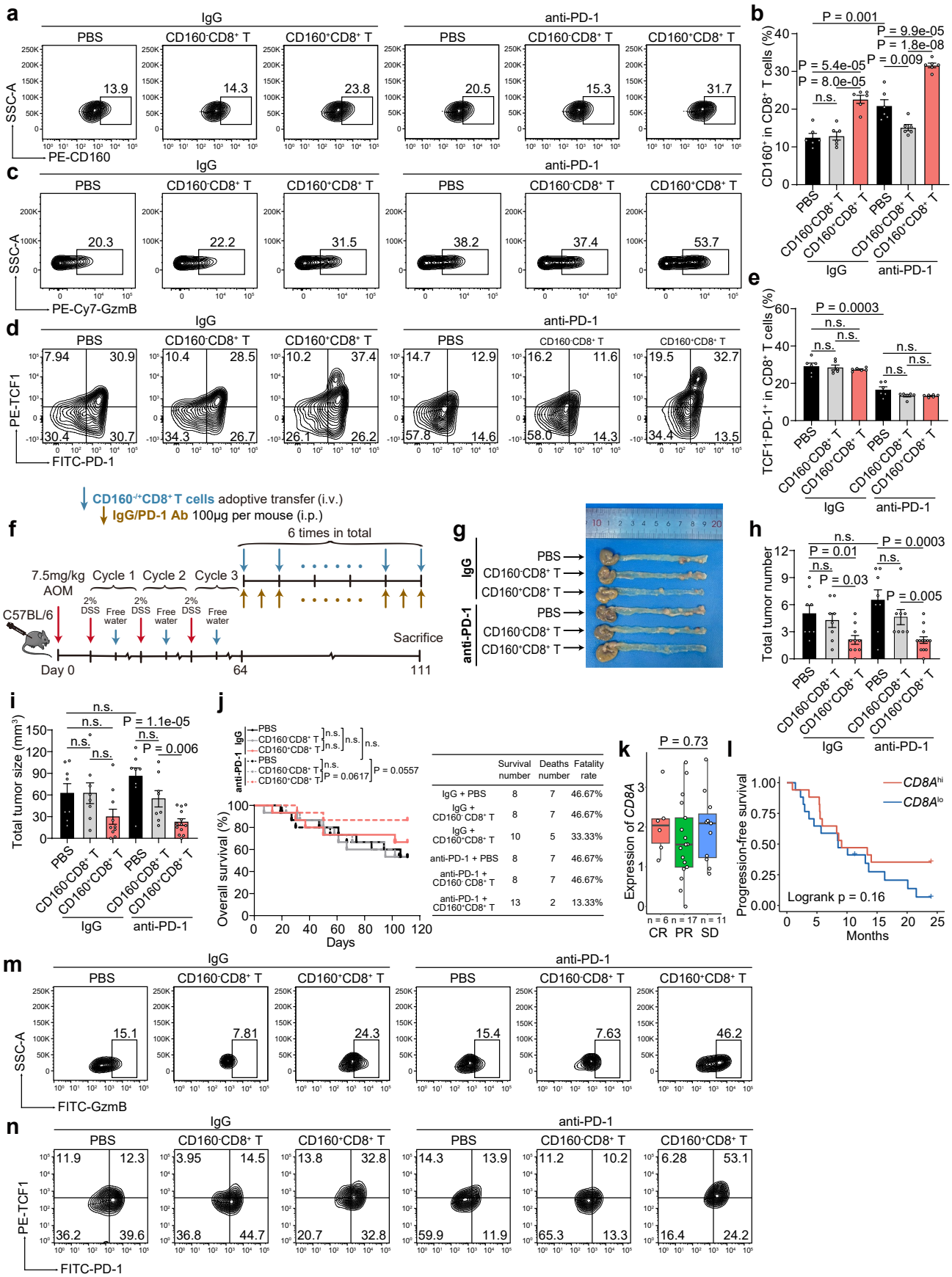

Extended Data Fig. 8 | See next page for caption.

https://doi.org/10.1038/s41556-025-01753-3

Extended Data Fig. 8 | Adoptive transfer of CD160$^+$CD8$^+$ T cells combined with anti-PD-1 therapy inhibits CRC progression and overcomes anti-PD-1 resistance. a, b, Representative flow cytometry plots (**a**) and frequencies (**b**) of CD160 in CD8$^+$ T cells isolated from tumor tissues in MC38 tumor-bearing mice, as shown in Fig. 6a ($n = 6$ mice). **c**, Representative flow cytometry plots of GzmB in CD8$^+$ T cells isolated from tumor tissues in MC38 tumor-bearing mice, as shown in Fig. 6a. **d, e**, Representative flow cytometry plots (**d**) and frequencies (**e**) of TCF1$^-$PD-1$^+$ in CD8$^+$ T cells isolated from tumor tissues in MC38 tumor-bearing mice, as shown in Fig. 6a ($n = 6$ mice). **f**, Experimental scheme for adoptive T cell transfer combined with anti-PD-1 therapy in AOM/DSS-induced CRC mice. Splenic CD160$^{-/+}$CD8$^+$ T cells from normal syngeneic C57BL/6 mice were adoptively transferred via tail vein injection, while AOM/DSS-induced CRC mice were administrated anti-PD-1 at the indicated time points. **g**, Representative images of colon tumors in AOM/DSS-induced CRC mice, as shown in (**f**) ($n = 8$–13 mice). **h-j** Total tumor number (**h**) and tumor size (**i**) in colon tissues and survival curve (**j**) were calculated under the indicated treatments, as shown in (**f**) ($n = 8$–13 mice). **k**, Box plots showing *CD8A* expression across different response groups of CRC patients received first line immunotherapy (CR $n = 6$; PR $n = 17$; SD $n = 11$). *P* values are determined by paired two-sided Mann-Whitney test. **l**, Kaplan–Meier curves displaying differences in PFS between CRC patients grouped by the high or low expression of *CD8A*. *P* value is determined by long-rank test. **m**, Representative flow cytometry plots of GzmB in CD8$^+$ T cells isolated from tumor tissues in anti-PD-1 resistant model mice, as shown in Fig. 6m ($n = 6$ mice). **n**, Representative flow cytometry plots of TCF1$^+$PD-1$^+$ in CD8$^+$ T cells isolated from tumor tissues in anti-PD-1 resistant model mice, as shown in Fig. 6m ($n = 6$ mice). Data are shown as the mean ± s.e.m, *P* values were determined by unpaired two-tailed Student's t-test (**b**, **e**, **h**, **i** and **j**). Box plots: center line, median; box limits, first and third quartile; whiskers, 1.5× interquartile range.

https://doi.org/10.1038/s41556-025-01753-3

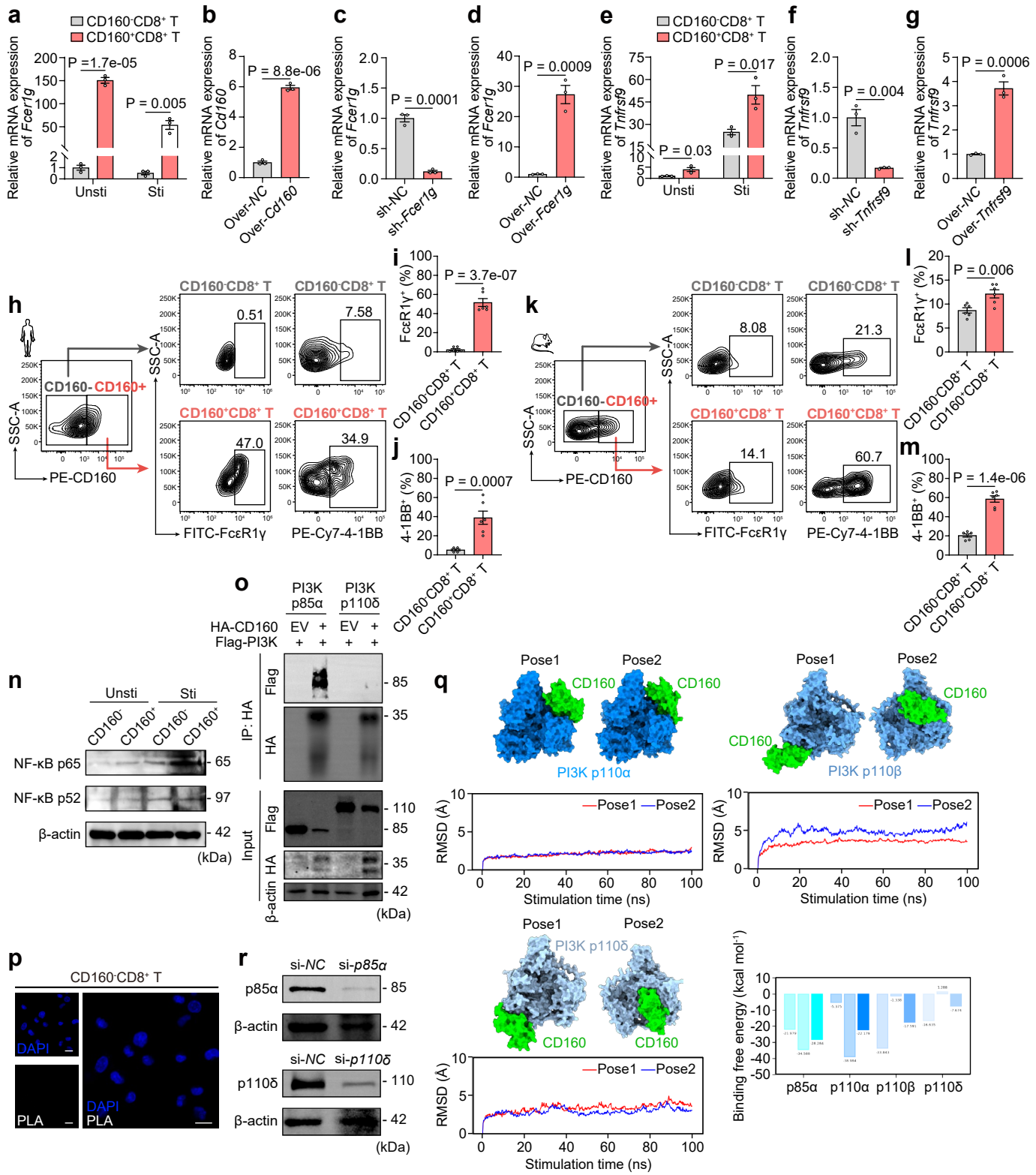

Extended Data Fig. 9 | See next page for caption.

https://doi.org/10.1038/s41556-025-01753-3

Extended Data Fig. 9 | CD160 regulates *Fcer1g* and *Tnfrsf9* expression to affect the cytotoxic function of CD8$^+$ T cells. a, Relative mRNA expression of *Fcer1g* in CD160$^{-/+}$CD8$^+$ T cells with or without anti-CD3/CD28 stimulation for 24 hours ($n = 3$ biological replicates). **b**, Relative mRNA expression of *Cd160* in CD160$^-$CD8$^+$ T cells overexpressing *Cd160* ($n = 3$ biological replicates). **c**, Relative mRNA expression of *Fcer1g* in CD160$^+$CD8$^+$ T cells after knocking down *Fcer1g* ($n = 3$ biological replicates). **d**, Relative mRNA expression of *Fcer1g* in CD160$^-$CD8$^+$ T cells overexpressing *Fcer1g* ($n = 3$ biological replicates). **e**, Relative mRNA expression of *Tnfrsf9* in CD160$^{-/+}$CD8$^+$ T cells with or without anti-CD3/CD28 stimulation for 24 hours ($n = 3$ biological replicates). **f**, Relative mRNA expression of *Tnfrsf9* in CD160$^+$CD8$^+$ T cells after knocking down *Tnfrsf9* ($n = 3$ biological replicates). **g**, Relative mRNA expression of *Tnfrsf9* in CD160$^-$CD8$^+$ T cells overexpressing *Tnfrsf9* ($n = 3$ biological replicates). **h**–**j**, Representative flow cytometry plots (**h**) and frequencies of FcεR1γ$^+$ (**i**) and 4-1BB$^+$ (**j**) cells in CD160$^+$ versus CD160$^-$ CD8$^+$ T cells isolated from tumor tissues of CRC patients ($n = 6$ samples). **k**–**m**, Representative flow cytometry plots (**k**) and frequencies of FcεR1γ$^+$ (**l**) and 4-1BB$^+$ (**m**) cells in tumor-infiltrating CD160$^+$ versus CD160$^-$ CD8$^+$ T cells from MC38 tumor-bearing mice ($n = 6$ mice). **n**, Representative images of NF-κB p65 and NF-κB p52 protein expression in CD160$^{-/+}$CD8$^+$ T cells with or without anti-CD3/CD28 stimulation for 24 hours analysed by Western blot. **o**, Binding of HA-tagged CD160 to the Flag-tagged PI3K p85α and p110δ in HEK293T cells. **p**, PLA signals between PI3K and CD160 in CD160$^-$CD8$^+$ T cells. Scale bars: 10 μm. **q**, Predicted binding models, stability, and binding free energy of CD160 interactions with p110α, p110β, p110δ. **r**, Knockdown efficiency of p85α and p110δ siRNA was verified in CD160$^+$CD8$^+$ T cells. Data are shown as the mean ± s.e.m, *P* values were determined by unpaired two-tailed Student's t-test (**a**, **b**, **c**, **d**, **e**, **f**, **g**, **i**, **j**, **l** and **m**).

https://doi.org/10.1038/s41556-025-01753-3

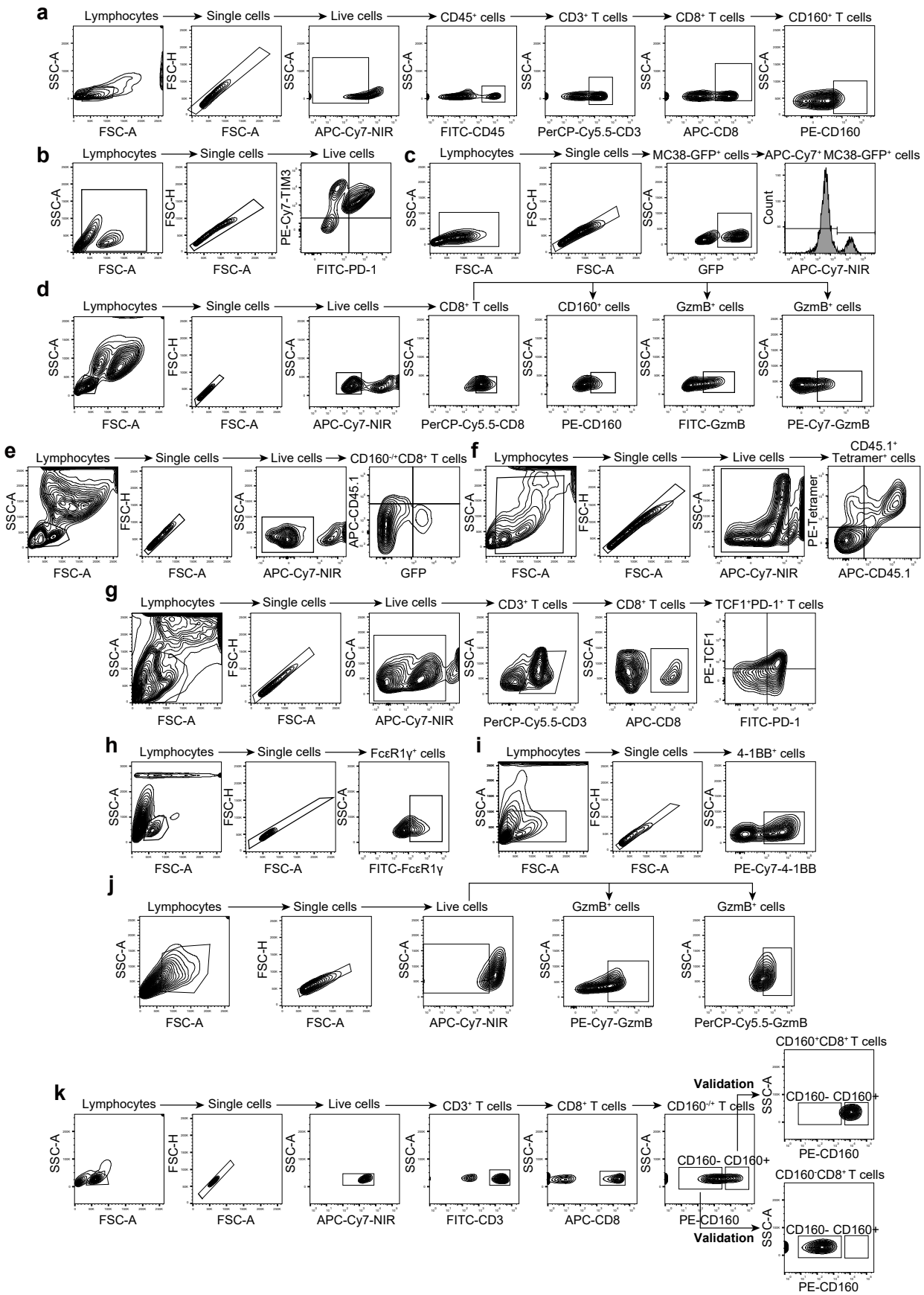

Extended Data Fig. 10 | See next page for caption.

https://doi.org/10.1038/s41556-025-01753-3

Extended Data Fig. 10 | Representative gating strategies for T lymphocytes. **a**, FACS gating strategy of $CD160^+$ in $CD8^+$ T cells isolated from intestine and spleen. Related to Fig. 2k; Extended Data Fig. 4e, i; Extended Data Fig. 7l, m, n. **b**, FACS gating strategy for *in vitro* exhaustion assay. Related to Fig. 4d. c, FACS gating strategy for co-culture system. Related to Fig. 4g. **d**, FACS gating strategy of $CD160^+$ and $GzmB^+$ cells in tumor-infiltrating $CD8^+$ T cells. Related to Fig. 5h; Extended Data Fig. 6g, i, m, o; Extended Data Fig. 7o; Extended Data Fig. 8a, c, m; Extended Data Fig. 9h, k. **e**, FACS gating strategy of $CD160^+CD8^+$ T cells ($GFP^+CD45.1^-$) and $CD160^-CD8^+$ T cells ($GFP^-CD45.1^+$) int tumor. Related to Extended Data Fig. 6c. **f**, FACS gating strategy of $CD45.1^+Tetramer^+$ cells in tumor. Related to Extended Data Fig. 6e. **g**, FACS gating strategy of progenitor exhausted $CD8^+$ T cells in tumor. Related to Fig. 5l; Extended Data Fig. 8d, n. **h**, FACS gating strategy of $Fc\varepsilon R1\gamma^+$ in $CD160^-CD8^+$ T cells or $CD160^+CD8^+$ T cells. Related to Fig. 7e. **i**, FACS gating strategy of 4-$1BB^+$ in $CD160^-CD8^+$ T cells or $CD160^+CD8^+$ T cells. Related to Fig. 7i. **j**, FACS gating strategy of $GzmB^+$ in $CD160^-CD8^+$ T cells or $CD160^+CD8^+$ T cells. Related to Fig. 4a; Fig. 7f, g, j, k. **k**, FACS sorting strategy of $CD160^+CD8^+$ T cells from spleen and purity validation.

nature portfolio

Corresponding author(s): Xue Zhang, Dapeng Hao, Tongsen Zheng

Last updated by author(s): Jul 16, 2025

Reporting Summary

Nature Portfolio wishes to improve the reproducibility of the work that we publish. This form provides structure for consistency and transparency in reporting. For further information on Nature Portfolio policies, see our Editorial Policies and the Editorial Policy Checklist.

Statistics

For all statistical analyses, confirm that the following items are present in the figure legend, table legend, main text, or Methods section.

n/a	Confirmed
☐	☒ The exact sample size (*n*) for each experimental group/condition, given as a discrete number and unit of measurement
☐	☒ A statement on whether measurements were taken from distinct samples or whether the same sample was measured repeatedly
☐	☒ The statistical test(s) used AND whether they are one- or two-sided *Only common tests should be described solely by name; describe more complex techniques in the Methods section.*
☒	☐ A description of all covariates tested
☒	☐ A description of any assumptions or corrections, such as tests of normality and adjustment for multiple comparisons
☐	☒ A full description of the statistical parameters including central tendency (e.g. means) or other basic estimates (e.g. regression coefficient) AND variation (e.g. standard deviation) or associated estimates of uncertainty (e.g. confidence intervals)
☐	☒ For null hypothesis testing, the test statistic (e.g. *F*, *t*, *r*) with confidence intervals, effect sizes, degrees of freedom and *P* value noted *Give P values as exact values whenever suitable.*
☒	☐ For Bayesian analysis, information on the choice of priors and Markov chain Monte Carlo settings
☒	☐ For hierarchical and complex designs, identification of the appropriate level for tests and full reporting of outcomes
☐	☒ Estimates of effect sizes (e.g. Cohen's *d*, Pearson's *r*), indicating how they were calculated

Our web collection on statistics for biologists contains articles on many of the points above.

Software and code

Policy information about availability of computer code

Data collection	Please see Methods section for data collection details. The library was sequenced on the Illumina NovaSeq 6000 sequencer with 150 bp paired-end reads. Flow cytometry data were collected by BD FACSMelody. Immunofluorescence images were acquired by fluorescence microscope (OLYMPUS, BX53F2). Images of multiplex immunohistochemistry were acquired using TissueFAXS Spectra Systems (TissueGnostics).

Data analysis	Please see Methods section for data analysis details. GraphPad Prism version 9 FlowJo software (v10.8.1) CellRanger (v6.1.2) FastQC (v0.12.1) Fastp (v0.23.4) STAR (v2.7.10b) RseQC (v5.0.3) FeatureCount (v2.0.6) DoubletFinder (v2.0.3) Seurat (v4.1.3) EdgeR (v3.40.2) GSVA R package (v1.44.5) Sva R package (v3.46.0) PhenoTest (v1.44.0)

For manuscripts utilizing custom algorithms or software that are central to the research but not yet described in published literature, software must be made available to editors and reviewers. We strongly encourage code deposition in a community repository (e.g. GitHub). See the Nature Portfolio guidelines for submitting code & software for further information.

Data

Policy information about availability of data

All manuscripts must include a data availability statement. This statement should provide the following information, where applicable:

- Accession codes, unique identifiers, or web links for publicly available datasets
- A description of any restrictions on data availability
- For clinical datasets or third party data, please ensure that the statement adheres to our policy

All data needed to evaluate the conclusions in the paper are present in the paper or the Supplementary Materials. The raw sequence data reported in this paper have been deposited in the Genome Sequence Archive in National Genomics Data Center via accession number HRA006401 for human scRNA/BCR/TCR-seq data, HRA006350 for human bulk RNA-seq data and CRA019585 for mouse bulk RNA-seq data. Processed scRNA/BCR/TCR-seq data and processed human bulk RNA-seq data are available are available from the Mendeley Data Repository (https://doi.org/10.17632/6czch25jyb.1 and https://doi.org/10.17632/hb9jjk2gbz.1). Processed mouse bulk RNA-seq data is available in the Mendeley Data repository (https://doi.org/10.17632/7tgb8gnb8f.1). The processed public datasets were collected from different databases, including Gene Expression Omnibus (GEO, https://www.ncbi.nlm.nih.gov/geo/, GSE235919, GSE39582, GSE21510 and GSE205506), GDC data portal (https://portal.gdc.cancer.gov/, TCGA-COAD and TCGA-READ) and GTEx portal (https://www.gtexportal.org/). All other data supporting the findings of this study are available from the corresponding authors upon reasonable request.

Research involving human participants, their data, or biological material

Policy information about studies with human participants or human data. See also policy information about sex, gender (identity/presentation), and sexual orientation and race, ethnicity and racism.

Reporting on sex and gender	In Supplementary Table 1, we obtained 19 patients with a pathological diagnosis of adenocarcinoma, ranging in age from 42 to 73 years. 8 were female and 11 were male. Meanwhile, we obtained 7 healthy donors with age between 41 and 53. All of them were male. In supplementary table 4, we obtained 13 MSI-H CRC patients with a pathological diagnosis of adenocarcinoma, ranging in age from 30 and 70. 3 were female and 10 were male.
Reporting on race, ethnicity, or other socially relevant groupings	All of the enrolled patients were Chinese.
Population characteristics	The clinical characteristic of patients involved in the study were showed in Supplementary Table 1 and 4.
Recruitment	1. Nineteen patients with primary colon cancer who underwent right hemicolectomy and pathologically diagnosed with colon adenocarcinoma at Harbin Medical University Cancer Hospital were enrolled. 2. Eight healthy donors were enrolled from The First Affiliated Hospital of Harbin Medical University, The Second Affiliated Hospital of Harbin Medical University and The First Affiliated Hospital of USTC. 3. Thirteen patients genetically diagnosed MSI-H and histologically confirmed colon cancer at Sun Yat-sen University Cancer Center were enrolled. There is no self-selection bias or other biases in recruitment.
Ethics oversight	The clinical protocol and samples were approved by the IRB at Harbin Medical University (IRB reference: HMUIRB2023001). All human participants signed informed consent before sample collection, in compliance with the Declaration of Hlesinki.

Note that full information on the approval of the study protocol must also be provided in the manuscript.

Field-specific reporting

Please select the one below that is the best fit for your research. If you are not sure, read the appropriate sections before making your selection.

☒ Life sciences ☐ Behavioural & social sciences ☐ Ecological, evolutionary & environmental sciences

For a reference copy of the document with all sections, see nature.com/documents/nr-reporting-summary-flat.pdf

Life sciences study design

All studies must disclose on these points even when the disclosure is negative.

Sample size	For scRNA/TCR/BCR-seq and bulk RNA-seq experiments, no statistical methods were used to predetermine the sample size. As many patients as possible were included in the study. For all other studies, our sample sizes are similar to those reported in previous publication (PMID: 38683582).
Data exclusions	No data was excluded.
Replication	Most sequencing was performed once per human sample because of the limited amount of tissue that is available per patients and healthy donors. For in vivo and in vitro animal experiments, we had three replicates, and the results were quite consistent between replicates.
Randomization	For in vivo experiments, all mice were randomly allocated into experimental groups. For cell experiments, randomization was not required because cells were manipulated in various ways and all samples were analyzed equally.
Blinding	Blinding was applied to all sequencing data generated in this study, where technical staff were not provided with sample identifying information. For all other experiments, the investigators were not blinded to allocation during experiments, outcome assessment and analysis. As we collected all effective experimental results. Blinding was not performed during allocation as mice were randomly assigned to groups with strict controls. In cell experiments, blinding is impractical due to varied manipulation based on design. During the data collection, our experimental data were relatively objective, so the lack of blinding had little impact on the results.

Reporting for specific materials, systems and methods

We require information from authors about some types of materials, experimental systems and methods used in many studies. Here, indicate whether each material, system or method listed is relevant to your study. If you are not sure if a list item applies to your research, read the appropriate section before selecting a response.

Materials & experimental systems

n/a	Involved in the study
☐	☒ Antibodies
☐	☒ Eukaryotic cell lines
☒	☐ Palaeontology and archaeology
☐	☒ Animals and other organisms
☒	☐ Clinical data
☒	☐ Dual use research of concern
☒	☐ Plants

Methods

n/a	Involved in the study
☒	☐ ChIP-seq
☐	☒ Flow cytometry
☒	☐ MRI-based neuroimaging

Antibodies

Antibodies used

Antibodies for Immunofluorescence:
Rabbit anti-Human CD8α (Cell Signaling Technology, Cat: #85336S, Lot 5, 1:100)
Rat anti-mouse CD8α (R&D Systems, Cat: #MAB116, Lot FSG0523022, 15μg/mL)
Sheep anti-mouse CD160 (R&D Systems, Cat: #AF3899, Lot CFFK0424021, 15μg/mL)
NF-kappaB p65 (D14E12) XP (R) Rabbit mAb (Cell Signaling Technology, Cat: #8242, Lot 16, 1:400)
Rabbit anti Sheep IgG (H&L)-Texas Red (Immunoway Biotechnology, Cat: #RS2730, Lot B3001, 1:200)
Goat Anti-Rat IgG H&L (Alexa Fluor® 488) (Abcam, Cat: #ab150157, Lot 1003916-7, 1:200)
Goat Anti-Rabbit IgG H&L (Alexa Fluor® 488) (Abcam, Cat: #ab150080, Lot 1043748-9, 1:200)
Antibodies for Western blot:
Anti-CD160 antibody (Affinity, Cat: #DF3522, Lot 56g9168, 1:1000)
PI3 Kinase p85 alpha+p55 antibody (Abcam, Cat: #ab278545, Lot 1037346-2, 1:1000)
PI3 Kinase p85 antibody (Cell Signaling Technology, Cat: #4257, Lot 7, 1:1000)
Phospho-Akt Rabbit mAb (Cell Signaling Technology, Cat: #4060, Lot 27, 1:2000)
AKT antibody (Cell Signaling Technology, Cat: #9272, Lot 30, 1:1000)
NF-kappaB2 p100/p52 Rabbit Ab (Cell Signaling Technology, Cat: #4882, Lot 7, 1:1000)
NF-kappaB p65 (D14E12) XP (R) Rabbit mAb (Cell Signaling Technology, Cat: #8242, Lot 27, 1:1000)
Histone H3 Polyclonal antibody (Proteintech, Cat: #17168-1-AP, Lot 00172674, 1:2000)
β-actin Monoclonal antibody (Proteintech, Cat: #66009-1-Ig, Lot 100254559, 1:20000)

4-1BB/CD137/TNFRSF9 (E2J5H) XP® Rabbit mAb (Cell Signaling Technology, Cat: #18798, Lot 1, 1:1000)
FCER1G Antibody (Affinity, Cat: #DF13263, Lot 9d2340, 1:1000)
DYKDDDDK Tag (D6W5B) Rabbit mAb (Cell Signaling Technology, Cat: #14793, Lot 7, 1:1000)
Antibodies for Co-Immunoprecipitation:
PI3 Kinase p85α (6G10) Mouse mAb (Cell Signaling Technology, Cat: #13666, Lot 2, 1:50)
PI3 Kinase p110α (C73F8) Rabbit mAb (Cell Signaling Technology, Cat: #4249, Lot 12, 1:50)
PI3 Kinase p110β Polyclonal antibody (Proteintech, Cat: #20584-1-AP, Lot 00164450, 4μg)
PI3 Kinase p110δ (D1Q7R) Rabbit mAb (Cell Signaling Technology, Cat: #34050, Lot 3, 1:50)
PI3 Kinase p110γ (D55D5) Rabbit mAb (Cell Signaling Technology, Cat: #5405, Lot 6, 1:50)
HA-Tag (C29F4) Rabbit mAb (Cell Signaling Technology, Cat: #3724, Lot 13, 1:50)
Antibodies for PLA:
Anti-CD160 antibody (Affinity, Cat: #DF3522, Lot 56g9168, 1:100)
PI3 Kinase p85-alpha (6G10) Mouse mAb (Cell Signaling Technology, Cat: #13666, Lot2, 1:100)
Antibodies for Flow Cytometry:
Anti-human CD45-PerCP antibody (BioLegend, Cat: #368507, Clone no.2D1, Lot B435873, 1:100)
Anti-human CD3-FITC antibody (BioLegend, Cat: #317335, Clone no. OKT3, Lot B441277, 1:100)
Anti-human CD8α-APC antibody (BioLegend, Cat: #301014, Clone no. RPA-T8, Lot B386144, 1:100)
Anti-human CD160-PE antibody (BioLegend, Cat: #341206, Clone no.BY55, Lot B400429, 1:100)
Anti-human 4-1BB-PE-CY7 antibodies (BioLegend, Cat: #309818, Clone no. 4B4-1, Lot B350445, 1:100)
Anti-mouse CD45-FITC antibody (BioLegend, Cat: #10310, Clone no.30-F11, Lot B388747, 1:100)
Anti-mouse CD3 Percp-Cy5.5 antibody (BioLegend, Cat: # 100218, Clone no. 145-2C11, Lot B384141, 1:100)
Anti-mouse CD8 Percp-Cy5.5 antibody (BioLegend, Cat: #100734, Clone no. 53-6.7, Lot B434030, 1:100)
Anti-mouse CD8α-APC antibody (BioLegend, Cat: #100712, Clone no. 53-6.7, Lot B420169, 1:100)
Anti-mouse CD4-PE-CY7 antibody (BioLegend, Cat: # 100422, Clone no. GK1.5, Lot B384460, 1:100)
Anti-mouse CD160-PE antibody (BioLegend, Cat: #143004, Clone no.7H1, Lot B409225, 1:100)
PE/Cyanine7 anti-human/mouse Granzyme B Recombinant (BioLegend, Cat: #372214, Clone no. QA16A02, Lot B419880, 1:100)
Anti-human/mouse Granzyme B-FITC antibody (BioLegend, Cat: #515403, Clone no. GB11, Lot B378948, 1:100)
Anti-mouse Granzyme B-PerCP-Cy5.5 antibody (BioLegend, Cat: #372211, Clone no. QA16A02, Lot B419880, 1:100)
Anti-mouse PD-1-FITC antibody (BioLegend, Cat: #135213, Clone no. 29F.1A12, Lot B427394, 1:100)
Anti-mouse TCF1/TCF7-RB705 antibody (BD Pharmingen, Cat: #570635, Clone no. S33-966, Lot 4275880, 1:100)
Anti-TCF1/TCF7-PE antibody (Cell Signaling Technology, Cat: #14456S, Clone no. C63D9, Lot 10, 1:200)
Anti-mouse CD366 (TIM3)-PE-CY7 antibody (BioLegend, Cat: #134010, Clone no. B8.2C12, Lot B410824, 1:100)
Anti-Mouse CD137 (4-1BB)-PE-CY7 antibody (Thermo Fisher, Cat: #25-1371-82, Clone no.17B5, Lot 2704649, 1:100)
Anti-Fcer1g-FITC antibody (Sigma, Cat: #FCABS400F, Lot 4193481, 1:200)
PE Rat IgG2a, κ Isotype Ctrl Antibody (BioLegend, Cat: #400507, Clone no. RTK2758, Lot B413062, 1:100)
PE Mouse IgM, κ Isotype Ctrl Antibody (BioLegend, Cat# 401611, Clone no. MM-30, Lot B389534, 1:100)
TruStain FcX™ (anti-mouse CD16/32) Antibody (BioLegend, Cat: #101319, Clone no. 93, Lot B431985, 1:200)
Anti-mouse CD45.1-APC antibody (BioLegend, Cat: #110714, Clone no. A20, Lot B436731, 1:100)
Anti-mouse CD45.2-PerCP-Cy5.5 antibody (BioLegend, Cat: #109827, Clone no. 104, Lot B432283, 1:100)
T-Select H-2Kb OVA Tetramer-SIINFEKL-PE (MBL Life Science, Cat# TS-5001-1C, Lot C003, 1:50)
Antibodies for Multiplex immunohistochemistry:
CD8α (D4W2Z) XP® Rabbit mAb (Cell Signaling Technology, Cat: #98941, Lot 6, 1:200)
PD-1 (D7D5W) XP® Rabbit mAb (Cell Signaling Technology, Cat: #84651, Lot 4, 1:100)
TCF1/TCF7 (C63D9) Rabbit mAb (Cell Signaling Technology, Cat: #2203, Lot 11, 1:100)
Rabbit anti-mouse TIM3 (Abcam, Cat: # ab241332, Lot 1038545-26, 1:1000)
Antibodies for Immunohistochemistry:
Granzyme B Antibody (2C5) (Santa Cruz Biotechnology, Cat: #sc-8022, Lot E0719, 1:200)
Antibody for in vivo experiment:
InVivoMAb Rat IgG2α isotype control (BioXcell, Cat: #BE0089, Clone no. 2A3, Lot 919324J3B, 100μg)
InVivoMAb anti-Mouse PD-1 (CD279) (BioXcell, Cat: #BE0146, Clone no. RMP1-14, Lot 865024J1, 100μg)
Antibodies for T cell activation:
anti-mouse CD3 Antibody (BioLegend, Cat: #100340, Clone no. 145-2C11, Lot B411255, 10mg/mL)
anti-mouse CD28 Antibody (BioLegend, Cat: #102116, Clone no. 37.51, Lot B436439, 2mg/mL)

Validation

The commercial antibodies employed in this study underwent rigorous validation procedures by their respective manufacturers. The antibodies were applied in accordance with the provided manutacturers' recommendations on the official websites. Only when manufacturer validation was doubtful, antibodies were tested on positive controls and/or positive controls.
Rabbit anti-Human CD8α (Cell Signaling Technology, Cat: #85336S, https://www.cellsignal.cn/products/primary-antibodies/cd8a-d8a8y-rabbit-mab/85336)
Rat anti-mouse CD8α (R&D Systems, Cat: #MAB116, https://www.rndsystems.com/cn/products/mouse-cd8alpha-antibody-53-67_mab116?keywords=MAB116)
Sheep anti-mouse CD160 (R&D Systems, Cat: #AF3899, https://www.rndsystems.com/cn/products/mouse-cd160-antibody_af3899)
NF-kappaB p65 (D14E12) XP (R) Rabbit mAb (Cell Signaling Technology, Cat: #8242, https://www.cellsignal.cn/products/primary-antibodies/nf-kb-p65-d14e12-xp-rabbit-mab/8242)
Rabbit anti Sheep IgG (H&L)-Texas Red (Immunoway Biotechnology, Cat: #RS2730, https://www.immunoway.com/products/secondary-antibodies/RS2730-Rabbit-anti-Sheep-IgG-H-L-Texas-Red.html)
Goat Anti-Rat IgG H&L (Alexa Fluor® 488) (Abcam, Cat: #ab150157, https://www.abcam.cn/products/secondary-antibodies/goat-rat-igg-hl-alexa-fluor-488-ab150157.html)
Goat Anti-Rabbit IgG H&L (Alexa Fluor® 488) (Abcam, Cat: #ab150080, https://www.abcam.cn/products/secondary-antibodies/goat-rabbit-igg-hl-alexa-fluor-594-ab150080.html)
Antibodies for Western blot:
Anti-CD160 antibody (Affinity, Cat: #DF3522, https://www.affbiotech.com/goods-2512-DF3522-CD160_Antibody.html)
PI3 Kinase p85 alpha+p55 antibody (Abcam, Cat: #ab278545, https://www.abcam.cn/products/primary-antibodies/-pi-3-kinase-p85-alpha-phospho-y467--pi3-kinase-p55-phospho-y199-antibody-pi3ky458-1a11-ab278545.html)
PI3 Kinase p85 antibody (Cell Signaling Technology, Cat: #4257, https://www.cellsignal.cn/products/primary-antibodies/pi3-kinase-

p85-19h8-rabbit-mab/4257)
Phospho-Akt Rabbit mAb (Cell Signaling Technology, Cat: #4060, https://www.cellsignal.cn/products/primary-antibodies/phospho-akt-ser473-d9e-xp-rabbit-mab/4060)
AKT antibody (Cell Signaling Technology, Cat: #9272, https://www.cellsignal.cn/products/primary-antibodies/akt-antibody/9272)
NF-kappaB2 p100/p52 Rabbit Ab (Cell Signaling Technology, Cat: #4882, https://www.cellsignal.cn/products/primary-antibodies/nf-kb2-p100-p52-antibody/4882)
NF-kappaB p65 (D14E12) XP (R) Rabbit mAb (Cell Signaling Technology, Cat: #8242, https://www.cellsignal.cn/products/primary-antibodies/nf-kb-p65-d14e12-xp-rabbit-mab/8242)
Histone H3 Polyclonal antibody (Proteintech, Cat: #17168-1-AP, https://www.ptgcn.com/products/Histone-H3-Antibody-17168-1-AP.htm)
β-actin Monoclonal antibody (Proteintech, Cat: #66009-1-Ig, https://www.ptgcn.com/products/Pan-Actin-Antibody-66009-1-Ig.htm)
4-1BB/CD137/TNFRSF9 (E2J5H) XP® Rabbit mAb (Cell Signaling Technology, Cat: #18798, https://www.cellsignal.cn/products/primary-antibodies/4-1bb-cd137-tnfrsf9-e2j5h-xp-rabbit-mab/18798)
FCER1G Antibody (Affinity, Cat: #DF13263, https://www.affbiotech.com/goods-16641-DF13263-FCER1G_Antibody.html)
DYKDDDDK Tag (D6W5B) Rabbit mAb (Cell Signaling Technology, Cat: #14793, https://www.cellsignal.cn/products/primary-antibodies/dykddddk-tag-d6w5b-rabbit-mab-binds-to-same-epitope-as-sigma-aldrich-anti-flag-m2-antibody/14793)
PI3 Kinase p85α (6G10) Mouse mAb (Cell Signaling Technology, Cat: #13666, https://www.cellsignal.cn/products/primary-antibodies/pi3-kinase-p85a-6g10-mouse-mab/13666)
PI3 Kinase p110α (C73F8) Rabbit mAb (Cell Signaling Technology, Cat: #4249, https://www.cellsignal.cn/products/primary-antibodies/pi3-kinase-p110a-c73f8-rabbit-mab/4249)
PI3 Kinase p110β Polyclonal antibody (Proteintech, Cat: #20584-1-AP, https://www.ptgcn.com/products/PIK3CB-Antibody-20584-1-AP.htm)
PI3 Kinase p110δ (D1Q7R) Rabbit mAb (Cell Signaling Technology, Cat: #34050, https://www.cellsignal.cn/products/primary-antibodies/pi3-kinase-p110-d-d1q7r-rabbit-mab/34050)
PI3 Kinase p110γ (D55D5) Rabbit mAb (Cell Signaling Technology, Cat: #5405, https://www.cellsignal.cn/products/primary-antibodies/pi3-kinase-p110g-d55d5-rabbit-mab/5405)
HA-Tag (C29F4) Rabbit mAb (Cell Signaling Technology, Cat: #3724, https://www.cellsignal.cn/products/primary-antibodies/ha-tag-c29f4-rabbit-mab/3724)
Anti-CD160 antibody (Affinity, Cat: #DF3522, https://www.affbiotech.com/goods-2512-DF3522-CD160_Antibody.html)
PI3 Kinase p85-alpha (6G10) Mouse mAb (Cell Signaling Technology, Cat: #13666, https://www.cellsignal.cn/products/primary-antibodies/pi3-kinase-p85a-6g10-mouse-mab/13666)
Anti-human CD45-PerCP antibody (BioLegend, Cat: #368507, https://www.biolegend.com/en-us/products/fitc-anti-human-cd45-antibody-12394)
Anti-human CD3-FITC antibody (BioLegend, Cat: #317335, https://www.biolegend.com/en-us/products/percp-cyanine5-5-anti-human-cd3-antibody-8220)
Anti-human CD8α-APC antibody (BioLegend, Cat: #301014, https://www.biolegend.com/en-us/products/apc-anti-human-cd8a-antibody-831)
Anti-human CD160-PE antibody (BioLegend, Cat: #341206, https://www.biolegend.com/en-us/products/pe-anti-human-cd160-antibody-8052)
Anti-human 4-1BB-PE-CY7 antibodies (BioLegend, Cat: #309818, https://www.biolegend.com/en-us/products/pe-cyanine7-anti-human-cd137-4-1bb-antibody-6540)
Anti-mouse CD45-FITC antibody (BioLegend, Cat: #103107, https://www.biolegend.com/en-us/products/fitc-anti-mouse-cd45-antibody-99)
Anti-mouse CD3 Percp-Cy5.5 antibody (BioLegend, Cat: # 100218, https://www.biolegend.com/en-us/products/percp-cyanine5-5-anti-mouse-cd3-antibody-5596)
Anti-mouse CD8 Percp-Cy5.5 antibody (BioLegend, Cat: #100734, https://www.biolegend.com/en-us/products/percp-cyanine5-5-anti-mouse-cd8a-antibody-4255)
Anti-mouse CD8α-APC antibody (BioLegend, Cat: #100712, https://www.biolegend.com/en-us/products/apc-anti-mouse-cd8a-antibody-150)
Anti-mouse CD4-PE-CY7 antibody (BioLegend, Cat: # 100422, https://www.biolegend.com/en-us/products/pe-cyanine7-anti-mouse-cd4-antibody-1919)
Anti-mouse CD160-PE antibody (BioLegend, Cat: #143004, https://www.biolegend.com/en-us/products/pe-anti-mouse-cd160-antibody-7574)
PE/Cyanine7 anti-human/mouse Granzyme B Recombinant (BioLegend, Cat: #372214, https://www.biolegend.com/en-us/products/pe-cyanine7-anti-humanmouse-granzyme-b-recombinant-antibody-15582)
Anti-human/mouse Granzyme B-FITC antibody (BioLegend, Cat: #515403, https://www.biolegend.com/en-us/products/fitc-anti-human-mouse-granzyme-b-antibody-6066)
Anti-mouse Granzyme B-PerCP-Cy5.5 antibody (BioLegend, Cat: #372211, https://www.biolegend.com/en-us/products/percp-cyanine5-5-anti-humanmouse-granzyme-b-recombinant-antibody-15597)
Anti-mouse PD-1-FITC antibody (BioLegend, Cat: #135213, https://www.biolegend.com/en-us/products/fitc-anti-mouse-cd279-pd-1-antibody-7004)
Anti-mouse TCF1/TCF7-RB705 antibody (BD Biosciences, Cat: #570635, https://www.bdbiosciences.com/zh-cn/products/reagents/flow-cytometry-reagents/research-reagents/single-color-antibodies-ruo/rb705-mouse-anti-tcf7-tcf1.570635?tab=product_details)
Anti-TCF1/TCF7-PE antibody (Cell Signaling Technology, Cat: #14456S, https://www.cellsignal.cn/products/antibody-conjugates/tcf1-tcf7-c63d9-rabbit-mab-pe-conjugate/14456)
Anti-mouse CD366 (TIM3)-PE-CY7 antibody (BioLegend, Cat: #134010, https://www.biolegend.com/en-us/products/pe-cyanine7-anti-mouse-cd366-tim-3-antibody-13929)
Anti-Mouse CD137 (4-1BB)-PE-CY7 antibody (Thermo Fisher, Cat: #25-1371-82, https://www.thermofisher.cn/cn/zh/antibody/product/CD137-4-1BB-Antibody-clone-17B5-Monoclonal/25-1371-82)
Anti-Fcer1g-FITC antibody (Sigma, Cat: #FCABS400F, https://www.sigmaaldrich.cn/CN/zh/search/fcabs400f?focus=products&page=1&perpage=30&sort=relevance&term=FCABS400F&type=product)
PE Rat IgG2a, κ Isotype Ctrl Antibody (BioLegend, Cat: #400507, https://www.biolegend.com/en-us/products/pe-rat-igg2a-kappa-isotype-ctrl-1843)
PE Mouse IgM, κ Isotype Ctrl Antibody (BioLegend, Cat# 401611, https://www.biolegend.com/en-us/products/pe-mouse-igm-kappa-isotype-ctrl-3163)
TruStain FcX™ (anti-mouse CD16/32) Antibody (BioLegend, Cat: #101319, https://www.biolegend.com/en-us/products/trustain-fcx-

anti-mouse-cd16-32-antibody-5683)
Anti-mouse CD45.1-APC antibody (BioLegend, Cat: #110714, https://www.biolegend.com/en-us/products/apc-anti-mouse-cd45-1-antibody-2319)
Anti-mouse CD45.2-PerCP-Cy5.5 antibody (BioLegend, Cat: #109827, https://www.biolegend.com/en-us/products/percp-cyanine5-5-anti-mouse-cd452-antibody-4271)
T-Select H-2Kb OVA Tetramer-SIINFEKL-PE (MBL Life Science, Cat# TS-5001-1C, https://www.mblbio.com/bio/g/dtl/T/?pcd=TS-5001-1C)
Antibodies for Multiplex immunohistochemistry:
CD8α (D4W2Z) XP® Rabbit mAb (Cell Signaling Technology, Cat: #98941, https://www.cellsignal.cn/products/primary-antibodies/cd8a-d4w2z-xp-rabbit-mab/98941)
PD-1 (D7D5W) XP® Rabbit mAb (Cell Signaling Technology, Cat: #84651, https://www.cellsignal.cn/products/primary-antibodies/pd-1-intracellular-domain-d7d5w-xp-rabbit-mab/84651)
TCF1/TCF7 (C63D9) Rabbit mAb (Cell Signaling Technology, Cat: #2203, https://www.cellsignal.cn/products/primary-antibodies/tcf1-tcf7-c63d9-rabbit-mab/2203)
Rabbit anti-mouse TIM3 (Abcam, Cat: #ab241332, https://www.abcam.cn/products/primary-antibodies/tim-3-antibody-epr22241-ab241332.html)
Granzyme B Antibody (2C5) (Santa Cruz Biotechnology, Cat: #sc-8022, Lot E0719, 1:200)
InVivoMAb Rat IgG2α isotype control (BioXcell, Cat: #BE0089, https://www.bioxcell.com.cn/in-vivo-antibodies/invivomab-rat-igg2a-isotype-control-anti-trinitrophenol-be0089.html)
InVivoMAb anti-Mouse PD-1 (CD279) (BioXcell, Cat: #BE0146, https://www.bioxcell.com.cn/in-vivo-antibodies/invivomab-anti-mouse-pd-1-cd279-be0146.html)
anti-mouse CD3 Antibody (BioLegend, Cat: #100340, https://www.biolegend.com/en-us/products/ultra-leaf-purified-anti-mouse-cd3epsilon-antibody-7722)
anti-mouse CD28 Antibody (BioLegend, Cat: #102116, https://www.biolegend.com/en-us/products/ultra-leaf-purified-anti-mouse-cd28-antibody-7733)

Eukaryotic cell lines

Policy information about cell lines and Sex and Gender in Research

Cell line source(s)	The MC38 murine cell line was obtained from National Infrastructure of Cell Line Resource (Beijing, China); The CT26 murine cell line was obtained from Stem Cell Bank of the Chinese Academy of Sciences (Shanghai, China); The MC38-OVA murine cell line and MC38-GFP murine cell line were kindly provided by Dr. Chang Shao, China Pharmaceutical University (Nanjing, China); HEK-293T were purchased from the China Center for Type Culture Collection (Wuhan, China).
Authentication	All the cells lines used in this study were authenticated by the supplier using STR.
Mycoplasma contamination	Tested negative for mycoplasma.
Commonly misidentified lines (See ICLAC register)	No commonly misidentified lines were involved in this study.

Animals and other research organisms

Policy information about studies involving animals; ARRIVE guidelines recommended for reporting animal research, and Sex and Gender in Research

Laboratory animals	Male C57BL/6 and Balb/c mice (6–8 weeks old) were purchased from Liaoning Changsheng Biotechnology Co., Ltd, while B6-H11-CAG-EGFP, CD45.1 congenic mice and Cd160 knockout (Cd160-/-) mice on a C57BL/6 background were purchased from GemPharmatech. Co., Ltd. For animal experiments with knockout mice, wild-type (WT) littermate controls on the same C57BL/6 background at the age of 6 to 10 weeks were used. Mice were housed in a controlled, specific pathogen-free environment and received humane care in accordance with the animal welfare guidelines. All mice were maintained under the conditions of pathogen-free, 12 hours light/12 hours dark cycle, temperatures of 18–23 °C, and 40–60% humidity.
Wild animals	No wild animals were used in this study.
Reporting on sex	Male or female CD160 knockout mice, male C57BL/6 mice, Balb/c mice, 6-H11-CAG-EGFP mice, CD45.1 congenic mice were used in this study.
Field-collected samples	No field-collected samples in this study.
Ethics oversight	All animal experiments were conducted in compliance with protocols approved by the institutional Animal Care and Use Committee of Harbin Medical University.

Note that full information on the approval of the study protocol must also be provided in the manuscript.

Plants

Seed stocks	*Report on the source of all seed stocks or other plant material used. If applicable, state the seed stock centre and catalogue number. If plant specimens were collected from the field, describe the collection location, date and sampling procedures.*
Novel plant genotypes	*Describe the methods by which all novel plant genotypes were produced. This includes those generated by transgenic approaches, gene editing, chemical/radiation-based mutagenesis and hybridization. For transgenic lines, describe the transformation method, the number of independent lines analyzed and the generation upon which experiments were performed. For gene-edited lines, describe the editor used, the endogenous sequence targeted for editing, the targeting guide RNA sequence (if applicable) and how the editor was applied.*
Authentication	*Describe any authentication procedures for each seed stock used or novel genotype generated. Describe any experiments used to assess the effect of a mutation and, where applicable, how potential secondary effects (e.g. second site T-DNA insertions, mosiacism, off-target gene editing) were examined.*

Flow Cytometry

Plots

Confirm that:

☒ The axis labels state the marker and fluorochrome used (e.g. CD4-FITC).

☒ The axis scales are clearly visible. Include numbers along axes only for bottom left plot of group (a 'group' is an analysis of identical markers).

☒ All plots are contour plots with outliers or pseudocolor plots.

☒ A numerical value for number of cells or percentage (with statistics) is provided.

Methodology

Sample preparation	Fresh tissues were dissected into 1 mm3 fragments using scissors and then enzymatically digested with RPIM-1640 medium mixture supplemented with 1 mg/mL collagenase IV (Solarbio), and 0.1 mg/mL DNase (Solarbio) for 1 hour using a constant temperature shaker (Spring Instrument Co., Ltd) at 37°C. The dissociated cells from relative tissues were filtered through a 70 µm cell strainer (Biosharp) and collected by centrifugation at 600 g for 20 minutes. Red blood cells were lysed with red blood cell lysis buffer (Miltenyi) on ice for 5 minutes. Single-cell suspensions were immediately stained with Zombine NIR (APC/CY7) followed by antibodies staining.
Instrument	Flow cytometer (BD FACSMelodyTM)
Software	FlowJo software (v10.8.1)
Cell population abundance	The purity of the sorted populations was verified by flow cytometry (> 95% pure).
Gating strategy	A single discrimination and live-dead cell exclusion was performed at gating strategy. Then CD45+ cells were gated, other immune cell populations were gated subsequently.

☒ Tick this box to confirm that a figure exemplifying the gating strategy is provided in the Supplementary Information.